ABSTRACT

Title of dissertation: Measuring Electromagnetic Properties of
Superconductors in High and Localized
RF Magnetic Field

Tamin Tai, Doctor of Philosophy, 2013

Dissertation directed by: Professor Steven M. Anlage
Department of Electrical and Computer Engineering

Niobium-based Superconducting Radio Frequency (SRF) particle accelerator cavity performance is sensitive to localized defects that give rise to quenches at high accelerating gradients. In order to identify these material defects on bulk Nb surfaces at their operating frequency and temperature, it is important to develop a new kind of wide bandwidth microwave microscopy with localized and strong RF magnetic fields. A novel near-field magnetic field microwave microscope that enables mapping of the local electrodynamic response in the multi-GHz frequency regime at liquid helium cryogenic temperatures was successfully built via the combination of a magnetic writer and a near field-microwave microscope [1] [2]. This magnetic writer can create a localized and strong RF magnetic field and should achieve a condition with $B_{surface} \sim 150$ mT and sub-micron resolution (Chapter 3). Our objective is to study the extreme and local electrodynamic properties of Niobium (Nb), and to relate these properties to specific defects that limit the ultimate RF performance of

---

[1] T. Tai, et al., IEEE Trans. Appl. Supercond. 21, 2615, (2011).
[2] T. Tai et al., IEEE Trans. Appl. Supercond. 23, 7100104, (2013).

superconducting radio frequency cavities made from Nb.

Therefore, in this dissertation, many superconducting materials, especially the candidate materials for superconducting RF cavities, were tested at a fixed location to analyze the local electrodynamic response through linear and nonlinear microwave measurements. For the linear measurement (Chapter 4), many fundamental properties of RF superconductivity such as the critical temperature (T_c) and penetration depth (λ) can be identified. For the nonlinear response measurement (Chapter 5), both the intrinsic and extrinsic nonlinearities from the superconductors are excited by our magnetic write head probe. Many models are introduced to identify the measured nonlinearity, including the intrinsic nonlinearity from the modulation of the superconducting order parameter near T_c, and the extrinsic nonlinearity from the moving vortex model, weak-link Josephson effect, and the possible nonlinear mechanism from switching events between the Meissner state and the mixed state. These models of extrinsic nonlinearity are studied in Chapter 6.

The high transition temperature and low surface resistance of MgB_2 attracts interest in its potential application in superconducting radio frequency accelerating cavities. However, compared to traditional Nb cavities, the viability of MgB_2 at high RF fields is still open to question. Hence, in Chapter 7, two-gap high quality MgB_2 films with thickness 50 nm, fabricated by a hybrid physical-chemical vapor deposition technique on dielectric substrates, are measured at a fixed location to investigate its RF properties. The third harmonic measurement on MgB_2 films shows different nonlinear mechanisms compared to the bulk Nb measurement [3]. We con-

---

[3]T. Tai et al., Phys. Rev. ST Accel. Beams 15, 122002, (2012).

clude that the nonlinear response for the high quality MgB_2 films at temperature less than T_c shows the nonlinearity from the moving vortices and from the following possible mechanisms: First, an intrinsic nonlinearity from the proximity-induced second T_c. Second, the intrinsic nonlinearity arising from Josephson coupling between the σ and π bands of the two-gap nature of MgB_2. Third: The potential nonlinearity from the reported superconducting nodal gap properties.

Finally the future plan to raster scan on the SRF candidate materials is proposed to relate the nonlinear electromagnetic images to the physical defects on the superconductor surface. These efforts can finally feed back to the cavity processing techniques and suggest new thoughts for alternate surface processing treatment in the future.

MEASURING ELECTROMAGNETIC PROPERTIES OF SUPERCONDUCTORS IN HIGH AND LOCALIZED RF MAGNETIC FIELD

by

Tamin Tai

Dissertation submitted to the Faculty of the Graduate School of the
University of Maryland, College Park in partial fulfillment
of the requirements for the degree of
Doctor of Philosophy
2013

Advisory Committee:
Professor Steven M. Anlage, Chair/Advisor
Professor Mel Gomez
Professor James R. Anderson
Professor Jeremy Munday
Professor Victor L. Granatstein

Acknowledgments

First of all, I would like to specially thank my advisor, Prof. Steven Mark Anlage for giving me an opportunity to join his talented team at Center for Nanophysics and Advanced Materials (CNAM) in Physics. Under his patient instruction, I step into the field of superconductivity for the first time in my life. His enthusiasm for physics and positive attitude encourage me to look for answers and solutions in many complicated physics and engineering problems. He creates a very creative and dynamic research environment for all his students and gradually lead his students into many amazing research projects. While I am struggling in the research, he always can provide me numerous ideas and guide me to the correct way without getting lost.

Secondly, I would like to thank our group postdoc, Dr. Behnood G. Ghamsari, and Prof. Anlage for their help in theoretical modeling. Without their theoretical expertise in RF superconductivity, this thesis would not be complete. John Abraham, a undergraduate student in our group, also help me in finite element modeling. I really learn lots of his technique among many commercial finite element simulators.

Also, I would like to thank another postdoc, Dr. Cihan Kurter, in our group for her help in photolithography. Besides, many graduate students and postdocs in Prof. Fuhrer's group (for examples: Harold Cai, Jacob Tosado, Mahito Yamamoto, Dr. Claudia Ojeda-Aristizabal, Dr. Wenzhong Bao) teach me how to use their E-beam system, AFM equipment and wire bonder. They also kindly share their processing parameters with me to let me work out my device quickly. Besides,

Prof. Gomez, Prof. Munday and Prof. Granatstein for being my doctoral defense committees.

Most of all, I am deeply indebted to my parents, Mr. Chin-Shan Tai and Miss Chin-Li Chou, for their countless love and support to make what I am today. They dedicated themselves to educating me toward success. Words cannot express the gratitude I owe them.

Finally, it is impossible to remember all, and I apologize to those I've inadvertently left out.

Lastly, thank you

CONTENTS

LIST OF FIGURES

x

xviii

xix

List of Symbols

λ London penetration depth

τ One RF period time

Φ Magnetic flux

Φ_0 Magnetic flux quantum

μ_0 Permeability of free space

K Surface current

Γ Probe geometry factor

b_Θ Nonlinear coefficient

B_c Thermodynamic critical B-field

B_{c1} Lower critical B-field

B_{c2} Upper critical B-field

H_c Thermodynamic critical H-field

H_{c1} Lower critical H-field

H_{c2} Upper critical H-field

J_{NL} Nonlinear current density scale

J_c Critical current density

m^* Mass of an electron pair

P_f Fundamental power

P_{3f} Third harmonic power

q^* Charge of an electron pair

Q   Quality factor of a cavity

T   Temperature

T_c critical temperature

V_{3f} Third harmonic voltage

List of Abbreviations

BCP	Buffered chemical polishing
BCS	Bardeen-Cooper-Schrieffer
dBm	Power ratio in decibels (dB) of the measured power referenced to one milliwatt (mW)
E-Beam	Electron Beam
Ecal	Electronic calibration
EP	Electro polishing
GHz	Gigahertz, 10^9 Hz
GL	Ginzburg-Landau
GMR	Giant magnetoresistance
HDDs	Hard disk drives
HF-MFM	High frequency magnetic force microscopy
HFSS	High frequency structure simulator
HPCVD	Hybrid physical-chemical vapor deposition
ILC	International Linear Collider
IMD	Intermodulation Distortion
LSM	Laser scanning microscope
MFM	Magnetic force microscope
MgB_2	Magnesium Diboride
MSU	Michigan State University
NLME	Nonlinear Meissner effect
Nb	Niobium
Nb_3Sn	Tri-Niobium Tin
PMMA	polymethyl methacrylate
REF	Reference signal
RF	Radio frequency
SEM	Scanning electron microscope
SHPM	Scanning hall probe microscope
S-C-S	Superconductor-constriction-superconductor
S-I-S	Superconductor-insulator-superconductor junction
S-N-S	Superconductor-normal metal-superconductor junction
SNR	Signal to noise ratio
SRF	Superconducting radio frequency
SQUID	Superconducting quantum interference device
Ta	Tantalum
TBCCO	$Tl_2Ba_2CaCu_2O_8$
TM	Transverse Magnetic modes of wave
TMR	Tunneling Magnetoresistance
UMD	University of Maryland
VNA	Vector network analyzer
YBCO	Yttrium barium copper oxide $YBa_2Cu_3O_{7-x}$

1. INTRODUCTION: MOTIVATION FOR THE DISSERTATION

1.1 Material Problems in Niobium Cavities Utilized in Novel Electron Accelerators

In particle physics, researchers want to build high energy accelerators to accelerate electrons and positrons up to near light velocity using superconducting cavities. These superconducting cavities are electromagnetic cavities resonating at a microwave frequency and can handle a high microwave power. The goal is to convert electromagnetic energy into the kinetic energy of the charged particles as efficiently as possible. Figure 1.1(a) [1] shows several cells of the superconducting cavities. The length of each cell is half a wavelength long $(\lambda/2)$ to ensure electrons can continue accelerating in the next half of the radio-frequency (rf) period. Each cell works under high electric and magnetic field with the highest electric field on the accelerating axis and maximum magnetic field on the equator as shown in Fig. 1.1(b) and Fig. 1.1(c). Therefore, in choosing a superconductor for a RF cavity design, materials with a high thermodynamic critical magnetic field (B_c), a low RF surface resistance and a high critical temperature (T_c) are preferred to achieve the highest energy gradient in the accelerator to tolerate strong magnetic and electric fields and to avoid energy loss during the acceleration of particle beams. In addi-
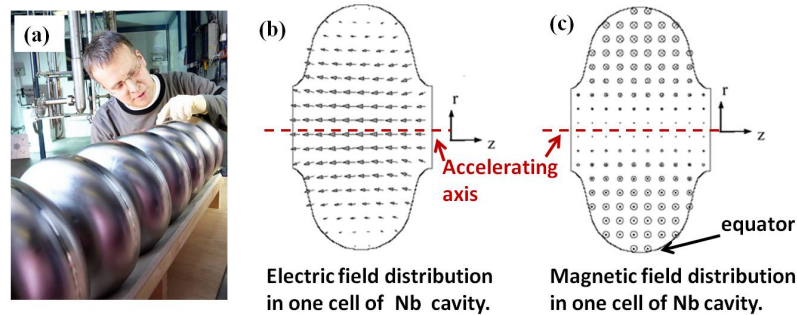
Fig. 1.1: (a) Current niobium superconducting radio frequency (SRF) cavities for particle accelerators. This figure comes from reference [1]. (b) Calculated electrical field distribution in one cell cavity. Note maximum electrical field is pointed along the z-axis which is the propagation direction of the accelerated beam. (c) Associated magnetic field distribution inside the cavity. The maximum magnetic field is on the equator pointing in and out of the paper plane. A electron beam weld is located at the point of maximum magnetic field.

tion to technical considerations, materials that are easy to fabricate and to achieve uniformly good material properties over a large surface area are favorable. Based on the above considerations, elemental superconductors are better than many superconducting compounds (for example: MoGe, Nb_3Ge and the high T_c cuprates). Therefore niobium (Nb) is the most acceptable one among many elemental superconductors. The first Nb cavities were successfully tested at Stanford University in 1967 by H. A. Schwettman and J.P. Turneaure [2]. At that time, the quality factor (Q) of this cavity was not good because of poor fabrication technology. Fortunately, thanks to today's post processing technology such as electro polishing (EP), buffered chemical polishing (BCP) and heat treatment, some Nb cavities have been demonstrating high Q ($\sim 10^{10}$ or more [3]) and high accelerating gradient (~ 59 MeV/m in a fine-grain niobium single cell cavity [4]).

However when researchers want to put these lab-fabricated cavities into commercial mass-production, many problems arise. Such high performance cavities

cannot be manufactured with any degree of certainty and regularity. Much debate regarding this inconsistent performance concluded that certain types of defects on the Nb cavities' surfaces behave as a source of quenching in high RF magnetic fields. A quench is when the Nb superconductor returns to the normal state in the presence of strong magnetic fields, thus limiting their utility. Candidates for these defects include pits, oxides, hydrides, impurity inclusions, surface grain boundaries etc., as illustrated schematically in Fig. 1.2 [5]. These defects arise from cavity fabrication steps such as forming, machining, electron beam welding, EP and BCP. These defects are either non-superconducting or have lower T_c, making them sources of dissipation and interrupting the superconducting current flow. Unfortunately, it is extremely hard to totally remove all of these defects even after sophisticated physical and chemical treatments. Because different defects have their individual quench limit, not all of the defects behave as sources of quenching in certain operation conditions (for example, a 9 cell TESLA cavity usually operates at a temperature of 2 K, an initial accelerating gradient of 25 MV/m, 1.3 GHz RF frequency under 16.5 MW beam power [6]).

Scientists don't know which defects have lower quench limits and therefore it is necessary to quantitatively understand the quench limit for different individual defects. Therefore, completely understanding the effects of different physical defects on the bulk Nb surface under RF electromagnetic field is one of the most important issues in this field. Once scientists can completely understand the relation between ultimate microwave performance and local material properties, they can offer a strategy to remove the truly deleterious defects that result in the superconductor
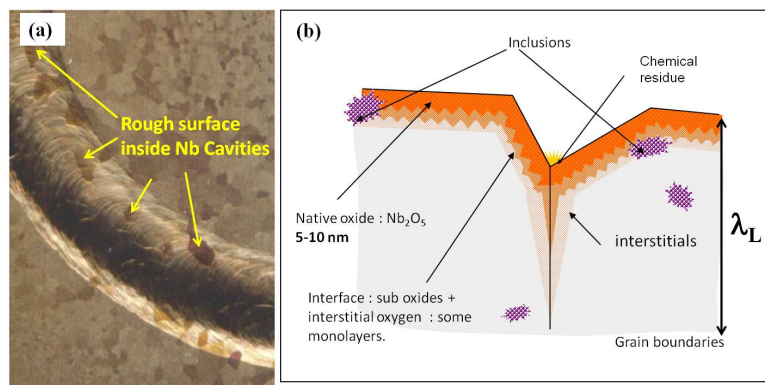
Fig. 1.2: (a) Optical images of the Nb surface from the inner side of an SRF cavity near an electron beam weld. Many defects can be found on the rough surface of bulk Nb. (b) Schematic picture of different types of defects on the Nb surface. Those defects include a few monolayers of native oxide, Tantalum (Ta) inclusions, chemical residues, Niobium-hydride, grain boundaries etc. The λ here illustrates the length scale in the vertical direction, which is the London penetration depth. The screening current and magnetic field at the surface exponentially decay to zero with this characteristic length scale. For bulk Nb, the λ_L at zero temperature is 40 nm. Figures come from reference [5].

quench of the cavities. This in turn opens the way to mass-produce the 17,000 or so cavities required to build the proposed International Linear Collider (ILC) [7].

Due to the defect issues with Nb, many different methods have been proposed to look for defects on the inner side of the cavities. For example, optical microscopy techniques have been developed to identify defects in finished Nb cavities at ambient temperature [8]. However, this optical screening process may result in identification of relatively benign defects which will not result in a quench of the superconductor under the operation conditions of the SRF cavities. Therefore, ideally one would like a microscopic technique that identifies defects based on their poor microwave performance at low temperatures in the superconductive state.

One of the best candidates for this challenging work is the near field microwave

4

microscope which has been developed to quantitatively image RF and microwave properties of a variety of materials on deep sub-wavelength scales [9] [10] [11] [12]. However, based on the demands to diagnose material problems in SRF cavities, a strong "RF magnetic tip" probe is necessary to perform a raster scanning on Nb coupons, which are Nb pieces sliced from the Nb cavities, and analyze the surface critical field, the surface breakdown field and the locally induced nonlinearity. Due to this requirement in SRF cavities, our probes must achieve the following conditions:

(1) A magnetic probe should provide an RF magnetic field with peak field up to the Nb thermodynamic critical field ($\sim 200\,mT$).

(2) A magnetic probe should operate in the high RF frequency region ($1\,GHz \sim 2\,GHz$ or higher) to reproduce the accelerator operating condition.

(3) A magnetic probe should be as small as possible to provide a localized magnetic field to improve the resolution and isolate closely separated defects.

(4) A magnetic probe should operate at SRF temperatures, usually 2K.

Finally, with this microscopy method, researchers in the SRF community will understand the detailed connection between local Nb defects created by different kinds of surface treatment and the final performance in a high RF magnetic field. With this, researchers will know which kinds of defects in cavity fabrication result in the superconductor quenching during operation and propose an effective method to remove them in the cavity fabrication. Our work in measuring high frequency microwave properties of Nb superconductors will definitely benefit the SRF community to understand the key issues that lead to degradation in the performance of Nb cavities.

1.2 Limitations of Existing Magnetic Field Microscopy

Magnetic imaging techniques have quickly grown up in the past decades due to the rapid development of magnetic microscopy. For example, magnetic force microscopy (MFM) [13], scanning superconducting quantum interference device (SQUID) microscopy [14] [15], scanning Hall probe microscopy (SHPM) [16] and magneto-optic Kerr microscopy [17] are all widely used in industry and in academic research to record the magnetic structure on the surface of materials by sensing the surface stray magnetic fields. However, each of the microscopy techniques varies in its limits of applicability. SHPM and Magneto-optical Kerr microscopy are not very sensitive to flux change and only work well in a DC or low frequency field (Note: The maximum frequency responses of SHPM depends on the working frequency of the semiconductor Hall sensor. For Kerr microscopy, the upper operating frequency is also constrained by the working frequency of the semiconductor photo detector. Both are generally in the kHz frequency region based on today's semiconductor technology.) The Scanning SQUID has the highest field sensitivity, but its high sensitivity degrades at high frequencies [18] and the spatial resolution is limited to the size of the pick-up coil [19], usually a few microns. On the other hand, although MFM has achieved the best spatial resolution (a few nm scale) and successfully demonstrated in high-frequency operation as high frequency MFM (HF-MFM) [20], it is still difficult to quantitatively analyze the data from MFM images. In addition, the resolution of HF-MFM will decrease while operating above 2 GHz [21] [22] and the field provided by the probe is only a constant field, not a driving RF field.

6

All of the microscopes described above are unable to provide a strong radio frequency (RF) magnetic field on a localized area. Because of these limitations, many ideas about the driving force magnetic probe (excited probes) have arisen recently. However creating a concentrated microwave magnetic field in a small area of the sample is a challenge and has created interest among many research groups using different methods. The fundamental method is to make a loop-shaped coil as small as possible to generate a concentrated magnetic field on the sample.[10] [11] [12] [23] [24]. Some groups also bundle many loop shaped coils to generate a strong localized field [25], but unfortunately this method will sacrifice spatial resolution. Recently several groups have used the method of either photo-lithography or E-beam lithography to fabricate a micro-coil and successfully generated about 10 Tesla to 50 Tesla of pulsed magnetic field on 30 ns time scales [26][27]. One group also demonstrated that this nanosecond pulsed field can switch the magnetization of nano magnetic particles [28], but this method will generate lots of heat and may not be useful to probe the properties of superconductors due to the unpredictable sample heating during the measurement. Another study on utilizing spin-torque-driven microwaves to generate a localized ac magnetic field to flip the magnetization direction of a thin single domain magnetic element has been widely discussed recently [29][30][31][32]. However this technique doesn't have application yet in investigating the properties of SRF cavities. Fig. 1.3 shows a brief summary of developments of localized high RF magnetic field measurements. These ideas may have potential for application in a high resolution magnetic microscope in the GHz frequency regime in the future.

In a word, based on the need of the SRF community to identify defects on
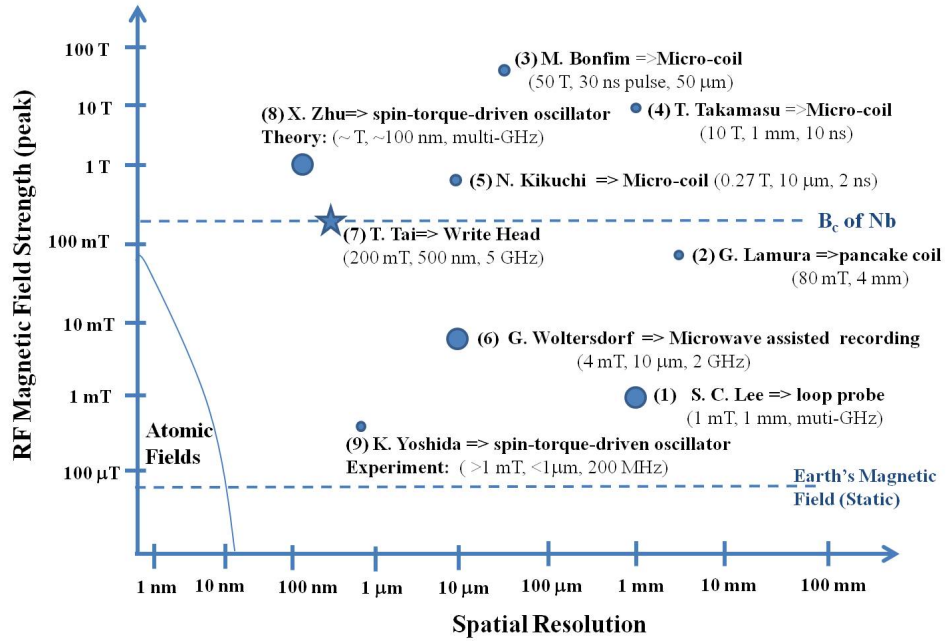
Fig. 1.3: High-Field, High-Resolution AC/Transient Magnetic Microscopy Generating Highly-Confined Magnetic Fields with Frequency > 1 GHz : A summary of methods to generate a highly concentrated RF magnetic field. Each technique lists a typical RF magnetic field scale, degree of spatial resolution, and an associated time/frequency scale demonstrated. All of the candidate technologies are numbered and referenced as follows (1) S. C. Lee $\Rightarrow$ loop probe. [10] [11] [12]. (2) G. Lamura $\Rightarrow$ pancake coil [25] (3) M. Bonfim $\Rightarrow$ Micro-coil [26] (4) T. Takamasu $\Rightarrow$ Micro-coil [27] (5)N. Kikuchi $\Rightarrow$ Micro-coil [28] (6) G. Woltersdorf $\Rightarrow$ Microwave assisted recording [29]. (7) T. Tai $\Rightarrow$ Write Head [33]. (8) X. Zhu $\Rightarrow$ spin-torque-driven oscillator [31]. (9) K. Yoshida $\Rightarrow$ spin-torque-driven oscillator [32]. Note the large circle ($\bullet$) and star sign ($\star$) size indicates the operation frequency/speed :larger symbols correspond to higher frequencies. The star also indicates the method used in this dissertation.

Nb surfaces [34], a completely novel magnetic microscope with the capability of imaging in the high frequency regime (at least a few GHz) under a strong RF field and at cryogenic temperatures is desirable. This dissertation will address our achievement to measure the electromagnetic response (linear and harmonic signals) from SRF related materials (Nb & MgB_2) in localized regions down to sub-micron scale. A detailed discussion of the modeling for the experimental measurement will be addressed. My effort to image surface defects will be discussed in the final chapter.

9

2. FUNDAMENTALS OF SUPERCONDUCTIVITY

2.1 Superconductivity and intrinsic nonlinearity

Superconductivity was first discovered in Mercury (Hg) in 1911 by Dr. Kamerlingh Onnes [35]. After Hg, physicists discovered that most non-ferromagnetic metals have a superconducting ground state. This superconducting phase has the common phenomena of exactly zero dc electrical resistance and expulsion of magnetic fields when the materials are cooled below their individual critical temperature in a small static magnetic field. The spontaneous expulsion of magnetic flux from the interior of the superconductor is called the Meissner effect. It is a remarkable fact that while the superconductor is immersed in a static magnetic field and cooled below T_c, spontaneous screening currents will be induced on the surface of the superconductor with a direction perpendicular to the direction of magnetic field to actively exclude the external magnetic flux. In this situation, we say the superconductor establishes the Meissner state. However, from the microscopic point of view, the Meissner effect does not cause the field to be completely ejected but instead the field penetrates the superconductor to a very small distance, characterized by a parameter λ, called the London penetration depth or penetration depth for simplicity. The magnetic field decays exponentially to zero within the bulk of the superconductor. Hence the

screening only happens within a few penetration depths below the surface. This is the reason why the near surface ($\sim 100\ nm$) properties of Nb are so critical for SRF applications.

The screening effect can be interpreted by the London equations which describes the relation of the supercurrent density (J_s) and electrical & magnetic fields ($E\&B$)

$$\frac{d}{dt}(\Lambda \mathbf{J_s}) = \mathbf{E} \tag{2.1a}$$

$$\mathbf{B} = -\nabla \times (\Lambda \mathbf{J_s}) \tag{2.1b}$$

$$where \qquad \Lambda \equiv \frac{m^*}{n_s q*^2}$$

Note that in the Meissner state, two electrons with equal and opposite momentum and spin forms a pair to reduce the internal energy. Therefore, $m^* = 2m$ and $q^* = 2e$ are the mass and charge of an electron pair (Cooper Pair), respectively. n_s is superfluid density which means the numbers of electron pairs per unit volume. From the first London equation (2.1.a), one can clearly see that the dc current can exist without electrical field, which can describe the zero dc resistance in the Meissner state. The second London equation (2.1.b), when combined with the Maxwell equation, $\nabla \times \mathbf{H} = \mathbf{J}$, leads to

$$\nabla^2 B = \frac{B}{\lambda^2}$$
$$where \qquad \lambda^2 \equiv \frac{\Lambda}{\mu_0} \tag{2.2}$$

This equation describes Meissner screening that screens out almost all of the magnetic field although it penetrates a penetration depth, λ, into the superconductor. Despite interpreting the Meissner effect successfully in the London equation, many superconductivity phenomena cannot be interpreted by this over-simplified model due to some assumptions in the London model. One limitation is that in the London model, the superfluid density is assumed uniform in space and the applied magnetic field (B) is much smaller than the critical field. If an applied magnetic field approaches the critical value, defined as a thermodynamic critical field, B_c, the response of superconductivity to the magnetic field will be very complex. Based on its response to a magnetic field, superconductors can be classified into two types, type I superconductors and type II superconductor. For type I superconductors, they have a single critical field, B_c, above which all superconductivity is lost. For type II superconductors, they have two critical fields, defined as lower critical field (B_{c1}) and upper critical field (B_{c2}). Partial magnetic penetration is allowed while the applied magnetic field is in between B_{c1} and B_{c2}. In this situation, the superconductor is in a mixed state (also known as the vortex state) . The discussion of the vortex state will be addressed in section 2.2. Note that bulk Nb is typically a type-I material, whereas thin film Nb is typically type-II. This variation is due to the relative size of the coherence length and mean-free path of the conduction electrons.

For both type I and type II superconductors, the response of an electron gas to the electric field should be considered in a localized region where the field is not uniform. Therefore, in the rigorous case, superconductivity would become

very complicated while considering spatially nonuniform fields on the scale of the penetration depth and with nonuniform n_s.

If the superfluid density is perturbed by external factors, superconductors will behave in a nonlinear manner in many measurable quantities. For all superconductors, this nonlinear manner is expected to be present and is considered to be an intrinsic nonlinearity. These external factors can be in the form of an applied current or magnetic field, for example. If the applied field/current is much smaller than the critical field/current, the generated nonlinearity is usually regarded as the nonlinear Meissner effect (NLME), which can be described by the Ginzburg-Landau (GL) theory. This GL theory was first presented by Ginzburg and Landau in 1950 [36]. They introduced a complex spatial pseudowavefunction $\psi(r)$ as a complex order parameter of the superconducting state. Therefore the local density of the superconducting electrons would be given by :

$$n_s = |\psi(r)|^2 \tag{2.3}$$

Assuming the smallness of $|\psi(r)|$ and smallness of its gradients with respect to space, the Ginzburg-Landau free energy density, f, can be expanded in a series of powers of $|\psi|$, its gradient, and different forms of energy

$$f = f_{n0} + \alpha|\psi(r)|^2 + \frac{\beta}{2}|\psi(r)|^4 + \frac{1}{2m^*} \mid (\frac{\hbar}{i}\nabla - e^*\mathbf{A})\psi \mid^2 + \frac{|\mathbf{B}|^2}{\mu_0} \tag{2.4}$$

where $\mathbf{A}$ is the magnetic vector potential, α and β are treated as phenomenological parameters, and f_{n0} is the normal state free energy density of the material.

13

This GL theory links the electrodynamic properties with the thermodynamic properties of a superconductor and provides for the spatial inhomogeneity of the superconducting order parameter. By solving this GL equation for different geometries of superconductors with appropriate boundary conditions, the spatial structure of $\psi(r)$ can be explored in any perturbed situation. Many research groups have modeled the intrinsic nonlinearity of both s-wave and d-wave type-II superconductors using the GL eqations [37] [38] [39]. In this way, one finds the inherent nonlinearity of the superfluid density due to an applied current as expressed by [40],

$$\left(\frac{n_s(T, J)}{n_s(T, J = 0)}\right)^2 \cong 1 - b_\Theta(T)\left(\frac{J}{J_c}\right)^2 \tag{2.5}$$

where $n_s(T, J)$ is the superfluid density at temperature (T) and in the presence of current density (J), $n_s(T, J = 0)$ is the superfluid density at the temperature T but in the absence of current. J_c is the critical current density at zero temperature $(T = 0K)$. $b_\Theta(T)$ is a both temperature and direction dependent nonlinear coefficient. Θ is the direction of the superfluid flow with respect to the coordinate axis of the superconducting gap on the Fermi surface as shown in Fig. 2.1. Note that for s-wave superconductors, the gap function is essentially independent of Θ but for d-wave superconductors, it will be strongly dependent on Θ and therefore the properties of superconductivity will be very directional. This angle-dependent nonlinear coefficient $(b_\Theta(T))$ carries information about the intrinsic nonlinear Meissner effect of different types of superconductors.

Figure 2.2 shows the theoretical temperature dependence of the nonlinear co-

14
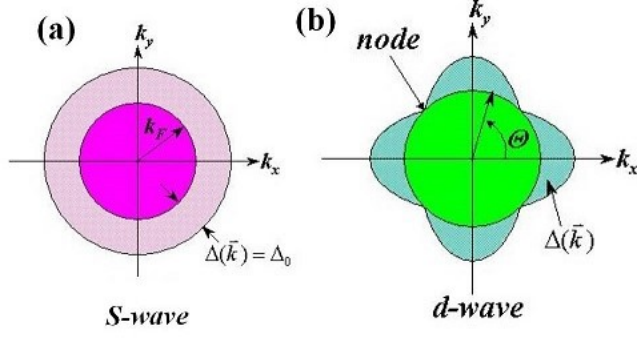
Fig. 2.1: (a)Fermi surface and superconducting energy gap of s-wave super-conductor showing a s symmetry of the pairing wave function. (b) Fermi surface and energy gap of d-wave superconductor showing a $d_{x^2-y^2}$ symmetry of the energy gap.
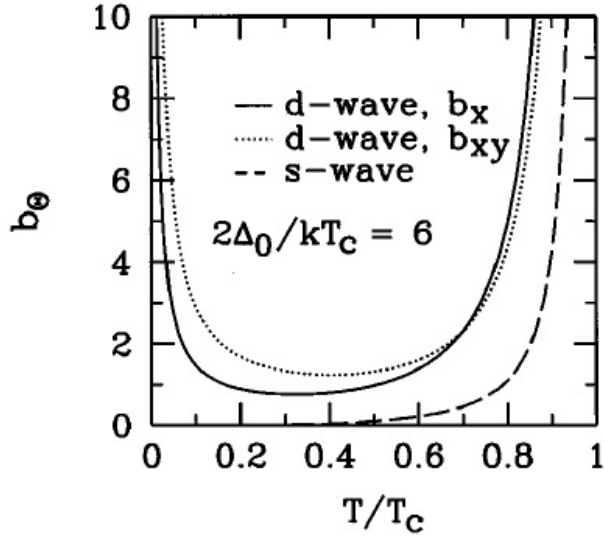
Fig. 2.2: Temperature dependence of the nonlinear coefficient b_Θ for $2\Delta_0/(kT_c) = 6$. The dashed line shows the theoretical result of an isotropic s-wave superconductor. The solid and dotted line are the results for d-wave superconductors with different directions of superfluid flow on the Fermi surface. Note that b_x means superfluid flows in a direction parallel to k_x and b_{xy} is at 45^0 with respect to k_x on the Fermi surface. This figure comes from reference [40].

efficient $b_\Theta(T)$ based on the Dahm and Scalapino model for $2\Delta_0/kT_c = 6$ [40], where Δ_0 is the maximum superconducting gap and k is the Boltzmann constant. From this theoretical prediction, one can see that b_Θ increases tremendously near T_c for s-wave superconductors. However for d-wave superconductors, the b_Θ not only increases tremendously at temperatures near T_c but also increases significantly at temperatures close to 0 K. For both cases, the divergence of $b_\Theta(T)$ at T_c is a general characteristic phenomenon of the superconducting state and is caused by the extreme sensitivity of the superfluid density to external fields and currents, which is the so-called nonlinear Meissner effect. At low temperatures, the divergence of b_Θ in d-wave superconductors is caused by the existence of nodes of the gap function on the Fermi surface. Theoretically, the nature of the nodes in d-wave superconductors will also have a strong surface contribution to the nonlinear Meissner effect due to Andreev bound states at low temperature [41]. The nonlinear measurement of our near field magnetic field microscope would be expected to explore many theoretically predicted intrinsic nonlinear mechanisms and to find novel physics in many recently discovered new superconductors, such as the pnictides.

2.2 Extrinsic nonlinearity of superconductors

2.2.1 Vortex nonlinearity

My microscope is capable of generating a small number of magnetic vortices in the superconductors under study. Therefore it is important to understand the nonlinearity generated by the vortices, as well as their interactions.
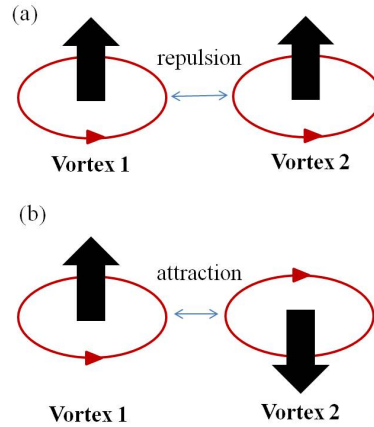
Fig. 2.3: (a)Two vortices with the same direction of field will repel each other.
(b)Two vortices with the opposite direction of field will attract each other.

GL theory is really a great beauty in solving many difficult problems in super-conductivity. One example is that this theory also successfully interprets the flux lattice of type II superconductors in a uniform magnetic field. As mentioned before, magnetic flux will penetrate into the superconductors while the external magnetic field is higher than the lower critical field, B_{c1}, but lower than the upper critical field B_{c2}. In this situation, the superconductors are in the vortex state or mixed state, a state between the Meissner state and the normal state. Abrikosov found a solution to the GL equations in the case of a bulk superconductor immersed in a magnetic field just below B_{c2} [42]. His prediction of an array of flux vortices was confirmed by a variety of experimental methods [43] [44] [45], showing not just that vortices exist, but that they also tend to align in a triangular lattice, as predicted by the theory. The lattice can be periodic over quite long length scales but is disturbed by material defects such as impurities and grain boundaries.

In particular, the Abrikosov solution corresponds to a regular array of vortices

when $B \simeq B_{c2}$. On the other hand, if the field is just above B_{c1}, we can imagine very few vortices in the entire sample and each vortex will be well isolated. Ideally, a single isolated vortex also can be generated by a very localized intense magnetic field [46] [47] [48]. In this situation, a magnetic flux quantum, Φ_0, also known variously as a fluxoid or fluxon, is created. The supercurrent maintains the flux in the core and screens it out of the bulk. As a result, the magnetic field distribution of this fluxon far from its core can be described by

$$|\mathbf{B}(\mathbf{r})| = \frac{\Phi_0}{2\pi\lambda^2} K_0(\frac{r}{\lambda}) \tag{2.6}$$

where K_0 is a zeroth-order Bessel function. Note that while $r \to 0$ (approaches the core) , the magnetic field will diverge logarithmically. In reality, for $r < \xi$, where ξ is the superconducting coherence length, the field is simply approximated by

$$|\mathbf{B}(\mathbf{r})| = \frac{\Phi_0}{2\pi\lambda^2} ln(\kappa) \qquad r < \xi \tag{2.7}$$

where $\kappa = \lambda/\xi$ is the dimensionless Ginzburg-Landau parameter. From this single vortex calculation, the interaction of vortices can be treated. Assume there are two vortices as shown in Fig 2.3. The field at $\mathbf{r}$ is given by the superposition of two individual vortex fields

$$\mathbf{B}(\mathbf{r}) = \mathbf{B_1}(\mathbf{r}) + \mathbf{B_2}(\mathbf{r}) = \mathbf{B_1}(|\mathbf{r} - \mathbf{r_1}|) + \mathbf{B_2}(|\mathbf{r} - \mathbf{r_2}|) \tag{2.8}$$

where $\mathbf{r_1}$ and $\mathbf{r_2}$ specify the positions of the cores of two individual vortices. These

two vortices will have interactions of either repulsion or attraction, depending on the direction of the field in each vortex. The force per unit length on vortex 2 due to the presence of vortex 1 is $\mathbf{f_2} = \mathbf{J_1(r_2)} \times \hat{\Phi}_0$, where $J_1(r_2)$ is the current density generated by vortex 1 at position $\mathbf{r_2}$. The direction of $\hat{\Phi}_0$ is parallel to the flux density. Hence, if two fluxoids have the same direction, a repulsive force between each vortex will be induced. On the other hand, if the field of both vortices are antiparallel, an attractive force will be generated. A vortex also can be in static equilibrium at any given position while the net superfluid velocity from all other sources is zero there. This can be accomplished if one vortex is surrounded by a symmetrical array. If the material has inhomogeneities, vortices may be pinned by defects where the pinning force is bigger than $\mathbf{J_s} \times \hat{\Phi}_0$, where $\mathbf{J_s}$ represents the net transport current density.

In type II superconductors, the vortex critical state has drawn much attention in academic research. Many theoretical models predict the possible responses of vortices in static or dynamic situations. Imaging the vortices on the superconducting materials is an important area of research. It has been popular to use magneto-optical Kerr microscopy to image static vortices in different type II superconductive materials under uniform DC magnetic field. One investigation studied a Nb sheet sliced from a Nb cavity using this magneto-optical imaging technique [55]. Similar experiments are also performed with scanning SQUID microscopy to analyze vortex interactions in Nb and MgB_2 [56]. Both methods are generally performed in a uniform DC magnetic field and have the disadvantage that the dynamic effect of vortex motion cannot be examined.

In reality, vortex motion in type II superconductors is very crucial and quite complicated. This motion leads to energy loss and therefore many research groups do their best effort to understand how to control the motion of vortices once they are inevitably generated. In SRF cavities, vortex motion is also one of the main issues leading to degradation of the performance of Nb cavities in high field operation [57] [58]. Because vortex motion can produce a nonlinear electromagnetic response, measuring the nonlinear response due to the mechanism of vortex motion is one of the key studies in SRF materials research. We will return to this point in chapter V.

2.2.2 Other sources of extrinsic nonlinearity

In addition to extrinsic nonlinearity from moving vortices, many other extrinsic effects produce nonlinear response. The Josephson effect is probably the most significant extrinsic nonlinear factor. A Josephson junction is made of two superconductors connected by a "weak link" which can be a thin insulating barrier (known as a superconductor-insulator-superconductor junction, or S-I-S), a short section of non-superconducting metal (S-N-S), or simply a narrow physical constriction that weakens the superconductivity at the point of contact (S-C-S). In bulk Nb cavities, due to the the chemical etching process, oxides and hydrides will be naturally formed in the fabrication process and therefore different kinds of Josephson junctions will exist on the bulk Nb surface [49][50]. These junctions will degrade the value of critical current in pure Nb and result in the breakdown of superconductivity at a field level below the thermodynamic critical field [49][50][51].

Different defects on Nb surfaces will lead to Josephson junctions having critical currents lower than the bulk critical current J_c. Nonlinear effects of these kinds of Josephson junctions on Nb surfaces have aroused great concern in the SRF community. A phenomenological equation, similar to Eq. 2.5, can describe this nonlinear effect by introducing a temperature dependent nonlinear current density scale, $J_{NL}(T)$, [52] [53]

$$\left(\frac{n_s(T,J)}{n_s(T,J=0)}\right)^2 = 1 - \left(\frac{J}{J_{NL}}\right)^2 \tag{2.9}$$

Note that the nonlinear current density scale $J_{NL}(T)$ is a material parameter, here depending on different defects. Fig. 2.4 shows schematically the expected values of J_{NL} on the several defects found on bulk Nb surfaces. A nonlinear measurement on those defects will quantitatively identify their electromagnetic properties in high RF field.

Finally, one more thing worth to mention is that the J_{NL} term in Eq. 2.9 can also be interpreted as a general form for different types of nonlinear mechanisms and can quantitatively characterize the different mechanisms of nonlinearity, including intrinsic and extrinsic nonlinearity. For the intrinsic nonlinearity, J_{NL} includes the term of b_Θ in Eq. 2.5 and it's temperature dependence can be approximated by $J_{NL}(T) = J_c(1 - (\frac{T}{T_c})^2)(1 - (\frac{T}{T_c})^4)^{1/2}$ in the GL picture.

21

0.2 mm Ta Defect
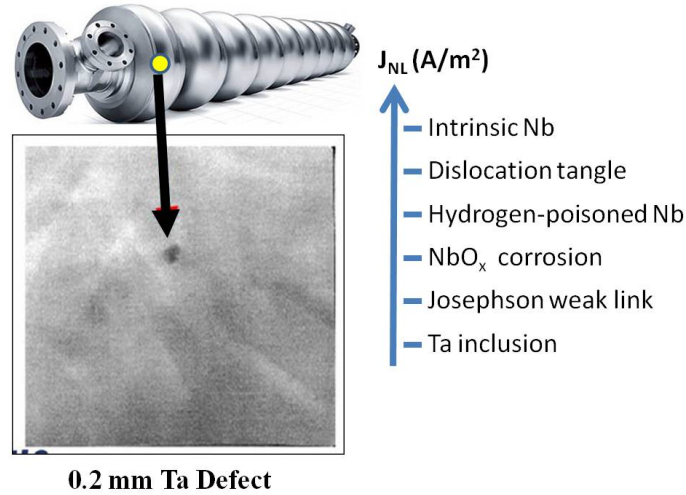
Fig. 2.4: Schematically expected values of J_{NL} for different types of defects on Nb cavities. Here a 9 cell cavity is shown and a representative Tantalum defect [59] from the fabrication process on the inner surfaces of the cavities are imaged by SEM.

2.3 Previous work on the electromagnetic properties of superconductors

Microwave experimental techniques have been widely used to study the physics of superconductors [54]. These experiments generally either measure the linear response or harmonic response by immersing the studied superconducting sample in a resonator cavity. In order to generate measurable nonlinear effects, the sample must be subjected to high microwave fields, a situation which can be achieved while the sample is placed at a location of maximum magnetic field inside the resonator cavity. In these experiments, researchers measure the resonant frequency shift and the temperature dependent or power dependent quality factor (Q) arising from changes in the properties of the sample [60][61][62]. For nonlinear microwave measurements,

22

many groups study the superconducting self-resonant samples such as superconductive spiral or stripline resonators to investigate the fundamental physics governing the superconducting quantum states. For instance, the intermodulation distortion (IMD) measurement on d-wave YBCO single crystal has been performed to prove the nonlinear mechanism arises from the gap nodal features on the Fermi surface [63]. However this kind of measurement can only monitor the spatially-averaged electromagnetic properties of the tested superconductor. The spatial resolution is limited by the length scale of the microwave wavelength and is impossible to get the localized microwave properties of the tested superconductors.

Based on the constraints of spatial resolution for far field measurement, the near field concept has emerged in recent years for microwave rf properties measurement. Many near-field microwave microscopes were developed to solve many practical problems in different research fields. In superconductivity, near field microwave microscopes were used to image the variation of T_c as well as the change of surface resistance as a function of the scanning probe position [64]. In our group, we built a novel near-field magnetic field microwave microscope to investigate the localized linear and nonlinear response of many high T_c superconducting cuprate samples [10] [11]. This experiment used a scanned magnetic loop probe to apply a focused local current distribution on the superconducting samples and investigate the local electromagnetic properties in the microwave frequency regime. A scanned magnetic loop probe is made by shorting the inner conductor and outer conductor of a commercial semi-ridge coax cable with inner diameter 200 μm and outer diameter 2 mm. The loop is brought to within 10 μm of the superconducting surface and

a high frequency current is applied to the loop. Our early work investigated the harmonic effects in YBCO films with various doping [53] and demonstrated temperature dependent phase sensitive properties in localized harmonic measurement [65]. Harmonic imaging of a single grain boundary Josephson tunnel junction also successfully resolved the localized source of nonlinearity [11] [12]. However the spatial resolution of the above achievement is not very high due to the large diameter of the loop size in the experiment. In this dissertation, we will show our effort to improve the spatial resolution down to the sub-micron scale by integrating a novel magnetic writer coming from the magnetic recording hard drive into the existing microscope [66]. Then we will study the linear and nonlinear responses investigated by this potential high resolution probe on SRF materials, including Nb thin films, bulk Nb and MgB_2 thin films.

3. INTEGRATION OF MAGNETIC WRITER INTO THE MICROWAVE MICROSCOPE

3.1 Introduction to the magnetic writer probe

Magnetic hard disk drives (HDDs) continue to be the primary high performance storage technology for non-volatile information recordings today. This success is due to the tremendous achievement in both read heads and write heads as well as the recording medium. Early HDDs used an electromagnet for both the read head and the write head to magnetize the bit region of the medium and then read its magnetic field by using electromagnetic induction. At that time, read and write elements shared the same electromagnet. Because of the need for increased data storage density, in the modern design of the hard drive, the hard drive head separates the write and read element to individually optimize the performance of both elements. For the read element, the giant magnetoresistance (GMR) effect came into use. This GMR head is more sensitive and can respond to the much smaller magnetic fields produced by the smaller written bits in the magnetic medium. More recently the tunneling magnetoresistance (TMR) read head has been used in HDD. The TMR head shows higher sensitivity than the traditional GMR read head.

For the write element, the write heads have progressed into a type of thin-

film inductive probe. These thin-film write heads (sometimes called the writer) are fabricated with several layers of lithography and film deposition. The main part of the writer is a yoke (magnetic head) surrounded by a few turns of helical wire coil which generates the magnetic flux as schematically shown in Fig. 3.1 (a) and (b) [67]. The yoke is usually made of high permeability materials such as ferrite or permalloy to channel the magnetic flux. The magnetic flux goes out through the small gap, usually 200 $nm \sim 100$ nm wide, at the end of the yoke. The first generation of thin-film inductive heads was a ring shaped head specifically for longitudinal recording as shown in Fig. 3.1 (a). Recently the design of the write head became a monopole-like shape for the developing high-density recording technology of perpendicular recording [68] as shown in Fig. 3.1 (b). This special shape design enables the write field to penetrate the recording medium more efficiently in the perpendicular geometry recording. Several studies of the high frequency characteristics of modern magnetic write heads shows well-confined fields on the length scale of several hundred nanometers at a few GHz frequency [21] [22] [69]. These characteristics enable us to achieve sub-micron resolution in the GHz frequency region in the design of our near-field microwave microscope.

Figure 3.2 shows the final merged read/write head assembly of current-day design. The read/write sensor is centered on the front edge of the slider. The slider is designed to control the flying height of the read/write sensor over the magnetic medium via an etched air-bearing face onto the disk-facing plane. Hence, the slider is what actually floats or slides over the surface of the disk, carrying the read/write head at the correct distance from the magnetic medium for reading and writing.
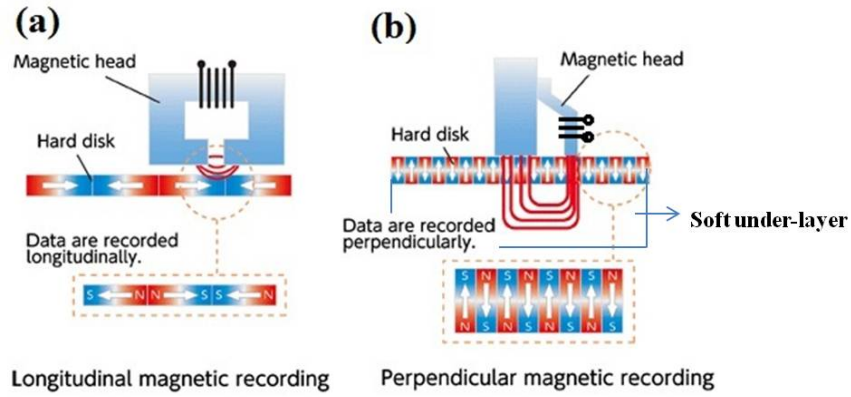
Fig. 3.1: (a) A ring shape magnetic write head on the longitudinal magnetic recording medium. (b) A monopole-like shape magnetic write head on the perpendicular magnetic recording medium. The flux comes out from the monopole terminal, then penetrates into the medium and is channeled by a soft underlayer before it returns to the other terminal of the head. This figure comes from the reference [67].

The surface of the slider body is coated with a nano-scale $(TiC)Al_2O_3$ layer [70]. This layer is as hard as rock to prevent the damage to the probe in case of any accidental crash during the read/write process. Therefore, the probe itself is very robust for my scanning probe application in the near field microwave microscope.

In our research, a magnetic write head (writer) is utilized to generate a strong and localized RF magnetic field, and to enhance the spatial resolution of our near
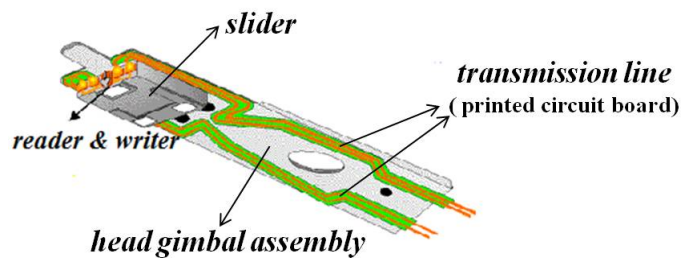
Fig. 3.2: General probe assembly inside the hard drive. The position of read head and write head are pointed out. The transmission lines carry the high-speed signals to and from the writer/reader.
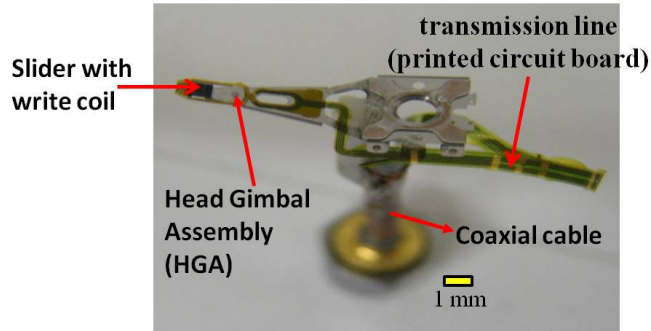
Fig. 3.3: A probe assembly is soldered on the coax cable. The probe assembly in the picture is a GT5 probe from Seagate company.

field magnetic microwave microscope. Taking advantage of magnetic write head technology with write-gap widths on the order of 100 nm [71], an RF field on the scale of 1 Tesla [72] with sub-micron spatial extent [73] can be created. In this work, we integrate the magnetic writer probe into our microwave microscope by soldering the probe assembly onto a coaxial cable as shown in Fig. 3.3.

Three kinds of probe assembly are used in this research and they are tabulated in Table 3.1. Note that due to trade secrecy and confidential information of the hard drive manufacturers, the exact specification of each probe is unpublished. Generally, the dimension of magnetic write-gap width is from 100 nm to 1 μm depending on the age of the technology. The Quantum Big Foot hard drive [74] was manufactured in the mid to late 1990s and we believe the probe from this hard drive has the largest gap compared to the other two probes. Perpendicular recording is the latest technology in the hard drive industry, therefore, the width of write-gap from the PINNACLE probe should be the smallest of the three.

Table 3.1: Catalog of Write Heads Used in Our Experiments			
Probe Assembly	Manufacturer	Read/Write Mechanism	Year
Probe from Quantum Bigfoot Hard Drive	Quantum Corp.	Longitudinal Recording	mid-to late-1990's
GT5 Probe	Seagate	Longitudinal Recording	circa 1998's
PINNACLE Probe	Seagate	Perpendicular Recording	greater 2007
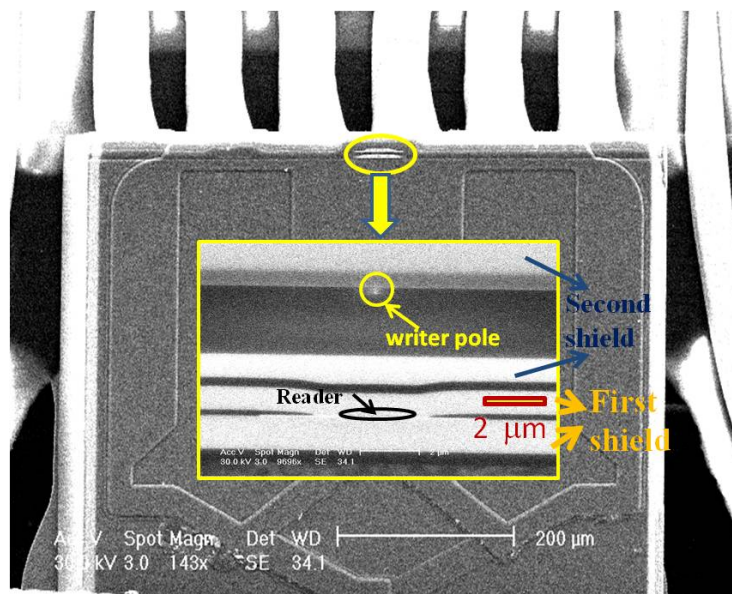
Fig. 3.4: SEM image of the PINNACLE probe slider assembly showing the media-facing surface. The center inset is a zoomed-in picture of the merged read/write head. The read element (read head) and write element (write head) are separated by magnetic shields. The reader is between the first magnetic shield, and the writer pole can be seen below the second shield.

A representative SEM image of the probe assembly is taken on the PINNACLE probe and shown in Fig.3.4. The read and write element can be clearly seen in the centered inset. The read element consists of a GMR sensor between two magnetic shields. These magnetic shields greatly reduce unwanted magnetic fields coming from the disk. Therefore the GMR sensor essentially "sees" only the magnetic field from the recorded data bit to be read. The inductive write element is a tiny 200 nm monopole shape. The second magnetic shield also functions as the other pole of the inductive write head. Due to the narrow width of the gap between two poles (not clearly seen in the SEM images due to the interference of the e-beam with the magnetic field), this writer probe has great potential for high resolution linear and nonlinear Meissner effect microscopy and in the future will be used in analyzing defects on Nb cavity surfaces at high frequencies and low temperatures.

3.2 Magnetic Write Head Behavior at Microwave Frequencies

Measuring the write head behavior at microwave frequencies is challenging but important. This can let us know the frequency regime of operation for the writer and whether it is compatible with our existing microwave system. Before integrating the magnetic write head into our near field microwave microscope, we measured the complex load impedance that the head presents to the microwave generator. Fig. 3.5 shows the impedance measured with a calibrated Picoprobe touching the contact pads on the slider. Note that this representative data is from the GT5 probe. Remarkably, the write head is very well impedance matched to 50 Ω in resistance
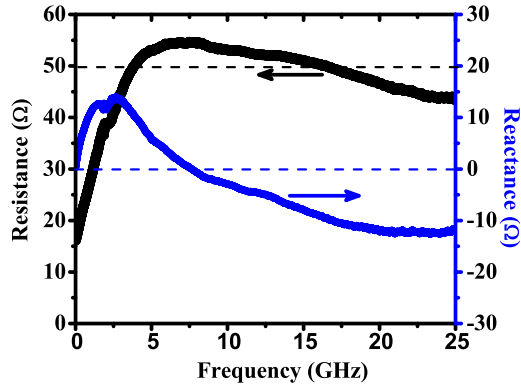
Fig. 3.5: Measured input impedance of the GT5 magnetic write head as a function of frequency. The thick line indicates the resistance, and the thin blue line indicates the reactance values. The measurement is done with a PNA-X N5242A network analyzer and calibrated Picoprobe at room temperature. The dashed lines show the characteristic impedance of the microwave generator $Z_0 = 50 \ \Omega$.

and 0 Ω in reactance over a broad frequency range from about 2 GHz to 25 GHz, which is quite ideal for the present application. Such good impedance match implies that we can deliver 45 mA of current to the write head using 100 mW (+20 dBm) of RF power, and we find that this does not burn out the magnetic write head coil.

3.3 HFSS simulation results on the write head at high frequencies

The electromagnetic fields produced by the near-field probe on the superconducting surface can be visualized by a finite element simulator, ANSYS High Frequency Structure Simulator (HFSS). Fig. 3.6 shows the model based on the dimensions of the Seagate GT5 magnetic writer. In this simulation, the sample is assumed to be a perfect electric conductor, not a superconductor. The 10 turn coil is stimulated with a 50 mA drive current at 4.5 GHz excitation frequency. The height of the probe is 200 nm from the surface of the sample. The magnetic flux induced

31
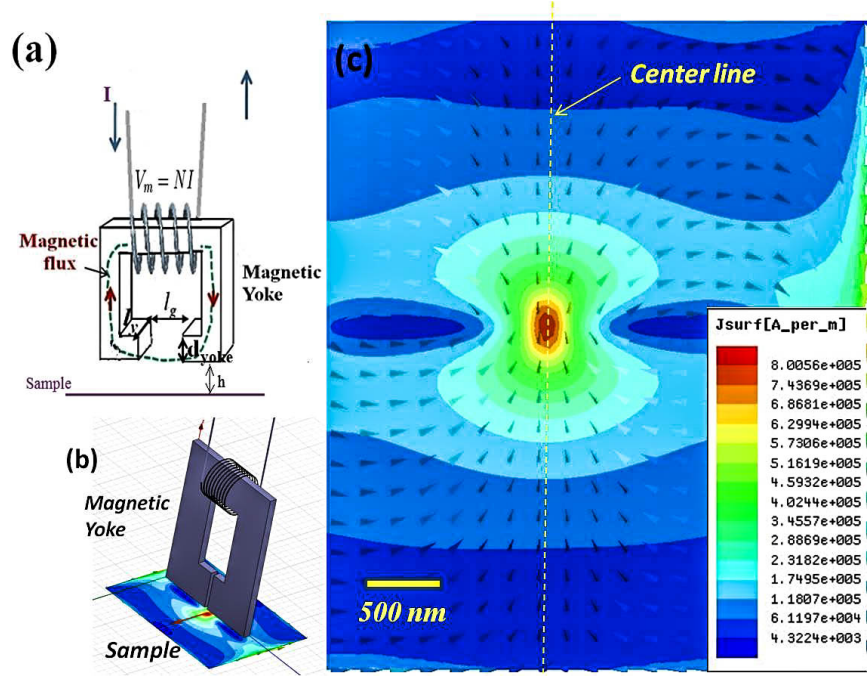
Fig. 3.6: (a) A schematic magnetic writer and the gap (not to scale) with a height (h) away from the sample surface. In our design, we assume l_g=100 nm, l_y=200 nm, and d_{yoke}=1 μm based on the dimension of the Seagate GT5 magnetic writer. (b) Configuration of HFSS simulation of a magnetic writer above a perfectly conducting sample. (c) Distribution of the surface current density (J_{surf}) on the sample surface. The J_{surf} scale bar and arrows indicate the magnitude and direction of the screening current, respectively, in the first half of the RF cycle. In this simulation, we assume the yoke is made of ferrite. The yoke is excited by a 50 mA RF current and the separation (h) between the probe and the sample is 200 nm. Note that a J_{surf} of $8 * 10^5$ A/m corresponds to a surface magnetic field B=460 mT.

by the incident signal goes out through the gap, about 100 nm long (l_g), $\sim$ 200 nm wide (w), at the end of the yoke. The thickness of the yoke (g) is 1 μm, with a 10 turn gold coil wrapped around it. The sample develops screening currents with a direction perpendicular to the direction of magnetic flux on the sample surface. The screening current on the sample surface has the pattern of a dipole. This screening response is essentially the same as that developed due to a horizontally-oriented point magnetic dipole at the location of the gap [75].

The surface magnetic field along the center line, shown as a dashed line in Fig.
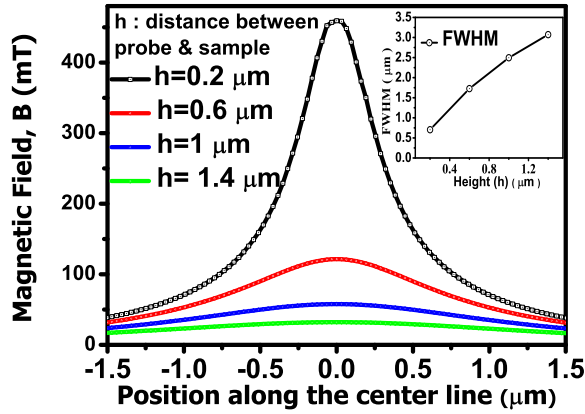
Fig. 3.7: Microwave magnetic field (B field) magnitude on the sample surface calculated by HFSS along the dashed center line on the sample in Fig. 3.6. The origin of the sample lies exactly below the center of the gap and shows the maximum magnetic field. The calculation is repeated at various heights (h) of the probe above the surface. The inset shows the Full Width Half Maximum (FWHM) of the field distribution as a function of height, showing that field concentration is stronger at smaller probe/sample distances.

3.6 (c), is plotted in Fig. 3.7 for different heights (h) between the probe and the sample. From the simulation result for a height of 200 nm, the maximum magnetic field (B field) on the surface is 459.2 mT, higher than the thermodynamic critical field of Nb ($\sim 200\ mT$). It is clear that the closer the probe to the sample (see the inset), the stronger and more concentrated the magnetic field on the surface. Therefore we want our magnetic writer as close as possible to the sample. The actual yoke geometry of the write head is not quite the same as the simple structure schematically shown in Fig. 3.6 (a) and (b). Although this simulation cannot describe the GT5 magnetic writer in detail, it provides a general trend and prediction for our microscope.

3.4   Equipment Overview

The magnetic write head probe described above is housed in a high vacuum cryogenic chamber as shown in Fig. 3.8. This chamber is a cryogenic probe station made by Desert Cryogenics. A continuous flow mechanism is used to cool the cold head down to 4.2 K by transferring liquid Helium from a Liquid Helium dewar into the bottom of the cold head through the liquid Helium transfer line (without pumping the Helium exhaust). The entry point of the liquid Helium transfer line and the Helium exhaust line are shown in the inset (b) of Fig. 3.8. The vacuum pressure of this chamber can be as low as $5 * 10^{-8}$ Torr at cryogenic temperatures. The microwave synthesizer, spectrum analyzer and temperature controller are shown in inset (a) of Fig. 3.8. Microwave current is generated by the microwave synthesizer and is conveyed into the probe in the chamber through the coaxial cable feed-through. The probe assembly and samples can be seen from the view port of the chamber through the optical microscope. The view inside the chamber is shown in Fig. 3.9. The probe stage is thermally anchored via high thermal conductivity copper braids. The microwave circuits for our microwave measurement on superconductors will be discussed in detail in the later chapters.
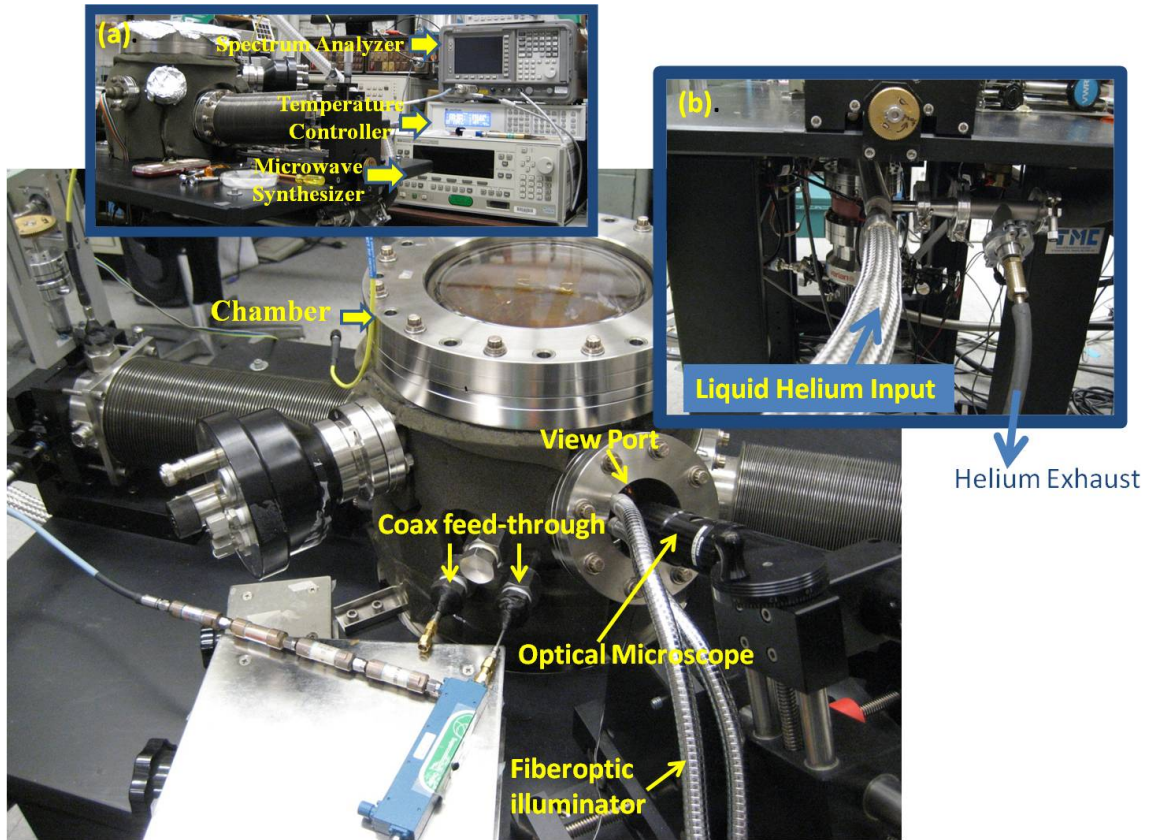
Fig. 3.8: Exterior pictures of the Desert Cryogenics probe station which houses the near field magnetic field microwave microscope. Inset (a) shows the spectrum analyzer, microwave synthesizer and the temperature controller. Inset (b) shows that the liquid Helium transfer line is inserted into the liquid Helium entry point. The Helium exhaust line is also labeled.
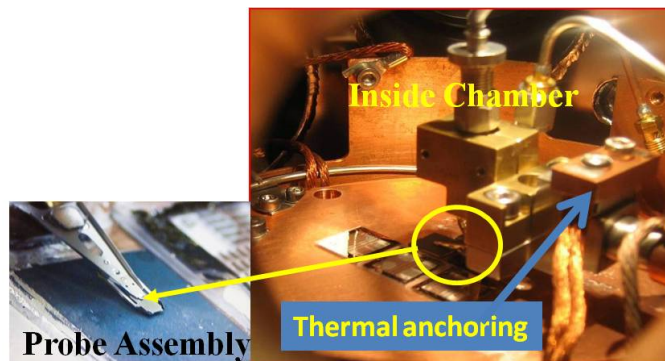
Fig. 3.9: Interior pictures of the Desert Cryogenics probe station. The probe assembly is held by a probe arm. Inset shows the magnetic write head probe assembly on top of a superconducting thin film. The thermal anchoring links to the probe assembly to enhance the thermal contact of the magnetic probe and insure that it achieves a temperature close to that of the sample.

4. LINEAR RESPONSE MEASUREMENT

4.1   Linear Response Setup

A linear response measurement on superconductors would help us to understand the basic properties of RF superconductivity, such as the critical temperature, surface resistance and penetration depth. Understanding these properties would let scientists make the best use of superconductors in different applications.

The schematic setup for linear response measurements is shown in Fig.4.1(a). A microwave fundamental tone (V_{a1}^+) is sent into the magnetic writer (either Seagate GT5 or PINNACLE probe) from port 1 of the vector network analyzer (VNA) (model $\sharp$ Agilent N5242A). We measure the linearly reflected signal in port 1 of the VNA.

The process is now discussed in more detail. The magnetic writer used in this measurement includes GT5 & PINNACLE probes and each probe is integrated into our microwave circuit by soldering the probe assembly on a coaxial cable (see Fig. 3.3). For each probe, the main part of the writer is a magnetic yoke surrounded by a several-turns helical coil which generates the magnetic flux. The yoke is made of a high permeability material (usually ferrite) to channel the magnetic flux to the narrow gap. It is also shielded to define a nano-scale bit in the recording medium

during the writing process [21] [22] [76]. Close-up views of the magnetic write head probe on superconducting samples are also shown on the side of Fig. 4.1. In our design, the magnetic writer approaches the surface of the superconductor in the range of 200 $nm \sim 2~\mu m$. The fundamental tone stimulates the magnetic writer to generate an RF magnetic field and therefore excites a screening current on the sample surface so that it can maintain the Meissner state in the bulk of the material. Larger magnetic field induces higher screening current within the penetration depth (λ) of the superconducting surface, until the field reaches the critical field of the material. The time dependent screening current on the superconductor will induce an electromotive force (emf) back on the magnetic writer. (Note that we do not measure the reader because it is too far away from the localized excitation on the surface of the superconductor.) The emf voltage will couple with the incident fundamental tone and reflect back as an output signal (V_{b1}^-). We measure the ratio of V_{b1}^- to V_{a1}^+ (S_{11}) at different temperatures of the superconducting samples. The sample temperature is controlled by a Lakeshore 340 temperature controller.

The superconducting samples we study are Nb thin films with thickness 50 nm that I made by sputtering Nb onto 3 inch diameter quartz wafers. After the deposition, the wafer is diced into many 10*10 mm^2 pieces but otherwise left undisturbed. The Nb sample is well anchored to the cold plate to ensure that the surface temperature of the superconductor is the same as the temperature of the cold plate. The probe is held by a three axis translatable arm. Hence different points on the surface of the sample can be examined in the same cool-down. We tested many pieces (at least 3 to 5) from each Nb wafer, and all pieces show consistent

37
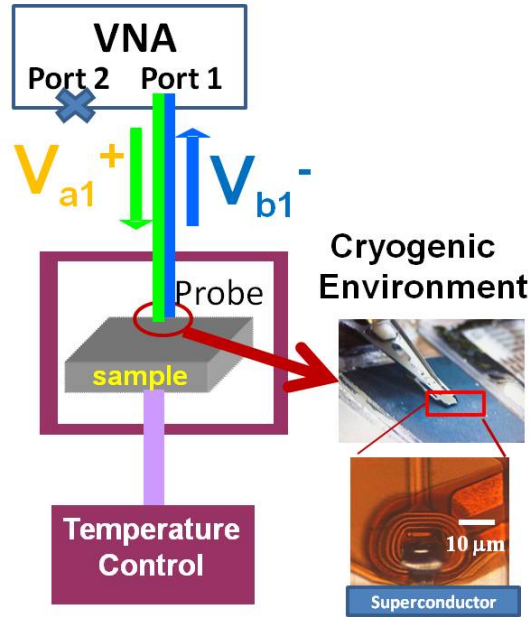
Fig. 4.1: Schematic diagram of the linear response measurement, S_{11}, performed as a function of temperature with the (VNA). The reflected signal and incident signal are at the same frequency.

results for their linear response measurement.

4.2   Linear Response Results on Nb Thin Film

Many single-position measurements on different 50 nm thick Nb samples were performed by two different writer probes, the GT5 and PINNACLE probes. The different probes have different resonant frequencies after integrating the probe to the microwave system. Before cooling down to measure the Nb superconductivity reflection signal, an electronic calibration (Ecal) is performed at the end of the flexible coaxial cable at ambient temperature and ambient pressure. Fig. 4.2 schematically illustrates the location where Ecal is performed. The probe assembly cannot be calibrated with Ecal in the measurement. After drawing a vacuum, the cooling down procedure is followed and it takes a couple of hours to stabilize temperature down
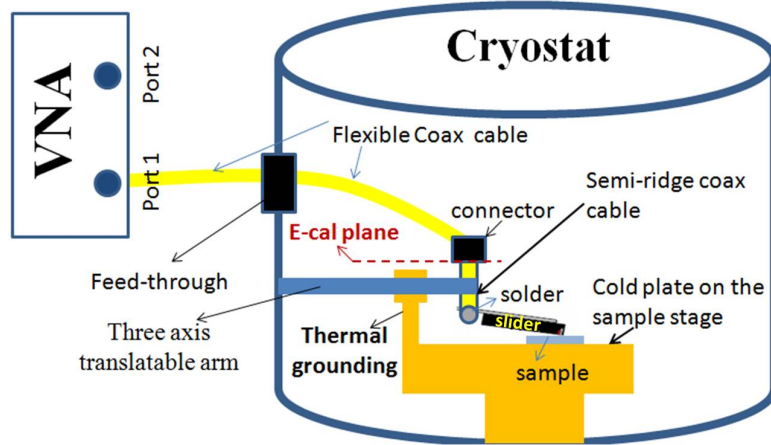
Fig. 4.2: Schematic illustration of the linear response measurement setup. The VNA at room temperature is connected to the sample at low temperature through a coaxial cable and magnetic write head. Note the Ecal calibration plane location, which is at the end of the flexible coaxial cable. Ecal is done at ambient temperature and pressure.

to almost 4.2 K (without pumping on the helium exhaust). The measurement are then performed.

Fig. 4.3 (a) and Fig. 4.3 (b) show the frequency dependent S_{11} measurement of the PINNACLE and GT5 probe, respectively, under -15 dBm (considered lower power) excitation and at a single-position on one of the Nb films. The measurements are at two different temperatures: one temperature is at the Nb normal state (10 K) and the other is at the Nb superconducting state (below the T_c of the film). The probe-sample separation is estimated to be on the order of $0.2 \sim 5 \ \mu m$. First, one can clearly see that the frequency positions of the resonant dips of the measurement with the GT5 probe and the PINNACLE probe are different. For the PINNACLE probe measurement, the deepest dip happens around 2 GHz, at which the maximum rf magnetic field at the sample can be generated. For the GT5 probe measurement, the deepest dip is around 4.7 GHz. The dip position also depends on the height
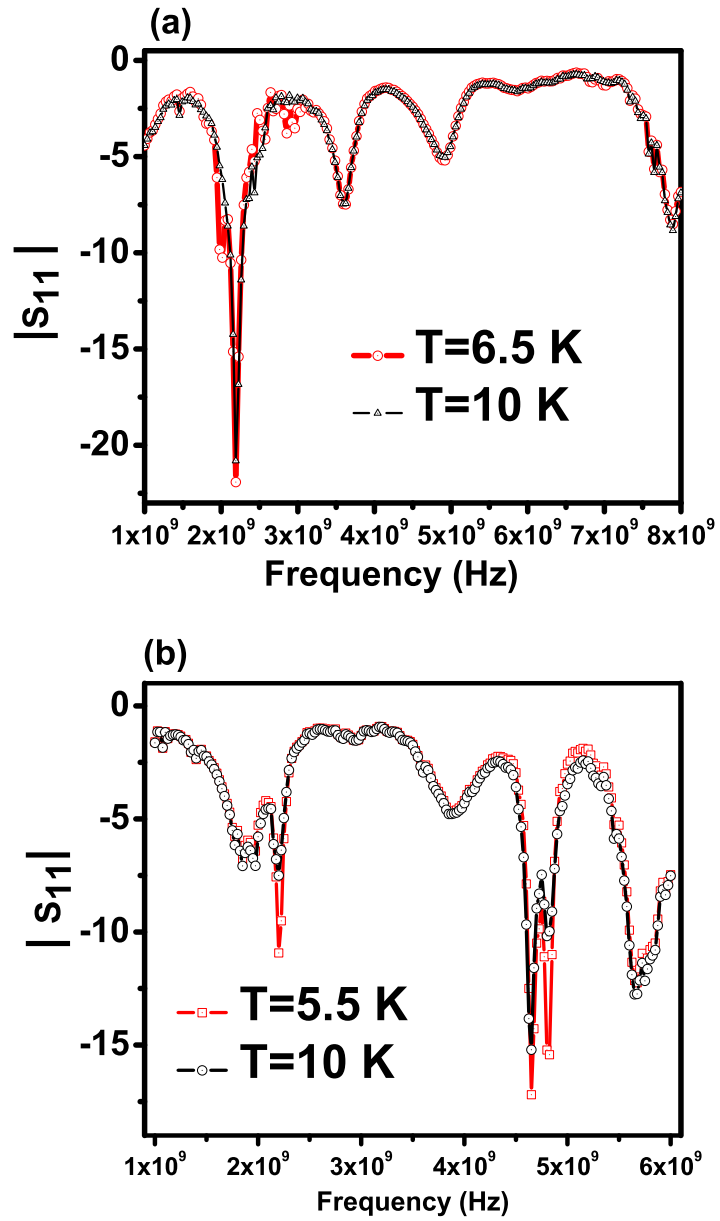
Fig. 4.3: Frequency dependence of $|S_{11}|$ in dB measured at two different temperatures by the PINNACLE probe (a) and the GT5 probe (b), respectively. The sample under test is a Nb thin film with thickness 50 nm and T_c=8.3 K. The excitation power in both measurements is -15 dBm. Note $|S_{11}|$ is plotted on a log scale.

between the probe and the superconducting sample, implying different coupling between the sample and the probe. Second, the amplitude of the deepest dip is very sensitive to the superconducting transition temperature of the Nb films. One can see an obvious change of S_{11} amplitude at the dip position when the sample becomes superconducting. This measurement can determine the best excitation frequency for both the linear and the nonlinear superconductivity measurement.

Fig. 4.4 (a) shows the amplitude and phase of a temperature dependent S_{11} measurement at a single-position on one of the Nb films under -15 dBm, 1.98 GHz excitation by the PINNACLE probe. The same measurement by the GT5 probe at -15 dBm, 4.82 GHz excitation is also shown in Fig. 4.4 (b). Note that the excitation frequency in the measurement is decided by the resonant dip in the frequency dependent S_{11} measurement. For both measurements, a sharp change of S_{11} occurs at 8.3 K for both the amplitude and phase. This change indicates the Nb transition temperature (T_c). Physically, at this temperature, the Nb thin film becomes superconducting and generates a strong screening current on the sample surface which couples with the incident voltage (V_{a1}^{+}) and results in a change of the reflected voltage (V_{b1}^{-}). In addition, from the normal state to the superconducting state, the surface resistance suddenly drops to a value closer to zero. A magnetic circuit model is provided below to quantitatively interpret the temperature dependent S_{11} measurement.
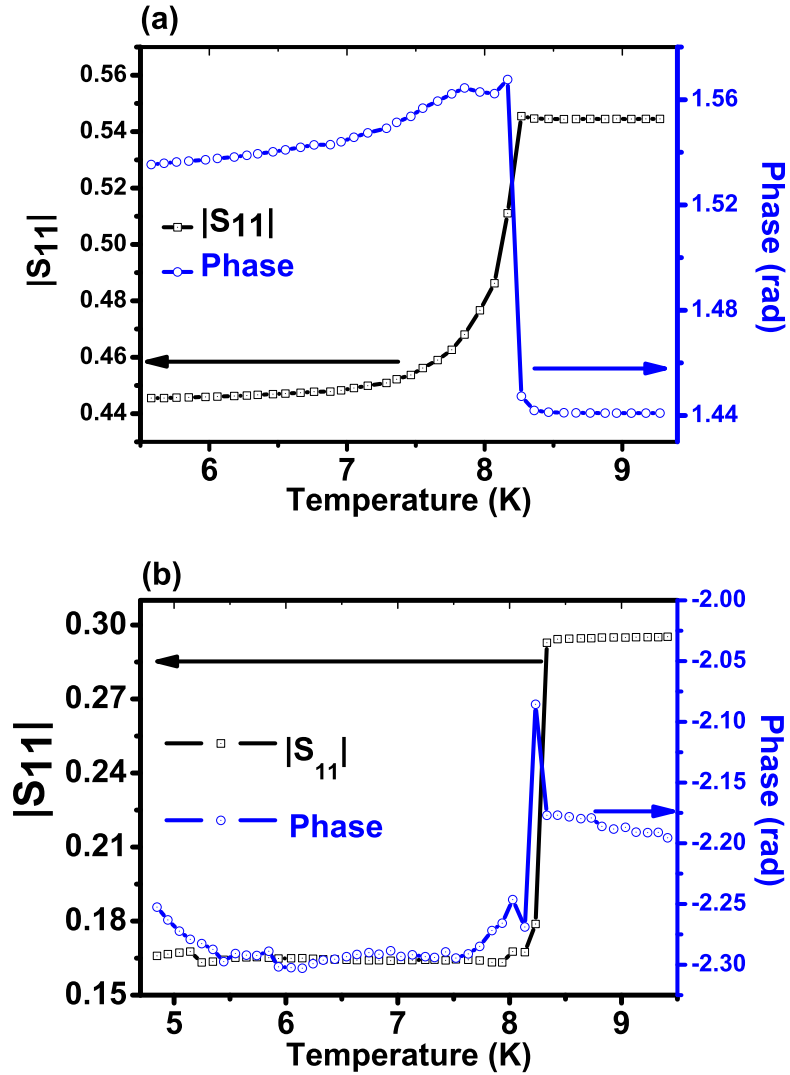
Fig. 4.4: (a) The temperature dependent S_{11} of a 50 nm Nb thin film measured with the near-field microwave microscope via the Pinnacle probe at 1.98 GHz (b) The temperature dependent S_{11} of a 50 nm Nb thin film measured with the near-field microwave microscope via the GT5 probe at 4.82 GHz. From (a) and (b), both amplitude and phase show a transition at 8.3 K, the same temperature as a global AC susceptibility measurement on this sample. Note $|S_{11}|$ is plotted on a linear scale.

4.3   Modeling the Linear Response Measurement [1]

For modeling this $S_{11}(T)$ measurement, a perfect Meissner state in the superconductor is assumed while the temperature is below T_c. The magnetic yoke is wrapped by an N-turn solenoid to channel a magnetic flux, Φ, down to the gap as illustrated in Fig. 4.5 (a). The separation between the probe and the sample is assumed to be small compared to the magnetic gap length (l_g) and can be ignored in the model. While exciting the surface of a superconductor by the magnetic probe, there are two channels for flux in the magnetic circuit: the air gap and the penetration depth of the superconductor. Since the total flux, Φ, provided by the yoke of the magnetic write-head distributes among these two channels, they should be represented by two parallel reluctances, R_g and R_s, as shown in Fig. 4.5 (b). The gap reluctance, R_g, follows the conventional geometric definition of reluctance

$$R_g = \frac{l_g}{\mu_0 A_{gap}} = \frac{l_g}{\mu_0 l_y d_{yoke}} \qquad unit : H^{-1} \tag{4.1}$$

where l_g is the gap length of the yoke, A_{gap} is the cross-section area of the air gap, d_{yoke} is the thickness of the yoke, l_y is the the size of the yoke in the transverse dimensions. The Meissner state reluctance R_s is generated due to the penetration of magnetic field into the superconductor within its penetration depth. Therefore, the total flux will shunt into two branches, Φ_s with its reluctance R_s and Φ_g with

---

[1]This model was worked out in collaboration with Dr. Behnood G. Ghamsari
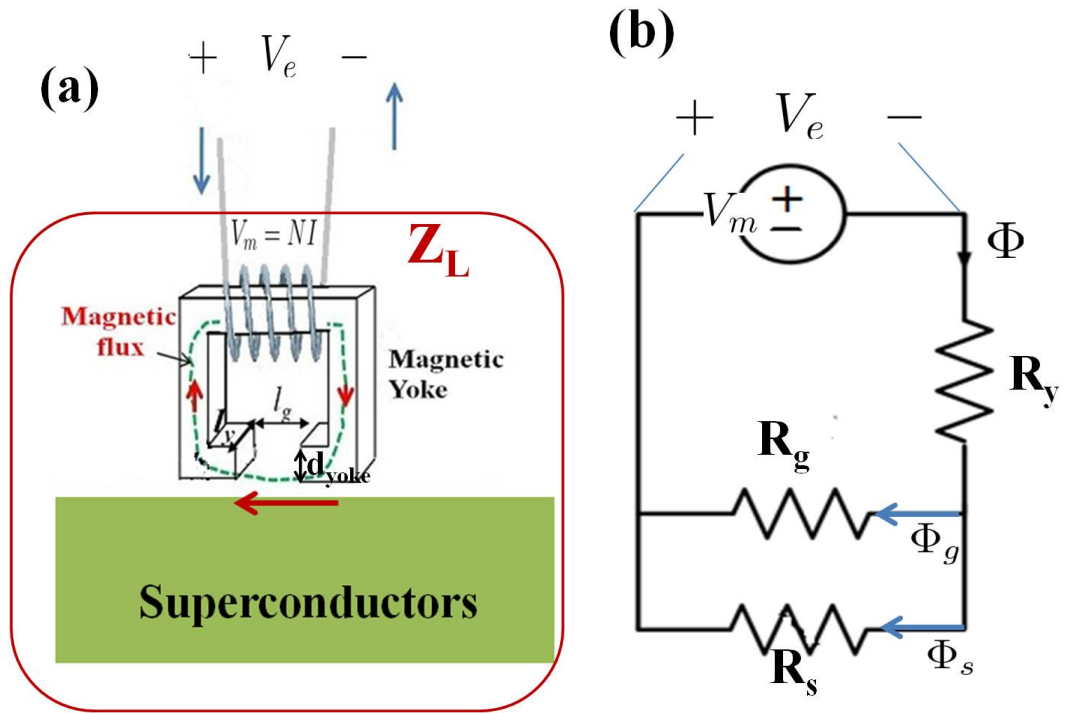
Fig. 4.5: (a) A schematic of the experiment where a magnetic probe locally excites the surface of a superconductor with a time-varying magnetic field. The total scene can be modeled as a total load impedance, Z_L. This figure uses the ring shape magnetic yoke to represent the writer. l_g indicates the length of the gap under the bottom of the magnetic yoke. d_{yoke} is the thickness of the magnetic yoke and l_y is the size of the yoke in the transverse dimensions. V_m is the impressed voltage created by the N turn solenoid with input current I. V_e is the induced electric voltage on the input winding. (b) The equivalent **magnetic circuit** of the experiment with a superconducting sample and the magnetic probe. Φ_g is the magnetic flux going through the gap reluctance R_g and Φ_s is the magnetic flux going through the superconducting sample with the reluctance R_s in the Meissner state. Φ is the total flux. V_m and V_e have their the same description as Fig. 4.5 (a).

its reluctance R_g. In the linear Meissner state, we obtain

$$\Phi_g = B * A_{gap} = B * (l_y * d_{yoke}) \qquad ; \qquad \Phi_s = B * (l_y * \lambda(T)) \qquad (4.2)$$

where B is the amplitude of the applied RF magnetic field in the gap (assumed to be the same field witnessed by the sample) and $\lambda(T)$ is a temperature dependent penetration depth. By applying the node-voltage law, we have $\Phi_g R_g = \Phi_s R_s$. Hence, the reluctance of the linear Meissner state is given by

$$R_s = \frac{d_{yoke}}{\lambda(T)} R_g \qquad where \qquad R_g = \frac{l_g}{\mu_0 l_y d_{yoke}} \qquad (4.3)$$

So the total reluctance in this magnetic circuit is

$$R_{eq} = R_y + R_g//R_s = R_y + \frac{d_{yoke}}{d_{yoke} + \lambda} R_g = \left(\frac{\mu_0}{\mu_f} + \frac{d_{yoke}}{d_{yoke} + \lambda} \right) R_g \qquad (4.4)$$

where R_y is the reluctance of the magnetic yoke and can be approximated as $\frac{\mu_0}{\mu_f} R_g$, here μ_0 and μ_f indicate the permeability of the vacuum and the magnetic yoke, respectively. By solving the magnetic circuit in Fig. 4.5, one finds the magnetic flux flowing through the magnetic circuit will, in turn, give the induced electric voltage into the input winding through Faraday's law

$$V_e = \frac{d\Phi}{dt} = \frac{d}{dt} \left(\frac{V_m}{R_{eq}} \right) = \frac{d}{dt} (\frac{NI}{R_{eq}}) = \frac{iN\omega I_0 e^{i\omega t}/R_g}{\mu_0/\mu_f + d_{yoke}/(d_{yoke} + \lambda(T))} \qquad (4.5)$$

where V_m is the impressed voltage on the magnetic circuit and can be written as

$V_m = NI$. Here N is the number of turns in the solenoid and I indicates the RF input current with a maximum amplitude I_0 in an RF cycle ($I = I_0 e^{i\omega t}$). Therefore the impedance of the magnetic circuit can be found as $\frac{iN\omega/R_g}{\mu_0/\mu_f + d_{yoke}/(d_{yoke}+\lambda(T))}$. To evaluate the load impedance, Z_L , one should include the impedance coming from the normal state of the superconductor and the rest of the probe circuit to get

$$Z_L = Z_{Bkd} + \frac{i\omega N/R_g}{\frac{\mu_0}{\mu_f} + \frac{d_{yoke}}{d_{yoke}+\lambda(T)}} \quad ; \quad Z_{Bkd} \equiv R_{Bkd} + iX_{Bkd} \qquad (4.6)$$

where R_{Bkd} and X_{Bkd} represent the background resistance and background reactance of the load impedance, respectively (i.e. these parameters model the background probe-dependent properties of the write head). In addition, while the film thickness is smaller than the penetration depth, the regular penetration depth should be replaced by an effective penetration depth, λ_e [77]

$$\lambda(T) \to \lambda_e(T) = \frac{\lambda^2(T)}{d_{film}} \qquad (4.7)$$

where d_{film} is the thickness of the film and it is assume that $d_{film} \ll \lambda$.

In the experiment schematically shown in Figs. 4.2 and 4.5(a), the probe load impedance (represented now by Z_L) is connected to a printed circuit board and then a semi-ridge coax cable of finite length is soldered to the contacts of the printed circuit board. The length of the printed circuit board plus the length of semi-ridge coax cable can be combined together and treated as a transmission line of length l on the probe assembly. One can model a microwave circuit of transmission line terminated
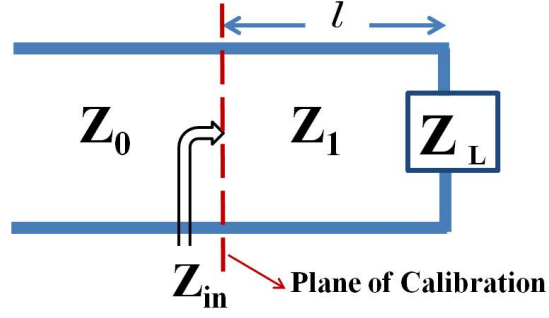
Fig. 4.6: Model the impedance looking into a magnetic write head probe at the end of a short segment of transmission line. Z_0 indicates the characteristic impedance of the calibrated transmission line (50 Ω). Z_1 is characteristic impedance of probe transmission line (usually NOT 50 Ω) with length l. Z_L represents the load impedance including the impedance of the magnetic probe head and a superconducting sample.

by Z_L as shown in Fig. 4.6. This shows a microwave circuit of transmission line terminated in the derived load impedance from the magnetic circuit model with a length l on the probe assembly. In this one port measurement, the E-cal calibration is done only on the transmission line from the part of the flexible coax cable shown in Fig. 4.2 but not on the probe assembly. Therefore a characteristic impedance mismatch between the calibrated transmission line and the un-calibration part will be inevitable. Here Z_0 represents the characteristic impedance of the calibrated transmission line, 50 Ohms in our case, and Z_1 is the characteristic impedance of the un-calibrated transmission line on the probe assembly with a length of l. Both Z_0 and Z_1 are real. In this circumstance, the input impedance, Z_{in} is the impedance at the plane of calibration, given by,

$$Z_{in} = Z_1 \frac{Z_L + jZ_1 tan(\gamma l)}{Z_1 + jZ_L tan(\gamma l)} \qquad where \qquad \gamma = \beta - i\alpha = \frac{n\omega}{c} - i\alpha \qquad (4.8)$$

Here n is the refractive index of the transmission line of length l, ω is the angular

47

Tab. 4.1: A transformation from the experimental S_{11} data to a single vector $\mathbf{y}$

T	S_{11} (Experiment)
T_1	$\alpha_1 + \beta_1 \, \mathrm{i}$
T_2	$\alpha_2 + \beta_2 \, \mathrm{i}$
$\vdots$	$\vdots$
T_j	$\alpha_j + \beta_j \, \mathrm{i}$

$\Longrightarrow$

T	y
T_1	α_1
T_2	α_2
$\vdots$	$\vdots$
T_j	a_j
$T_1 + T_c$	β_1
$T_2 + T_c$	β_2
$\vdots$	$\vdots$
$T_j + T_c$	β_j

frequency and α is an attenuation coefficient inside the transmission line. Finally the theoretical S_{11} based on this model can be defined as

$$S_{11} = \frac{Z_{in} - Z_0}{Z_{in} + Z_0} \tag{4.9}$$

Complex curve fitting of this model to the $S_{11}(T)$ data is performed by the least square method to minimize the difference between the experimental temperature dependent S_{11} values and the values predicted by the model. In order to simultaneously fit both the amplitude and phase of the experimental $S_{11}(T)$ data, the complex data are separated into a real part and an imaginary part. Then a single vector $\mathbf{y}$ is created by concatenating the real and the imaginary parts from the measured data as shown in Table 4.1. Here $\alpha_1, \alpha_2, \cdots, \alpha_j$ are the real parts of the experimental S_{11} data and $\beta_1, \beta_2, \cdots, \beta_j$ are the imaginary parts of the experimental S_{11} data. $T_1, T_2, \cdots, T_j$ are the corresponding discrete temperature values from the experiment. The newly created function, $\widehat{S}_{11}$, from the model is used to

Tab. 4.2: The generated $\widetilde{S_{11}}$

	T	S_{11} (Model)
	T_1	$a_1 + b_1$ i
	T_2	$a_2 + b_2$ i
	$\vdots$	$\vdots$
$\widetilde{S_{11}}$	T_j	$a_j + b_j$ i
	$T_1 + T_c$	$a_1 + b_1$ i
	$T_2 + T_c$	$a_2 + b_2$ i
	$\vdots$	$\vdots$
	$T_j + T_c$	$a_j + b_j$ i

find the minimum least square between vector $\mathbf{y}$ and the $\widehat{S}_{11}$

$$Minimum\left(|\widehat{S}_{11}(coef, T) - \mathbf{y}|^2\right) = Minimum\left(\sum_j (\widehat{S}_{11}(coef, T_j) - \mathbf{y_j})^2\right) \quad (4.10)$$

where '$coef'$ indicates the unknown coefficients in the theory, j indicates the temperature dependent discrete index in the calculation. The newly created $\widehat{S}_{11}$ based on the theoretical model is given by

$$\widehat{S}_{11} \equiv (1 - H(T - T_c)) * real\left[\widetilde{S_{11}}(T)\right] + H(T - T_c) * imag\left[\widetilde{S_{11}}(T - T_c)\right]$$

$$where \quad H(T - T_c) = \begin{cases} 0 & \text{for } T \leq T_c \quad (4.11) \\ 1 & \text{for } T > T_c \end{cases}$$

where $H(T - T_c)$ is a Heaviside step function, "$real$" and "$imag$" indicate the real part and imaginary part of the data, respectively. The $\widetilde{S_{11}}$ is a set of numerical values which is created from the S_{11} theoretical model and then the created S_{11} is copied to generate the same set of numerical values when $T > T_c$ as shown in Table

4.2. Note that $a_1, a_2, \cdots, a_j$ and $b_1, b_2, \cdots, b_j$ are the real parts and the imaginary parts of the calculated S_{11} from the model, respectively, at the desired temperatures, $T_1, T_2, \cdots, T_j$. Therefore, when $T < T_c$, the real part of S_{11} is left in the new $\widetilde{S_{11}}$ function to be fitted. On the other hand, while $T > T_c$, only the imaginary part of S_{11} is taken for fitting. This way one can effectively find a solution simultaneously for both the amplitude and phase of S_{11} in our measurement.

In our experiment, the index of refraction of the Teflon inside the coax cable is taken to be $n \approx 1.2$, almost independent of the excitation frequency. The uncalibrated length of the transmission line is around 5~6 cm. Conveniently, we combine the n and l together to treat them as a constant term $nl = 0.065\ m$ in the fitting calculation. On the other hand, the coefficient α (unit: m^{-1}) and l (unit: m) are bundled together as a dimensionless fitting unknown parameter. The thickness of the yoke is assumed to be a constant, d_{yoke}=500 nm, the average thickness in the fabrication of modern inductive thin film writers. The temperature dependence of an effective penetration depth, λ_e is approximately described by [77]

$$\lambda_e(T) \approx \frac{\left(\lambda(0)\left[1 - (T/T_c)^4\right]^{-\frac{1}{2}}\right)^2}{d_{film}} \tag{4.12}$$

where $\lambda(0) = 40\ nm$ is the 0 K penetration depth of Nb and $d_{film} = 50\ nm$ is the known thickness of the measured Nb thin film. Therefore, based on the model, the unknown coefficients in the experiment are αl, Z_1, R_{Bkd}, X_{Bkd}, N/R_g and μ_0/μ_f.

The first fit is done on the data set measured by the PINNACLE probe
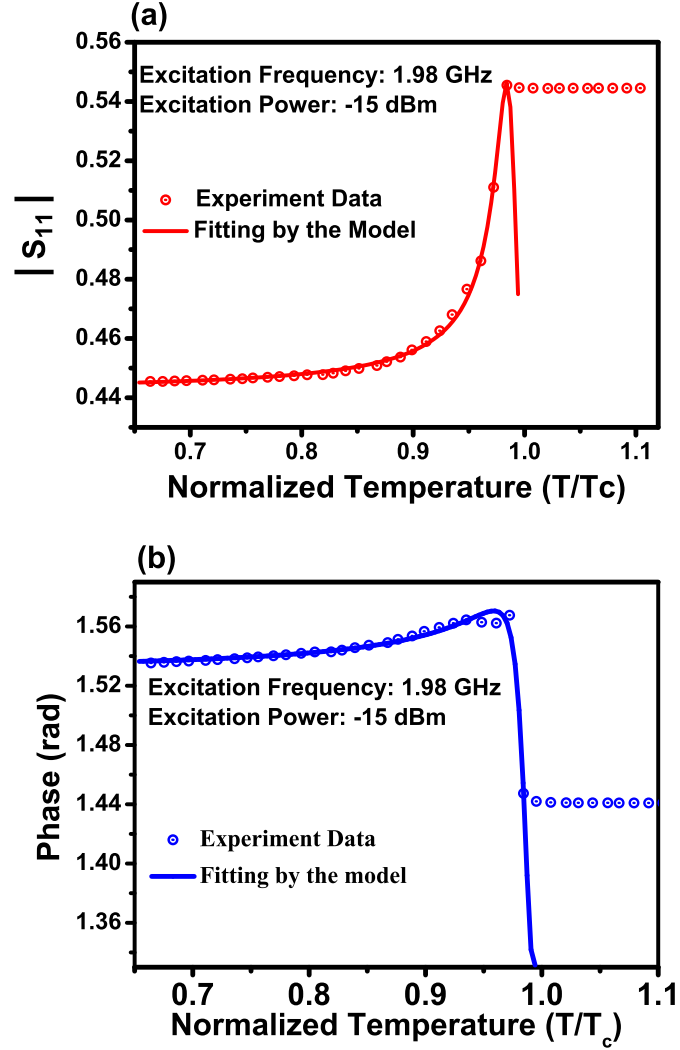
Fig. 4.7: (a) Theoretical amplitude of S_{11} based on the model is plotted by the solid line and experimental amplitude of S_{11} is plotted in dot circle symbols. (b) Theoretical phase of S_{11} based on the model is plotted by the solid line and experimental phase of S_{11} is plotted in dot circle symbols. Note that experiment data for both amplitude and phase is from Fig. 4.4 (a) measured with the PINNACLE probe at 1.98 GHz, -15 dBm excitation. Theoretical curve is plotted with αl=0.245 (unit-less), Z_1=30.23 Ω, R_{Bkd}=320.48 Ω, X_{Bkd}=-105.13 Ω, N/R_g=6.59 $* 10^{-9}$ $Henry$ and μ_0/μ_f= -0.46 under constant values nl=0.065 m and d_{yoke}=500 nm.

with an excitation frequency of 1.98 GHz from Fig. 4.4 (a). The solid lines in Fig. 4.7 (a) and Fig.4.7 (b) show the theoretical amplitude and phase respectively, based on the model with the following fit coefficients : $\alpha l = 0.245$ (unit-less), $Z_1 = 30.23\ \Omega$, $R_{Bkd} = 320.48\ \Omega$, $X_{Bkd} = -105.13\ \Omega$, $N/R_g = 6.59 * 10^{-9}\ Henry$ and $\mu_0/\mu_f = -0.46$. Note that the model is designed only to fit the data in the superconducting state. The experimental data for the amplitude and phase measured by the PINNACLE probe is also indicated in the figure by dot circles. Note that the μ_0/μ_f is a negative value, which implies that the excitation frequency is above and not far away from the yoke ferrite ferromagnetic resonance frequency. All of the fitting coefficients are physically reasonable.

The data set measured by the GT5 probe with an excitation frequency at 4.82 GHz is also fitted for comparison. Fig. 4.8 (a) and Fig.4.8 (b) show the fit results based on the model for amplitude and phase respectively with solid lines and experimental data as dot circles. The solid lines are plotted for the following fitting coefficients: $\alpha l = 0.353$ (unit-less), $Z_1 = 17.63\ \Omega$, $R_{Bkd} = 53.73\ \Omega$, $X_{Bkd} = 83.05\ \Omega$, $N/R_g = 3.46 * 10^{-11}\ Henry$ and $\mu_0/\mu_f = -0.43$.

Comparing both measurements done by two different probes and their individual fitting results, there are many similarities and differences. First, both fitting results for μ_0/μ_f are negative. This means that both probes function at frequencies above but near their yoke ferrite ferromagnetic resonance frequency. Also, R_{Bkd} and X_{Bkd} are extremely dependent on the excitation frequencies and probe details. This is expected because these parameters account for un-calibrated properties of the probes that depend sensitively on probe fabrication details and frequency. The
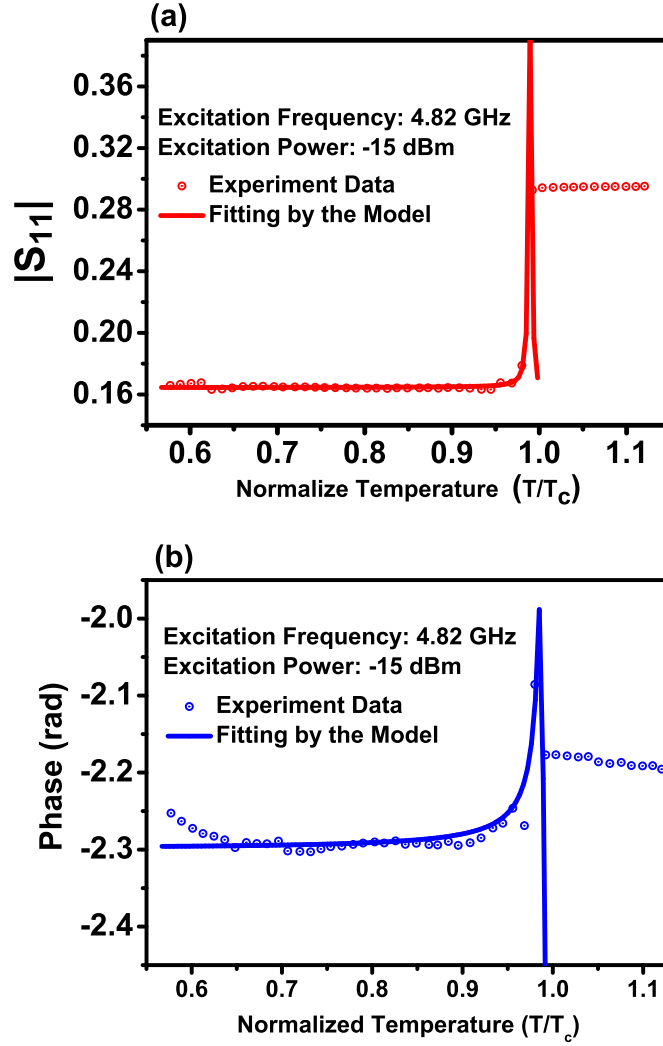
Fig. 4.8: (a) Theoretical amplitude of S_{11} based on the model is plotted by the solid line and experiment amplitude of S_{11} is plotted in dot circle symbols. (b) Theoretical phase of S_{11} based on the model is plotted in solid line and experimental phase of S_{11} is plotted in dot circle symbols. Note that experimental data for both amplitude and phase is from Fig. 4.4 (b) measured with the GT5 probe at 4.82 GHz, -15 dBm excitation. Theoretical curve is plotted with $\alpha l = 0.353$ (unit-less), $Z_1 = 17.63 \ \Omega$, $R_{Bkd} = 53.73 \ \Omega$, $X_{Bkd} = 83.05 \ \Omega$, $N/R_g = 3.46 * 10^{-11} \ Henry$ and $\mu_0/\mu_f = -0.43$ under constant values $nl = 0.065 \ m$ and $d_{yoke} = 500$ nm.

significant difference for N/R_g can be interpreted by the difference of the two probe geometries (One is a mono-pole shape and the other one is traditional ring shape). Another thing to mention is that a change of yoke thickness in the simulation will slightly change all of these six coefficients but not very significantly. This means that these fitting coefficients are not sensitive to the change of yoke thickness but will be very sensitive to the excitation frequency. This model enables a quantitative interpretation of the measurement data in the near-field magnetic microwave probe. Finally the model doesn't fit the data in the normal state. This is because in the normal state, the penetration depth $\lambda(T)$ in Eq.4.6 should change to the skin depth of the normal state Nb. In this case, the field configuration around the sample is very different, and the situation is of no interest to us here. Finally we note that this method can be used to extract the magnitude and temperature dependence of the magnetic penetration depth in the superconducting thin film, once the other parameters have been determined by measurements on standard samples.

4.4   The Limitation of the Linear Response Measurement

From the normal state to the superconducting state, the surface resistance suddenly drops to a value closer to zero, but not exactly zero. This value of surface resistance will be a function of the applied magnetic field in the superconducting state. Technically this dependence can be extracted from the microwave measurement of S_{11} by applying different RF magnetic fields up to a scale on the order of the thermodynamic critical field. The change of S_{11} under different RF magnetic

fields would help to calculate the surface resistance as a function of the RF field. This is of importance for the so-called medium-field and high-field Q slopes of SRF cavities. It is widely observed that the Q of SRF cavities falls with increasing surface RF magnetic field, particularly as the quench field is approached. A detailed understanding of these Q-slopes is lacking. Figure 4.9 shows a schematic picture of changes of surface resistance (R_s) and changes of third order harmonic response (P_{3f}) as a function of the applied field. Comparing R_s and P_{3f}, R_s changes only at high field but P_{3f} already responds at intermediate field values. The conclusion is that the nonlinear response measurement should be a more sensitive and easier way to image the surface microwave properties of the superconductor compared with the microwave linear response measurement. This conclusion has been verified by the Intermodulation Distortion (IMD) measurement and surface resistance measurement on an MgB_2 resonator as a function of the circulating power [78]. Roughly speaking, IMD measurements are equivalent to measuring the harmonic response. In our nonlinear measurement, we directly measure the P_{3f} to identify the microwave surface properties of the superconductors because P_{3f} measurement is a straightforward and useful method in the wide bandwidth near-field microwave microscope.

Another limitation of the low-power linear response measurement is the fact that we could not develop signals from bulk Nb surfaces. The reason is that the effective penetration depth in thin films with thickness $d_{film} \ll \lambda$ is more significant than that of bulk superconductors, as illustrated in Eq. 4.7, which leads to a measurable change in the linear response measurement on Nb thin film but not on
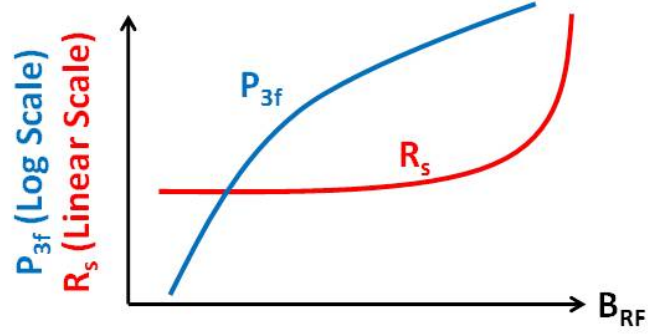
Fig. 4.9: Comparison of the change of surface resistance (R_s) and the change of third harmonic response (P_{3f}) under a magnetic field (B_{RF}) in a schematic picture. This figure is supported by third-order intermodulation measurements on MgB_2 [78].

bulk Nb. This limitation further motivates the need to pursue localized nonlinear measurements to get information about bulk Nb.

4.5   Chapter 4 Conclusions

From the linear response measurement of Nb thin films by the magnetic write head probes, the electrodynamic properties of Nb materials can be identified. The linear response can be used to find the film T_c in a local area. A magnetic circuit model combined with the transmission line circuit is given to interpret the linear response measurement. From the curve fitting results, many unknown coefficients in our microwave circuit can be generally approximated. This model will benefit the understanding in building a novel near field magnetic microwave microscope and then quantitatively imaging the microwave surface properties of SRF materials.

5. NONLINEAR RESPONSE MEASUREMENT RESULTS AND DISCUSSION OF CUPRATE, NB FILMS AND THE BULK NB SAMPLE

5.1 Nonlinearity Measurement and Setup

In the previous work of our group, we developed a large scale size of the magnetic loop probe with an inner diameter $\sim 200~\mu m$ & the outer diameter $\sim 2~mm$ to nondestructively measure the local harmonic generation from unpatterned superconducting samples [10], [11], [12]. In this design, the low resolution in imaging prevents the discovery of nanoscale defects and their associated microwave properties. Therefore, we replace the loop probe with the magnetic write heads shown in Table 3.1 to produce stronger and more localized RF magnetic fields, and to enhance the magnetic coupling between the probe and the superconducting sample. A comparison of the magnetic loop probe and a representative magnetic write head probe is shown in Fig. 5.1.

The nonlinear amplitude and phase measurements of the superconductor harmonic response utilizes the two-port VNA method shown in Fig. 5.2. Both the
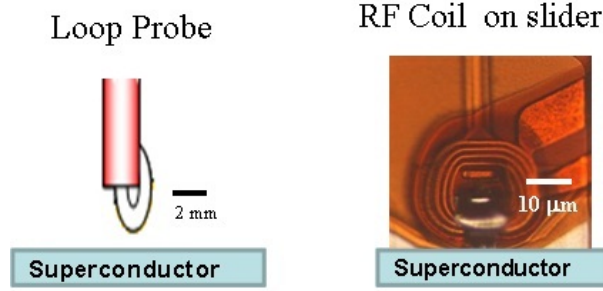
Fig. 5.1: Comparison of loop probe (left) and magnetic write head probe (right). A 4-turn coil is visible inside this magnetic write head, which develops a high frequency magnetic field in a write-gap near the surface of the superconductor.

magnetic probe and the superconductor are kept in a high vacuum cryogenic environment. An excited wave (fundamental signal) at frequency f comes from port 1 of the VNA and is low-pass filtered to eliminate higher harmonics of the source signal. This fundamental tone is sent to the magnetic write head probe to generate a localized RF magnetic field on the superconductor sample. The superconducting sample responds by creating screening currents to maintain the Meissner state in the material. These currents inevitably produce a time-dependent variation in the local value of the superfluid density, and this in turn will generate a response at harmonics of the driving tone. The generated harmonic signals are gathered by the magnetic probe and returned to room temperature where they are high-pass filtered to remove the fundamental tone V_f. Finally, an un-ratioed measurement of V_{3f} is performed on port 2 of the VNA.

In this way, we measure the complex third harmonic voltage of $V_{3f}^{sample}(T)$ or equivalent scalar power, $P_{3f}^{sample}(T)$. With the assumption of $d_{film} \ll \lambda$, this
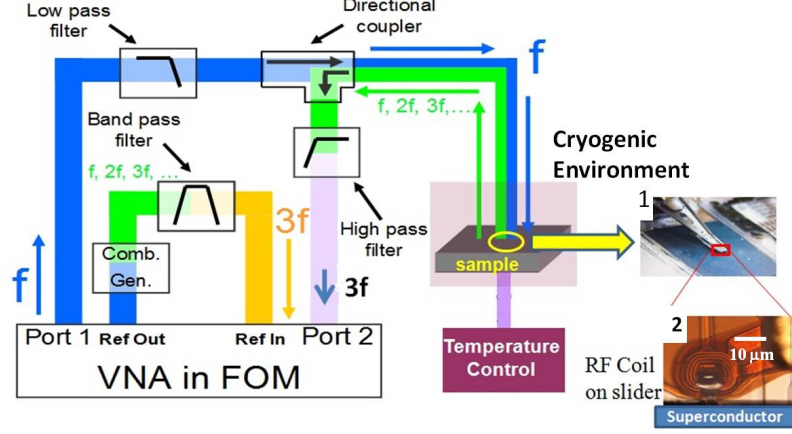
Fig. 5.2: Set up of phase-sensitive harmonic measurement in nonlinear microwave microscopy. The frequency offset mode (FOM) of a vector network analyzer (VNA :model PNA-X N5242A) is used in this measurement. Inset 1. shows the magnetic write head probe assembly on top of a superconducting thin film and inset 2. is a picture of the RF micro-coil of the probe above the sample.

generated third harmonic power $P_{3f}^{sample}(T)$ is estimated as [53] [84]

$$P_{3f}^{sample}(T) = \frac{\omega^2 \mu_0^2 \lambda^4(T) \Gamma^2(K_{RF})}{32 Z_0 d_{film}^6 J_{NL}^4(T)} \qquad with \qquad \Gamma(K_{RF}) = I_{tot} \int \frac{\int K_{RF}^4(x,y)dx}{(\int K_y dx)^2} dy \tag{5.1}$$

where ω is the angular frequency of the incident wave, $\lambda(T)$ is the temperature dependent magnetic penetration depth, Z_0 is the characteristic impedance of the transmission line in the microscope, μ_0 is the permeability of free space, d_{film} is the thickness of the tested superconductors, I_{tot} is the total current flowing through a crossection right beneath the bottom of the probe, $K(x,y)$ is the surface current induced in the superconductor at the fundamental frequency, J_{NL} and Γ are the de-pairing critical current density of the superconductor and a current-distribution geometry factor, respectively. The value of $\Gamma(K_{RF})$ depends on the distribution of

surface current density, $K_{RF}(x, y)$ on the superconducting plane. From Eq. (5.1), a strong magnetic field from the magnetic write head probe (as compared to the loop probe) will enhance the surface current K_{RF} and confine the current distribution, both leading to an enhancement of Γ, and therefore P_{3f}, for a given excitation power. This has the added benefit of improving the spatial resolution of the probe. The value of J_{NL} also significant affects the P_{3f}. For intrinsic nonlinearity, J_{NL} can be roughly estimated by a theoretical model for the superconductor response as a function of the superfluid density and the energy gap of the superconductors. For s-wave superconductors (for example, Nb), the intrinsic P_{3f} is very small and below the noise level of the analyzer at any superconducting temperature, except around T_c. For extrinsic nonlinearity, J_{NL} will depend on the specific defect and results in a measurable P_{3f} above the noise level of the analyzer. Fig. 5.3 schematically shows the different values of J_{NL} on different defects. One can clearly see that defective regions of the sample, including those responsible for hot-spot generation in the SRF cavities, have smaller values of J_{NL} than the surrounding material, hence will develop larger P_{3f}, thus giving away their location to the microscope.

In order to get a phase-sensitive measurement of the 3rd harmonic signal coming from the superconducting sample, a harmonic generation circuit (comb generator) is connected to provide a reference 3rd harmonic signal, and the relative phase difference between the main circuit and reference circuit is measured. Further detail about this phase-sensitive measurement technique can be found in the work of D. Mircea, Ref. [65]. In this way we measure the complex third harmonic voltage $V_{3f}^{sample}(T)$ or the corresponding scalar power $P_{3f}^{sample}(T)$. The lowest noise floor
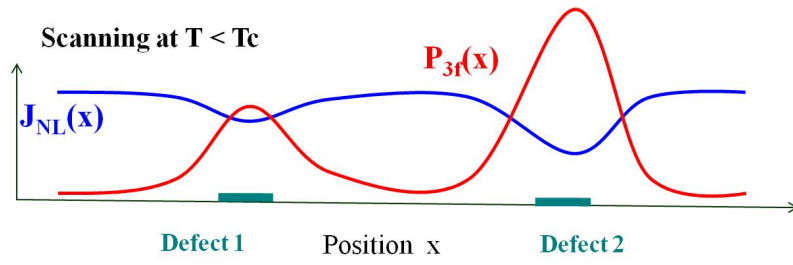
Fig. 5.3: Schematic J_{NL} variation on the superconducting surface with different defects. The P_{3f} generation from defects is local. Hence measuring P_{3f} at different positions can be used to find defects on superconductors.
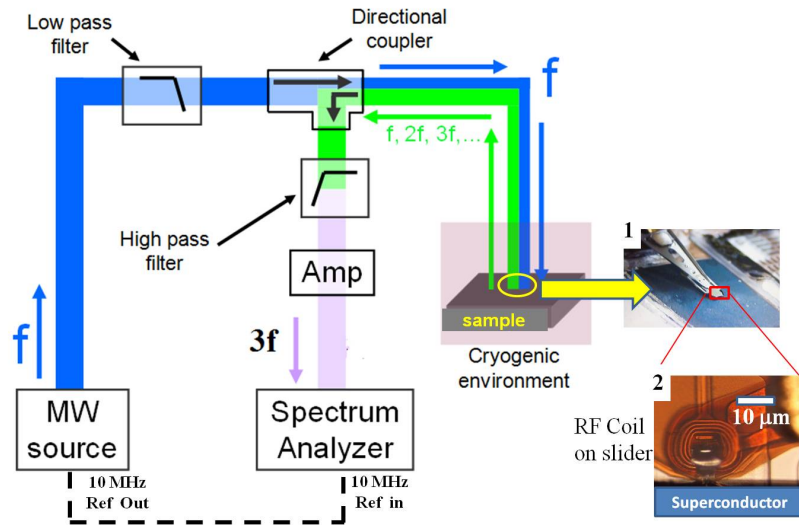
Fig. 5.4: Set up of P_{3f} measurement in nonlinear microwave microscopy. A preamplifier (Agilent model ♯ 87405C) is used in front of the input terminal of the spectrum analyzer (Agilent model ♯: ESA-E E4407B) to enhance the sensitivity to small signals. A phase-lock loop is connected between the microwave source (HP model ♯ 83620B) and the spectrum analyzer to match the phase of the microwave source and the spectrum analyzer. Inset 1. shows the magnetic write head probe assembly on top of a superconducting thin film and inset 2. is a picture of the RF micro-coil of the probe above the sample.

of the VNA (Model $\sharp$: PNA-X N5242A) in our measuring frequency range is -127 dBm for the un-ratioed power measurement. A ratioed measurement of the complex $V_{3f}^{sample}(T)/V_{3f}^{ref}$ is also performed at the same time. The microscope thus measures the local harmonic power and phase generated at the location of the probe, for a given incident frequency, power and sample temperature.

A method to lower the noise floor is to remove the VNA and use a stable synthesizer (model $\sharp$ HP 83620B) on port 1 and a spectrum analyzer (model $\sharp$: ESA-E E4407B) on port 2 (see Fig. 5.2). The noise floor of our spectrum analyzer is -147 dBm, better than our VNA. A preamplifier (Agilent $\sharp$ 87405C) may be placed before the input terminal of the spectrum analyzer to enhance the signal to noise ratio (SNR). In this way, the noise floor of the spectrum analyzer is reduced to -165 dBm to further enhance the sensitivity to any small signals in our P_{3f} measurement. Fig. 5.4 shows this alternative microwave circuit for sensing small P_{3f} signals from the superconductor. The phase-lock connection is applied between the microwave synthesizer (microwave source) and the spectrum analyzer. In this phase-lock loop, a 10 MHz reference signal from the microwave source is generated and output as the 10 MHz reference signal for the spectrum analyzer. To perform the data acquisition on the spectrum analyzer, a 100 Hz span centered at the desired third harmonic frequency (3f) is used. There are 100 points in the 100 Hz span and my program will automatically search for the maximum signal in the 100 Hz span after 10 averages of the signal. The reason I use 100 discrete points in a 100 Hz span and 10 averages is a compromise between the data acquisition time and the need for a better signal to noise ratio. Using these parameters, we can estimate an error of 3 dB for the

P_{3f} measurement. Details of how I find the best desired third harmonic frequency power (P_{3f}) on a sample can be found in Appendix A.2.

5.2   Temperature Dependent Third Harmonic Measurement on High-T_c Superconductor Measured by "Quantum Big Foot" Probe

5.2.1   Measurement Results on High-T_c Cuprate

A measurement of the temperature dependent 3rd order harmonic power is performed at the center of a $Tl_2Ba_2CaCu_2O_8$ (TBCCO) film by the "Quantum Big Foot" magnetic write head probe with different exciting powers. The superconducting sample we study first is a TBCCO thin film of thickness 500 nm, epitaxially grown by the magnetron sputtering method [79]. The T_c of the TBCCO film is 103.2 K determined by an AC susceptibility measurement. The reason we study the cuprate superconductor is to understand the characteristics of the magnetic write head probe on superconductors and to save the consumption of liquid helium before measuring the Nb materials. The inset of Fig. 5.5 shows $P_{3f}(T)$ measured by the low resolution loop probe. A peak in P_{3f} near T_c shows up. This enhancement of P_{3f} arises from the modulation of the superconducting order parameter near T_c due to the enhanced sensitivity of superconducting properties as the superfluid density decreases to near-zero levels. This peak at T_c is phenomenologically predicted by Ginzburg-Landau theory and is particularly pronounced for thin film samples. From Eq. (5.1), one sees that due to J_{NL} approaching zero and $\lambda(T)$ diverging at T_c, the

third harmonic power will increase strongly. The divergence is cut off by the distribution of transition temperatures in the sample, and the influence of quasiparticle electrodynamics. With the loop probe, the enhancement of P_{3f} above background is only 15 dB, for 18 dBm fundamental input power. Such a small enhancement can be easily achieved on the same sample by the magnetic head probe with only 9 dBm excited power (Fig. 5.5), which means that the magnetic write head generates a more localized and intense field, inducing stronger surface currents on the sample. From comparison of the 18 dBm data in Fig. 5.5, we find that the probe geometry factor Γ [12] is enhanced by a factor of 30 in the "Quantum Big Foot " magnetic write head probe compared to the loop probe. Note that localized heating would produce a shift of the $P_{3f}(T)$ peak to lower temperature with increasing input power. Despite these higher currents, there is no evidence of localized heating in the sample from the magnetic write head probe.

Another point to note is that the apparent noise floor of the measured P_{3f} increases with an increased excitation power. This increased P_{3f} in the noise floor is from the magnetic write head probe itself. We have measured the P_{3f} of the magnetic probe on the surface of a bare sapphire substrate and in general this probe nonlinearity is negligible at excited powers under 10 dBm at this excitation frequency. However, at high excited power the magnetic write head probe shows a measurable nonlinearity. Hence, higher excited power not only excites the higher nonlinearity of the tested superconductors but also the nonlinearity of the magnetic write head probe. The mechanism of probe nonlinearity is the hysteretic behavior of the yoke material [80] and has been discussed in the literature [66]. Although higher
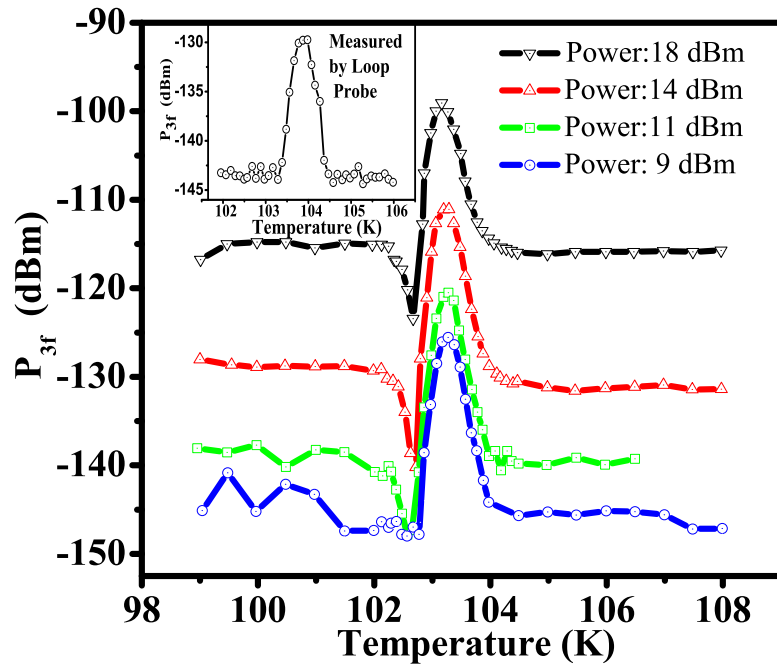
Fig. 5.5: Temperature dependence of third harmonic power P$_{3f}$ of a TBCCO film, measured by a magnetic write head probe (Quantum Big Foot Probe) with an excitation frequency of 3.5 GHz. Data shown in the inset is measured by the bare loop probe with excitation frequency of 3.5 GHz and excited power 18 dBm.
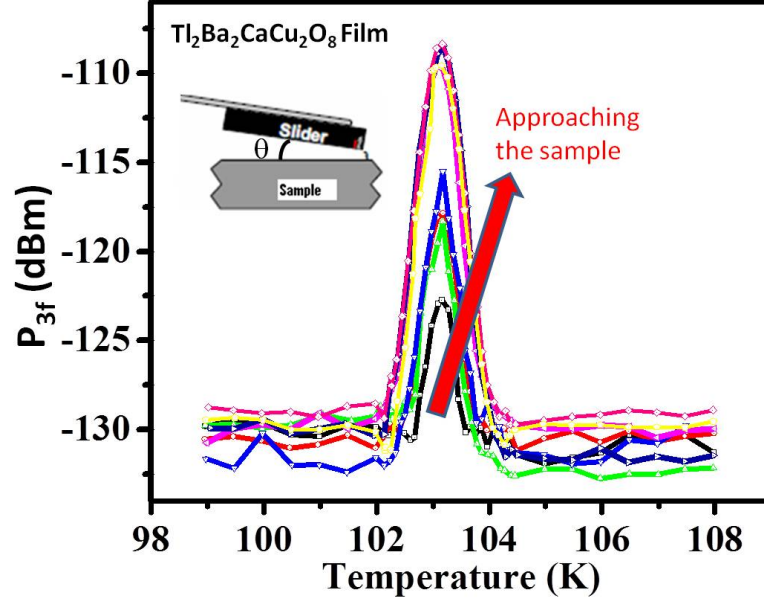
Fig. 5.6: Height dependence of the P_{3f} on TBCCO sample. The closer the probe to the sample, the stronger the P_{3f} from the TBCCO superconductor. The excitation frequency and power are 3.76 GHz, 12 dBm respectively in the measurement. The arrow in the figure indicates the probe moving direction toward the sample surface.

excited power excites stronger nonlinearity from the probe, this probe nonlinearity is almost temperature independent in a very wide cooling temperature range, especially at Helium cooling temperature. This is good for us to study the localized microwave properties for Nb materials. It should also be noted that the probe nonlinearity (V_{3f}^{probe}) is complex. When added to the signal from the superconductor V_{3f}^{sc}, the total nonlinearity can increase, or decrease, the magnitude of the measured third harmonic power (P_{3f}) as shown near T_c in Fig. 5.5. Therefore we treat probe nonlinearity as a constant background complex signal above the noise floor of the spectrum analyzer.

In addition, the P_{3f} from the superconductor is very sensitive to the probe height, as shown in Fig. 5.6. In this measurement, the probe height can be controlled by adjusting the landing angle of the slider, θ, through a micrometer on the z-axis of the probe station (see Fig. 4.2 and Fig. 8.1). The excitation frequency and power are maintained constant (3.76 GHz, 12 dBm) during the measurement and only the position of the micrometer on the Z-axis of the probe station is varied. As shown in Fig. 5.6, as the probe approaches the sample surface, an enhanced screening current on the superconductor will generate stronger P_{3f}. Again there is no temperature shift of the nonlinear response, suggesting that local heating is not an issue in these measurements. Therefore, in our experiment, we want our probe as close as possible to the sample to enhance the maximum nonlinearity from the tested superconductors. The probe height can first be roughly decided through the image of the built-in optical microscope on the cryogenic probe station, followed up by a frequency dependent linear response $S_{11}(f)$ measurement as discussed in Chapter 4 (Fig. 4.3) to look for the best height position and excitation frequency.

5.2.2 Measurement Results on High Quality MgB_2 Films

A high quality epitaxial MgB_2 thin film with thickness 25 nm is also examined to test the magnetic write head probe in a liquid Helium cooled environment. The MgB_2 film is deposited on a SiC substrate by a hybrid physical-chemical vapor deposition technique [81]. Temperature dependent 3rd order harmonic power is also measured in the center position of an MgB_2 thin film. In Fig. 5.7, a peak at 39.1 K shows up clearly near the known T_c of the film. This proves that the magnetic
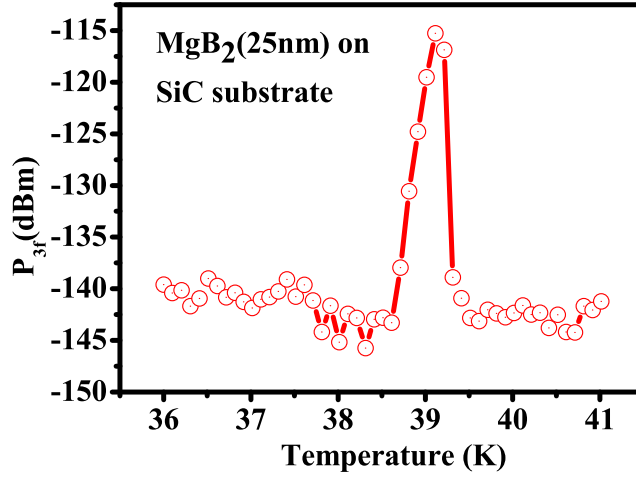
Fig. 5.7: Temperature dependence of third harmonic power P_{3f} from an MgB_2 film, measured with the magnetic write head probe (Quantum Big Foot Probe) with an excitation frequency of approximately 3.5 GHz and a power of 12 dBm.

probe can function in the low temperature region. Comparison of this peak with that of TBCCO, one finds a much sharper transition, implying a narrow distribution of T_c values in the MgB_2 thin film. The MgB_2 nonlinear measurement results will be discussed in much more detail in Chapter 7.

5.3   Temperature Dependent Third Harmonic Measurement on Superconductors by the GT5 Probe

5.3.1   Temperature Dependent Third Harmonic Measurement on the Cuprate Thin Film

From the previous section, the P_{3f} measurement by the "Quantum Big Foot" probe often just shows a peak in $P_{3f}(T)$ near T_c. No matter how strong the excitation
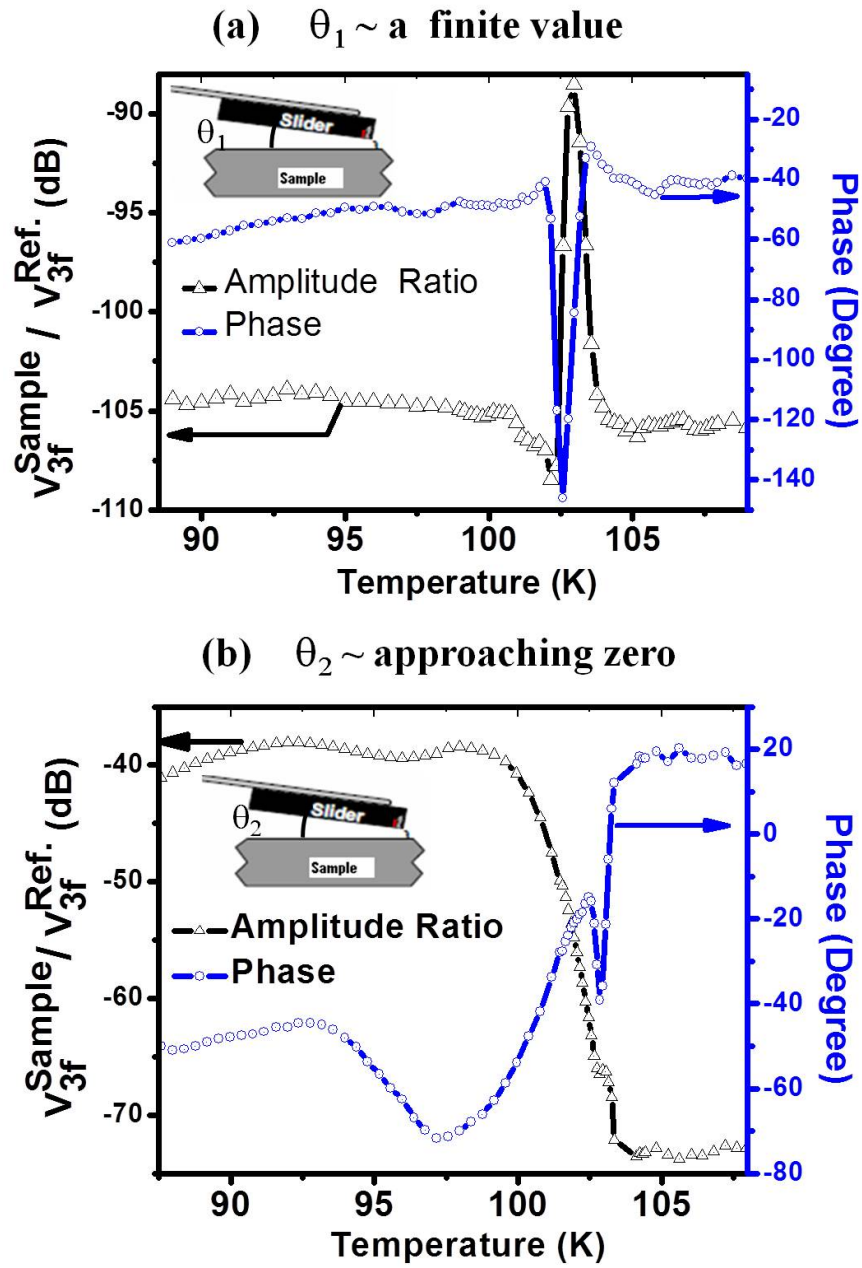
Fig. 5.8: The complex third harmonic response of $V_{3f}^{Sample}(T)/V_{3f}^{Reference}$ of a TBCCO thin film superconductor measured by the GT5 probe. The magnitude (black line) and its phase (blue line) are illustrated individually. The magnetic write head probe touches the sample with different landing angles during the measurement. (a) Landing angle (θ_1) is a finite value (b) Landing angle (θ_2) is much smaller compared to θ_1.

69

power is or how close the probe-sample distance is, the nonlinear signal below T_c is not seen. This may imply that the field coming from the "Quantum Big Foot" probe is still not enough to excite the superconductor into an Abrikosov vortex state or some other nonlinear state at low temperature. Therefore, again, a measurement of the temperature dependent 3rd order harmonic power is performed at the center of the TBCCO film but by the newer-generation GT5 magnetic write head probe. Figure 5.8 (a) shows the temperature dependent $P_{3f}(T)$ result measured by the GT5 write head probe. A peak in P_{3f} near T_c shows up, as expected. In addition, also as expected, the phase of $V_{3f}(T)$ goes through a minimum while its amplitude shows a maximum as temperature is increased from below T_c, as noted before by Dragos Mircea of our group [65]. The new and interesting result is the $P_{3f}(T)$ excited by this localized strong RF magnetic probe below T_c as shown in Fig. 5.8 (b). This nonlinearity can be easily excited by approaching the probe as close as possible to the sample surface, which implies the magnetic field on the surface is enhanced to a value larger than the lower critical field (H_{c1}) but smaller than the upper critical field (H_{c2}) of the TBCCO. In this case, the phase shows a local minimum at T_c and then is followed by a turning point at 102.5 K, which implies a change in the dominant nonlinear mechanism from the intrinsic nonlinearity coming from the modulation of superconducting order parameter near T_c to the nonlinearity perhaps in the Abrikosov vortex critical state. In my experiment, the applied RF field on the sample depends on the angle θ between the probe assembly (slider) and the sample surface. Ideally, the smaller θ, the smaller the distance between the probe and the sample, which means a more intense magnetic field on the tested superconductors.

70

This GT5 magnetic write head probe satisfies our need to excite the superconductors into a nonlinear state. We use this GT5 probe for the rest of the P_{3f} measurement on the Nb thin films and the bulk Nb sample. This nonlinear response from low temperatures will be very sensitive to the surface defects, for example due to defects which generate additional channels of dissipation and reactance.

5.3.2 Temperature Dependent Third Harmonic Measurement on the Nb Thin Film

The sputtered Nb film with thickness 50 nm is examined in a 3rd harmonic measurement. These samples have been described in Chapter 4. In this experiment, the temperature of the sample could be generally cooled down to almost 5 K by carefully anchoring the samples on the cold plate of our cryostat. We probe many single points on the Nb sample surface. To address each point, the magnetic writer probe has to lift, laterally translate to another position, and then probe the new position. The height of the probe is judged by optical microscopy and an attempt is made to keep the same height of the probe in each measurement. We see significant differences at different points for this third harmonic nonlinear measurement.

A representative result at one point is shown as the dots in Fig. 5.9 under 14 dBm, 3.41 GHz excitation. A peak in $P_{3f}(T)$ near 8.3 K indicates the T_c of this material and can be interpreted as the intrinsic nonlinearity from the modulation of the superconducting order parameter near T_c due to the decrease of superfluid density and the associated divergence of the penetration depth near T_c [53] [65]. Note that a low temperature nonlinearity follows up after the peak and gradually grows

71

while decreasing temperature. This low temperature nonlinearity may come from the Abrikosov or Josephson vortex critical state, and implies a nonlinear mechanism related to moving flux or vortices inside the film [11] [12]. In other words, when the field from the writer is higher than the lower critical field (H_{c1}) of the Nb, magnetic flux will penetrate into the superconductor and produce a nonlinear response [82]. This mechanism can be interpreted as at least one vortex (or one vortex/antivortex pair) overcoming the Bean-Livingston barrier [83] and penetrating into the film. In this case, it is not clear how many vortices are involved or the manner of vortex entry and exit; either in the form of a semiloop [57] or perpendicular vortex/anti-vortex pair [48]. However, considering the gap geometry of the magnetic writer probe and the known film thickness, which is comparable to the value of its magnetic penetration depth at zero temperature, a harmonic response from a perpendicular vortex-antivortex pair may be the mechanism of this additional nonlinearity [48]. This will be discussed in more detail later in section 7.4.4.

The solid line in Fig. 5.9 shows the result of the theory for $P_{3f}(T)$ based on the mechanism of the intrinsic nonlinearity near T_c using the Ginzburg-Landau (GL) model [53]. The generated third harmonic power P_{3f} can be estimated with Eq. (5.1) derived for the time dependent nonlinear inductive circuit [53] [84]. Next we discuss this model in detail.
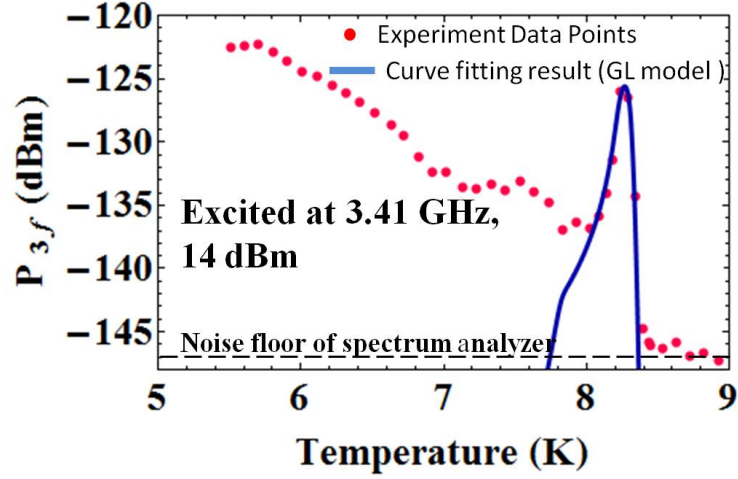
Fig. 5.9: Temperature dependence of the third harmonic response for a 50 nm thick Nb film. In this measurement, a microwave synthesizer and a spectrum analyzer are used for the nonlinear measurement. The noise floor of the spectrum analyzer in the $P_{3f}(T)$ measurement is -147 dBm. The dot points are experimental P_{3f} data measured by the GT5 probe. A calculated result (solid curve) based on the GL model is fit to the data near T_c. The parameters are as follows: $\Gamma = 10^5$ A^3/m^2, $\lambda(0K) = 40$ nm, $\lambda_{cutoff} = 312$ nm, $J_{cutoff} = 2.1 * 10^{11}$ A/m^2, and $T_c = 8.3$ K with a standard deviation of Gaussian spread of $\delta T_c = 0.03$ K.
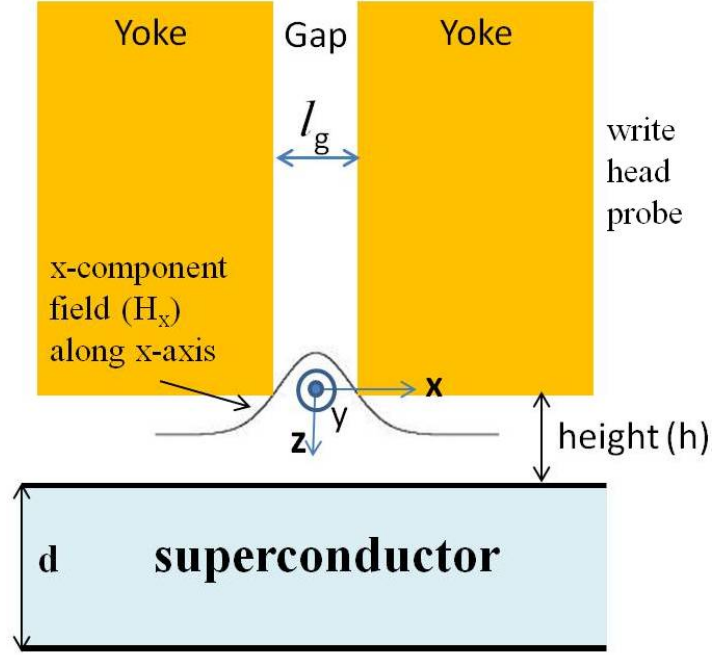
Fig. 5.10: Schematic illustration of the 2D magnetic write head on the top of the super-conductor. The origin is at the bottom of the head centered at the middle of the gap. Gap length (l_g) and film thickness (d) are not to scale.

5.3.3 Model of Intrinsic Nonlinear Response Near T_c of the Nb Thin Film

Based on our magnetic write head probe, we calculate the surface current from the Karlqvist equation [85], which gives the magnetic field distribution outside the gap of the magnetic writer in the x-z plane as schematically shown in Fig. 5.10. Under the treatment of the Karlqvist 2D assumption, the fields are invariant in the y-direction along the gap. By only considering the x-component of magnetic field (H_x) on the superconducting surface, which is doubled with respect to free space by the boundary condition of the surface, the surface current K_y can be written as

$$K_y = \frac{2B_g}{\mu_0} \arctan\left[\frac{l_g z}{x^2 + z^2 - (l_g/2)^2}\right] \tag{5.2}$$

where B_g is the maximum field strength inside the gap, l_g is the length of the gap and x, z are distances in the x and z directions with the origin centered in the middle on the bottom of the gap. In reality, the gap is of finite thickness in the y direction as shown in the schematic yoke picture of Fig. 4.5 (a) with thickness l_y. By assuming that the currents are uniform in the y-direction between $y = 0$ and $y = l_y$ and ignoring the return currents, the current distribution geometry factor Γ in Eq. 5.1 can be approximated as

$$\Gamma \cong \frac{l_y \int_{-\ell}^{\ell} K_y^4 dx}{I_{tot}}; \qquad I_{tot} = \int_{-\ell}^{\ell} K_y dx \qquad (5.3)$$

where ℓ is the distance from the center of maximum current to the node of minimum current as shown in the inset of Fig. 5.11 which is simulated by the ANSYS High Frequency Structure Simulator (HFSS) under the assumption that the magnetic writer is 2 μm away from a perfect conductor surface. However, in the Karlqvist model, the ℓ is effectively infinite since no return current is considered due to Karlqvist assumption for invariant field in the y-direction. The height dependence of Γ can be calculated as shown in Fig. 5.11 when evaluating the K_y function at variant $z = h$ in Eq. 5.2. In our calculation, we assume $B_g = 1\ Tesla$, $l_g = 100\ nm$. Therefore the value of the Γ can be estimated to be $10^5 A^3/m^2$ under the assumption that the probe height is around 4 μm above the superconducting surface while fitting the measured $P_{3f}(T)$ peak in Fig. 5.9. We note that the probe geometry factor is a strong function of height and can lead to surface fields above the critical field of the superconductor [53].
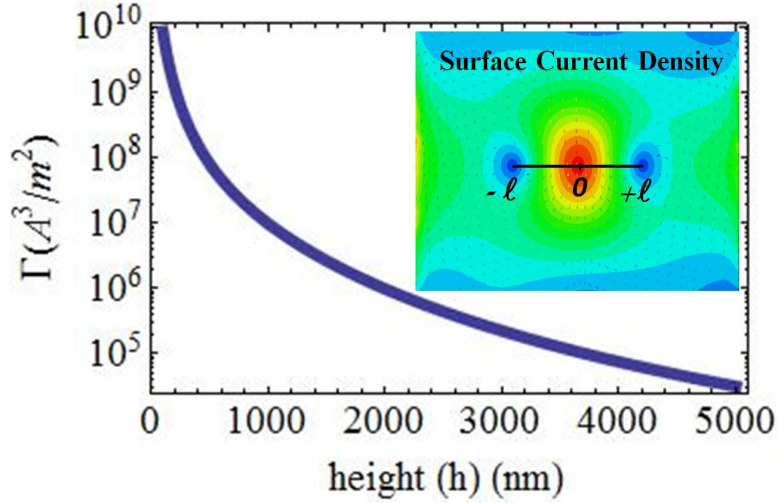
Fig. 5.11: Calculation of height dependence (h is the +Z direction) of the probe geometry factor $\Gamma(K_{RF})$ for the longitudinal magnetic write head probe under the assumption of Karlqvist model. The black line in the inset shows the integral path of Eq. (5.3) on the plot of the surface current density simulated by the ANSYS High Frequency Structure Simulator (HFSS) under the assumption that the magnetic writer is 2 μm away from a perfect conductor surface. Red corresponds to large current while blue corresponds to small current. The value of ℓ is on the scale of the outside edge dimension of the magnetic yoke, which is 1.5 μm in the HFSS simulation, and is effectively infinite in the Karlqvist calculation since the return currents are not considered.

The term J_{NL} in Eq. 5.1 is the nonlinear current density scale and quantitatively characterizes the mechanism of nonlinearity. For the intrinsic nonlinearity, this term is on the scale of the de-pairing current density of the superconductor. Based on the GL model, the temperature dependent $J_{NL}(T)$ can be written as

$$J_{NL} = J_0[1 - (\frac{T}{T_c})^2][1 - (\frac{T}{T_c})^4]^{1/2} \tag{5.4}$$

where T_c is the critical temperature, J_0 is the critical current density at 0 K, which can be estimated as H_0/λ_0 where H_0 and λ_0 are the thermodynamic critical field and penetration depth of Nb at 0 K, respectively. In our calculation, H_0 is assumed to be 200 mT and λ_0 is 40 nm. As T approaches T_c, the cutoff of $\lambda(T)$ and $J_{NL}(T)$ and a Gaussian distribution of T_c in Eq. (5.1) are also applied in this calculation. Finally from our result of the curve fitting as shown in the solid curve of Fig. 5.9, this model describes well the experimental results near T_c and proves that the measured $P_{3f}(T)$ peak comes from the mechanism of intrinsic nonlinearity. The fit parameters shown in the caption of Fig. 5.9 are all physically reasonable. It is clear that for the low temperature ($T < T_c$) nonlinearity, other mechanisms must be responsible for $P_{3f}(T)$.

The thickness dependence of the intrinsic nonlinear response near T_c is also a very important parameter for measuring this intrinsic nonlinearity of Nb thin films. As the thickness of the film becomes larger, the intrinsic nonlinearity due to modulation of the superconducting ordered parameter will become small and may be un-measurable (i.e. it may go below our noise floor). Fig. 5.12 shows

77
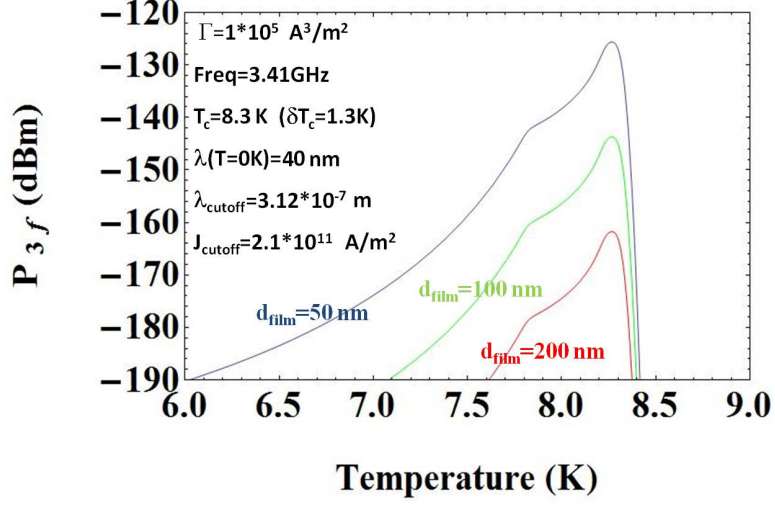
Fig. 5.12: Theoretical Nb thin film $P_{3f}(T)$ based on the model of intrinsical nonlinearity for three different thickness (50 nm, 100 nm and 200 nm). The curve with 50 nm thickness is the same as the theoretical fit curve on Fig. 5.9. Except the different thickness parameters, all three curves uses the same parameters are as follows: $\Gamma=10^5 \; A^3/m^2$, $\lambda(0K)=40$ nm, $\lambda_{cutoff}=312$ nm, $J_{cutoff}=2.1 * 10^{11}$ A/m^2, and $T_c=8.3$ K with a standard deviation of Gaussian spread of $\delta T_c=0.03$ K. A typical best noise floor for our measurements is above -160 dBm.

the theoretical temperature dependent $P_{3f}(T)$ based on the model of the intrinsic nonlinearity near T_c for three different thickness of Nb thin films. One can see the peak at T_c dramatically decreases as the film thickness increases. This implies that for measurement of thicker films and bulk materials, the P_{3f} peak at T_c will not show up once the P_{3f} peak at T_c is below the analyzer noise floor.

5.3.4   Complex Third Harmonic Voltage on the Nb Thin Film

In order to further understand the complex-valued third harmonic voltage V_{3f}, the phase-sensitive harmonic technique is performed on the 50 nm thick Nb film. In this measurement, the unratioed measurement shows a corresponding scalar power $P_{3f}^{sample}(T)$, which is analogous to the $P_{3f}(T)$ measurement done by the spectrum analyzer. Fig. 5.13 shows a representative data set for this measurement. Note

78

that the probe position in this measurement is different from that of Fig. 5.9. The red curve is the phase of the complex $V_{3f}^{sample}(T)/V_{3f}^{ref}$. The blue curve is the corresponding scalar power $P_{3f}^{sample}(T)$. Clearly, the phase shows a minimum at $T_c(\sim 8.3K)$ while the harmonic magnitude $P_{3f}(T)$ exhibits a maximum. Note that between the normal state and the superconducting state of Nb, the phase shift is almost $\pi/2$, consistent with an analytical model for the harmonic phase variation near T_c [65]. After this minimum, the phase is followed by a dramatic turning point at 8.0 K, which implies a change in the dominant nonlinear mechanism from the intrinsic nonlinearity near T_c to the nonlinearity in, for example, the vortex critical state. For temperatures below 8 K, the phase gradually decreases with decreasing temperatures while the amplitude of the $P_{3f}(T)$ slightly increases.

Comparing to the $P_{3f}(T)$ of Fig. 5.9, there are many similarities and differences. From the $P_{3f}(T)$ above T_c in Fig. 5.13, it is clear that the probe shows some nonlinearity at high excitation power. This nearly temperature independent probe nonlinearity is due to the hysteretic properties of the high permeability material in the yoke [66] and will become significant at high excited power. Therefore at $T > T_c$, all of the nonlinearity comes from the probe itself. Both $P_{3f}(T)$ in Fig. 5.9 and Fig. 5.13 show a peak at 8.3 K indicating the T_c of the Nb thin film. Below the peak, both of the temperature dependence of $P_{3f}(T)$ are consistent with that of Josephson vortices [11] [12]. However, this $P_{3f}(T)$ behaves a little bit differently. We see different levels of $P_{3f}(T)$ increase with decreasing temperatures at different locations. This may imply that the nonlinearity from the moving vortices is very sensitive to surface morphology and probe-sample separation. For further detailed analysis, a

79
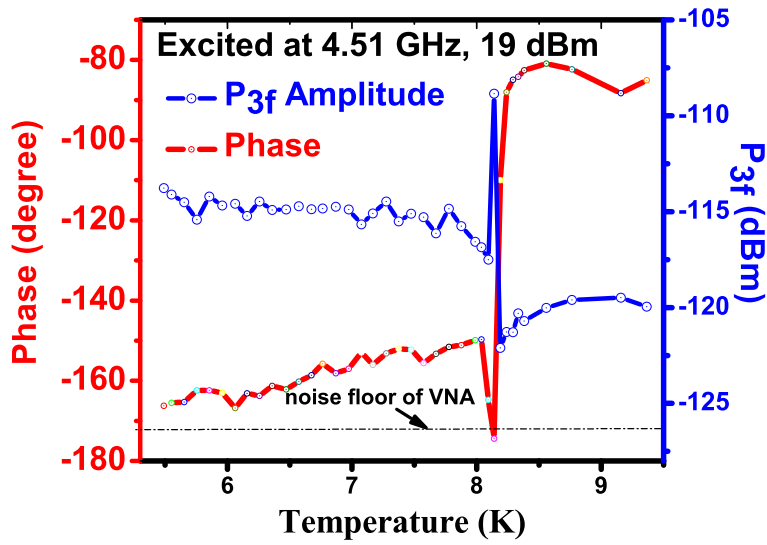
Fig. 5.13: Temperature dependence of the third harmonic response with amplitude (blue) and its relative phase (red) for a 50 nm thick Nb film. The two-port VNA measurement is used. The noise floor of the VNA in the $P_{3f}(T)$ measurement is -127 dBm. Note that the temperature scale was corrected because of poor thermal contact of the thermometer to the cold head. The GT5 probe is used in this measurement.

raster scan of the probe should be performed to realize the relation between surface morphology and vortex motion in the vortex critical state (see Chapter 8).

5.4 Nonlinearity Measurement on the Bulk Nb superconductor for the investigation of SRF cavities

5.4.1 Setup of Bulk Nb Measurement

From previous sections, we have succeeded in measuring the nonlinearity on the Nb thin film at low temperature, which implies the field generated by the magnetic write head probe is higher than the H_{c1} of thin film Nb. The final goal is the electromagnetic imaging of many types of defects on bulk Nb coming from the EP or BCP process steps in the fabrication of Nb cavities. Therefore cooling the bulk Nb down to its T_c and measuring the surface nonlinearity is very crucial in this research. A bulk Nb sample coming from a Nb cavity with a well-defined location of defects is the best candidate for measurement of the nonlinearity by our microwave microscope. Therefore, in this part, we collaborate with Prof. Tom Bieler, Dr. Compton and Dr. Baars at Michigan State University (MSU). Fig. 5.14 (a) shows a schematic picture of the original MSU tensile specimen made from bulk Nb with high residual-resistivity ratio (RRR). The surface of this tensile specimen received mechanical and EP treatment prior to deformation. Then a tensile experiment was conducted to deform and break the specimen into two halves . After the tensile test, the two halves are welded together. This welding structure is similar to the welded part between two hemi-spherical cavities in a SRF cavity. Fig. 5.14 (b) shows the

MSU Bulk Nb Sample
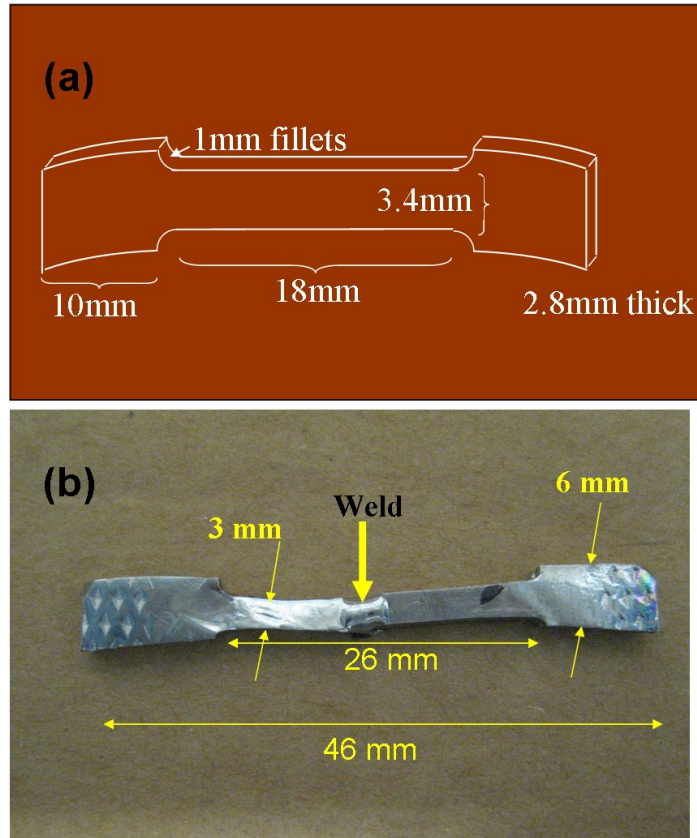
Fig. 5.14: (a)A schematic picture of the bulk Nb tensile specimen before deformation. All dimensions in the specimen are labeled. (b) The finished specimen after tensile test and welding treatment in the center of this sample.

finished specimen. The sample has been very carefully imaged by electron backscattered pattern (EBSP) orientation imaging microscopy (OIM) [86], by Prof. Bieler's group and can locate some specific defects which also appear in the processing of bulk Nb cavities.

In order to make the surface superconducting in our cryostat system for this bulk Nb sample, thermally anchoring the sample and good radiation shielding from the outside environment is crucial. Figure 5.15 shows the setup inside the cryostat
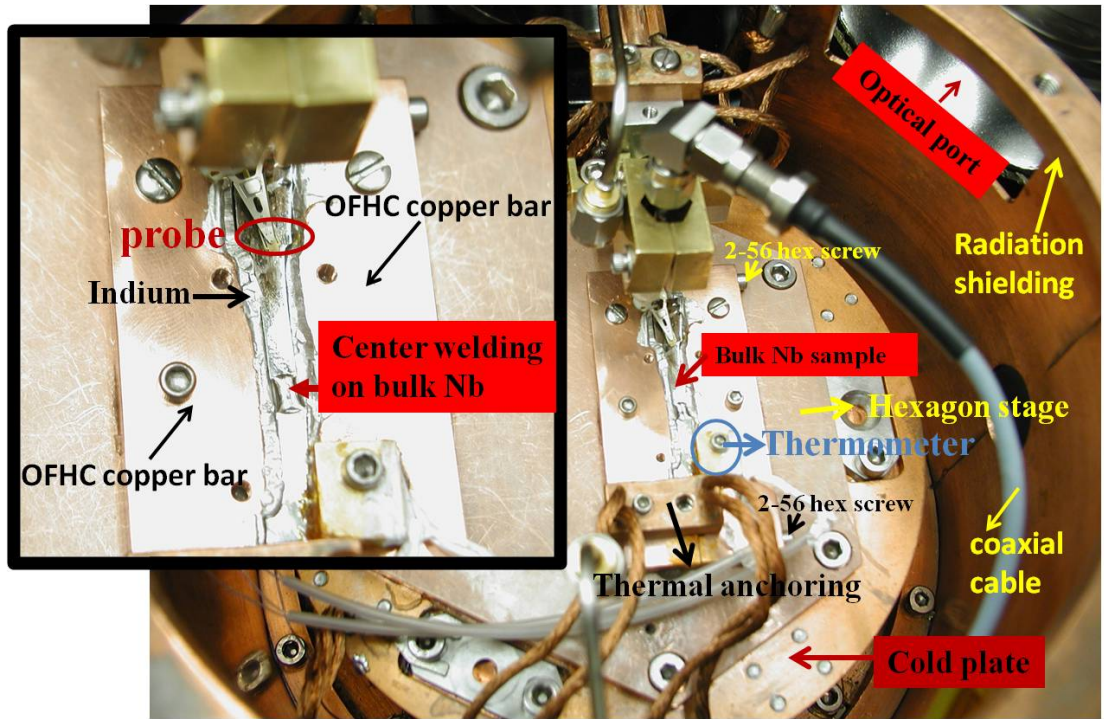
Fig. 5.15: The setup inside the cryostat probe station for measuring the bulk Nb nonlinearity. The zoom-in picture on the left side is to highlight the magnetic write head probe on the surface of the bulk Nb. Note the radiation shielding and thermal anchoring, which are critical for cooling the bulk Nb sample below T_c.

for bulk Nb nonlinearity measurement. The bulk Nb sample is clamped in place by two halves of an Oxygen-free high conductivity (OFHC) copper bar. Indium is filled within the gap between the Nb sample and OFHC copper bar to reduce the thermal resistance between bulk Nb and the OFHC copper bar. The two halves of the bar are bolted together laterally by two 2-56 hex-head screws from the side and then the whole OFHC copper bar assembly is bolted directly onto the surface of the sample stage in the cryostat with vacuum grease in between to reduce the thermal resistance. Note that the sample stage is also made of OFHC copper and is also firmly bolted on the top of the cold plate. The thermometer is placed on the bulk Nb top surface to monitor the temperature of the relevant surface of the bulk Nb. One OFHC copper cryogenic radiation shield is attached to the cold head of the cryostat. The lid of the radiation shield has a 3 inch diameter infrared blocking window as a view port. This setup can cool down the bulk Nb sample to 5 K without pumping the liquid helium exhaust from the cryostat. By pumping the liquid helium exhaust, the surface temperature of the Bulk Nb can go below 4 K. However 5 K is already enough to analyze the surface microwave properties of this bulk Nb sample. Note that if these extensive precautions are not taken, it is virtually impossible to cool the surface of bulk Nb down below its transition temperature.

5.4.2   Third Harmonic Measurement Results on Bulk Nb

The measurement is performed on many relatively flat surfaces on the bulk Nb sample with T_c of 9.2 K. The probe height is determined by optical microscopy from the side of the cryostat combined with $S_{11}(f)$ measurement to decide the best
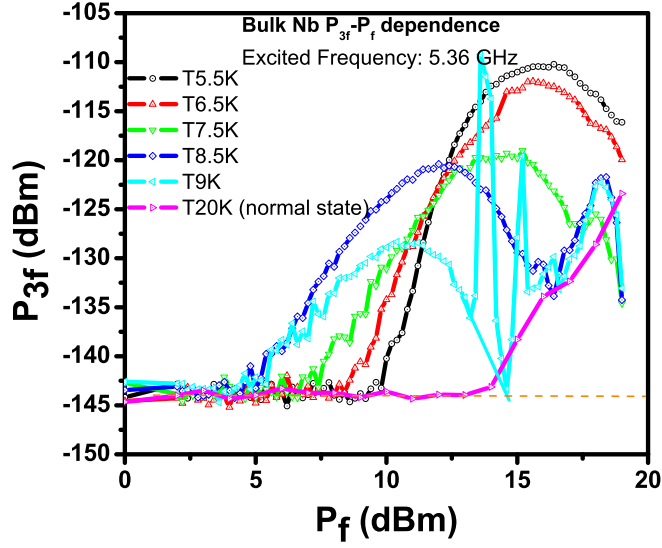
Fig. 5.16: The P_{3f} dependence on P_f at some specific temperatures for local microwave excitation of bulk Nb with the GT5 probe. Note the T_c of the bulk Nb sample is 9.2 K. The P_{3f} at T=20K indicates the probe nonlinearity itself.

excitation frequency. The probe height is approximately within 1 μm from the bulk Nb surface. Different points show slightly different microwave properties and will be illustrated qualitatively in this section.

Figure 5.16 shows one of the representative measurements for the power dependence of P_{3f} with respect to fundamental power P_f at many specific temperatures under 5.36 GHz excitation. All of the curves measured below T_c show a sharp P_{3f} onset from the noise floor of the spectrum analyzer and then follow a continuous increase of nonlinearity until a turnover at high excitation power. The onset of the nonlinear response is temperature dependent and can be defined as a temperature dependent lower critical power, P_{c1}. For high temperatures, the onsets kick off at low excitation power and start at higher excitation for lower temperatures. This

85
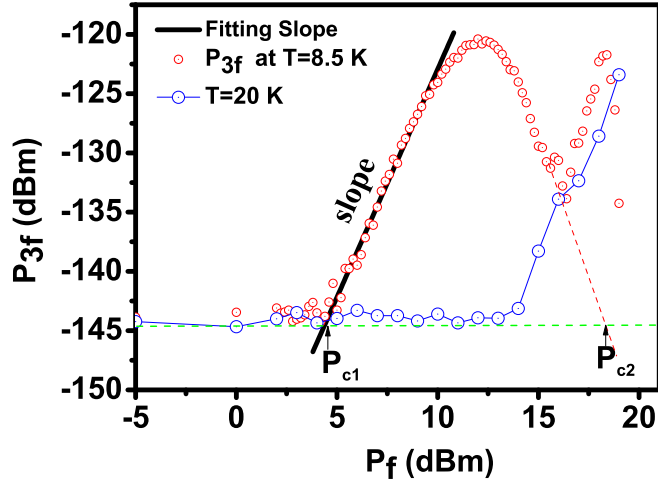
Fig. 5.17: The definition of three new parameters, P_{c1}, P_{c2} and slope after the onset from the P_{3f} versus P_f data on bulk Nb with the GT5 probe. This data is from Fig. 5.16 at T=8.5 K as a representative case to define these new parameters. The P_{3f} at T=20K is also included to illustrate the probe nonlinearity contribution.

means larger excitation power is required to create nonlinear response at lower temperature. In addition, after the turnover, all $P_{3f}(P_f)$ curves tend to decrease with increasing power, suggesting that we are destroying superconductivity. The linear extrapolation of P_{3f} to the noise floor can be defined as an upper critical power, P_{c2}, which suggests that superconductivity will eventually be destroyed due to high magnetic field. Figure 5.17 illustrates the criteria for defining the new parameters, P_{c1} and P_{c2}. In addition, the slope after each onset is also analyzed. Both the temperature dependent P_{c1} and P_{c2} are plotted together in Fig. 5.18 (a) and the temperature dependent slope is also plotted in Fig. 5.18 (b). These plots are similar to the temperature dependent critical fields of bulk Nb.

The analysis of the temperature dependent P_{c2} will benefit the understand-
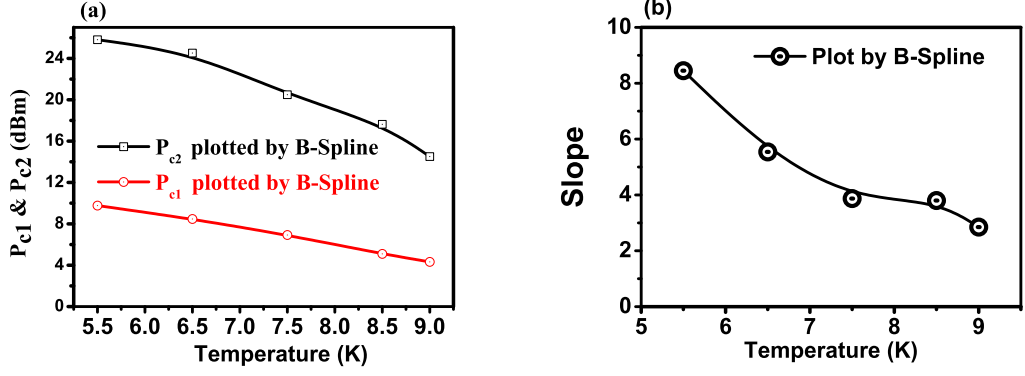
Fig. 5.18: (a) Temperature dependent P_{c1} and P_{c2} extracted from the data on bulk Nb shown in Fig. 5.16. (b) Temperature dependent slope of $P_{3f}(P_f)$ just after the onset of nonlinear response above the noise floor.

ing of surface field excited by the GT5 probe. Generally, one can assume that the relation of input critical power and surface critical field can be modeled as $P_c(T) = k\,[B_c(T)]^2$, where k is the unknown constant relating the power to the magnetic field. The temperature dependent B_c can be approximated by $B_c(T) = B_c(0K)\left[1 - \left(\frac{T}{T_c}\right)^2\right]$ with $B_c(0K) = 0.21\ Tesla$ for the bulk Nb thermodynamic critical field at 0 K. Fig. 5.19 (a) shows the fit of experimental $P_{c2}(T)$ with the model by adjusting the value of k. When $k = 22.2\ W/T_{esla}^2$, the model and the experimental P_{c2} data have the minimum deviation. By taking $B_c = \sqrt{\frac{P_c(T)}{k}}$ with $k = 22.2\ W/T_{esla}^2$, the surface critical field excited from the GT5 probe can be extracted. Fig. 5.19 (b) shows the temperature dependent thermodynamic critical field deduced in this manner. The fact that the $P_{c2}(T)$ data is fit by this simple $B_c(T)$ expression implies that the field generated from the GT5 probe can achieve the thermodynamic critical field at high power.

At the same probing point, the temperature dependent $P_{3f}(T)$ is also measured
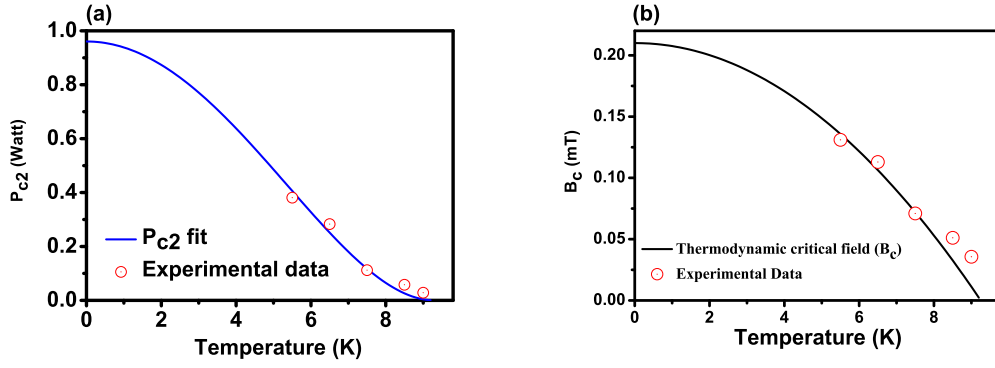
Fig. 5.19: (a) A fit of experimental $P_{c2}(T)$ with a simple model. (b) A fit of the experimental temperature dependent $B_{c2}(T)$ with the approximate equation: $B_c(T) = B_c(0K)\Big(1 - (T/T_c)^2\Big)$.

at a specific power and 5.36 GHz excitation as shown in Fig. 5.20. First, one finds there is a suppression of the T_c at the higher power. We think that this is due to heating of the sample by the driving probe during the measurement. A good thing is that this heating effect from the probe is still small but measurable. This, combined with the high power results in Fig. 5.16, suggest that the write head probe is producing extremely intense localized RF magnetic field excitation of the bulk Nb surface. This means that we have accomplished one of our key objectives for this microscope. Second, there is a suppression of the nonlinearity at the lower power but a saturated nonlinearity at the higher power at low temperature. From this temperature dependent nonlinear behavior, the measured response at the high power is consistent with the nonlinearity from the Josephson effect [87]. This situation will happen on the bulk Nb surface due to the presence of oxides and hydrides forming a weak link Josephson junction. The detailed discussion of possible extrinsic nonlinear mechanisms on bulk Nb will be given in Chapter 6.
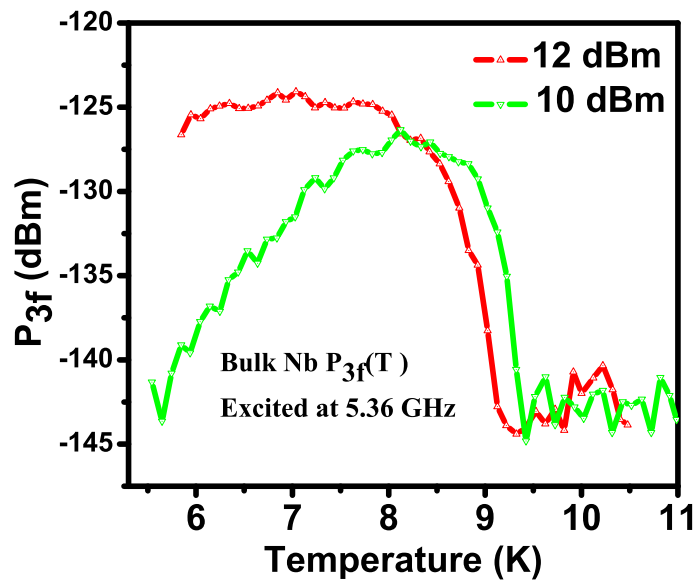
Fig. 5.20: The temperature dependent $P_{3f}(T)$ at some specific input powers and 5.36 GHz excitation. Note the T_c of the bulk Nb sample is 9.2 K and the onset of nonlinearity at low excitation power also begins at exactly 9.2 K. The onset of nonlinearity at higher excitation power occurs at a lower temperature, suggesting that localized heating of the bulk Nb surface has occurred.

The GT5 magnetic probe was also used to perform the same power dependence and $P_{3f}(T)$ measurement on another representative point on the sample. Figure 5.21 shows the P_{3f} dependence on P_f at selected temperatures at this position. The nonlinear properties for temperatures above 6.7 K seem to be similar to that of Fig. 5.16 including a later onset of nonlinearity with decreasing temperature, followed up with a turnover while gradually increasing the excitation power. However, at very low temperature (for example at 4.7 K), the curve of P_{3f} versus P_f shows an additional peak while the excitation power is between -2.5 dBm and 7 dBm. This may imply some nonlinearity is excited at very low temperature. One possibility is that the Nb hydride or Nb oxide has lower T_c or forms another weak link Josephson junction which has lower critical temperature. We analyze the slope of P_{3f} on P_f from the first onset and the second onset as illustrated in Fig. 5.22 (a). Fig 5.22 (b) is a slope summary after analysis. Note that if there is only one onset of nonlinearity (for the case while temperature is above 6 K), the two curves is treated as a regular single slope value after the single onset. One can see the red line is "analogous" to the lower critical field and the black line is "analogous" to the upper critical field. This may imply the first onset is due to the extrinsic Josephson nonlinearity and then the second onset is due the the penetration of the first Josephson vortex.

The temperature dependent $P_{3f}(T)$ at the same probe position is shown as Fig. 5.23. The onset of Nb nonlinearity begins immediately at the bulk Nb T_c (9.2 K) and then quickly saturates before T=8 K for 5.5 dBm, 5.025 GHz excitation. The nonlinearity shows a dip around 5.8 K. Below 5.8 K, the nonlinearity increases again. This behavior also happens at low excitation power at 0 dBm. The possible
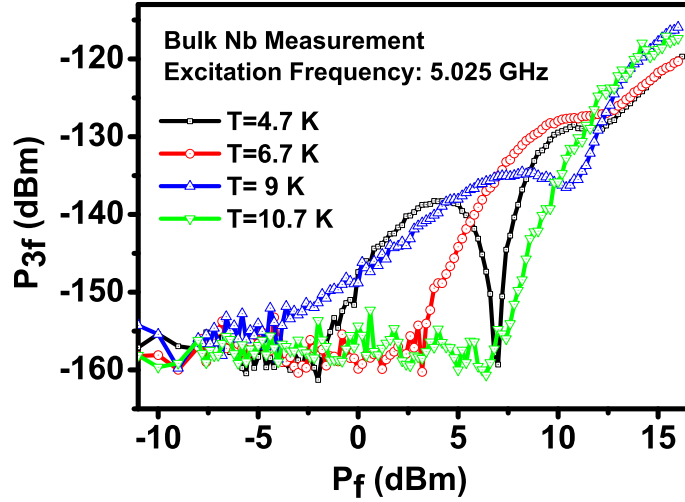
Fig. 5.21: The P_{3f} dependence on P_f at selected specific temperatures on the bulk Nb sample with the GT5 probe. The P_{3f} dependence on P_f at 4.7 K shows a different nonlinear behavior compared to the other two temperatures. Note that the nonlinearity of the probe measured at T=10.7 K is higher compared to the previous measurement in Fig. 5.16 due to different excitation frequency and slight difference of the probe height.
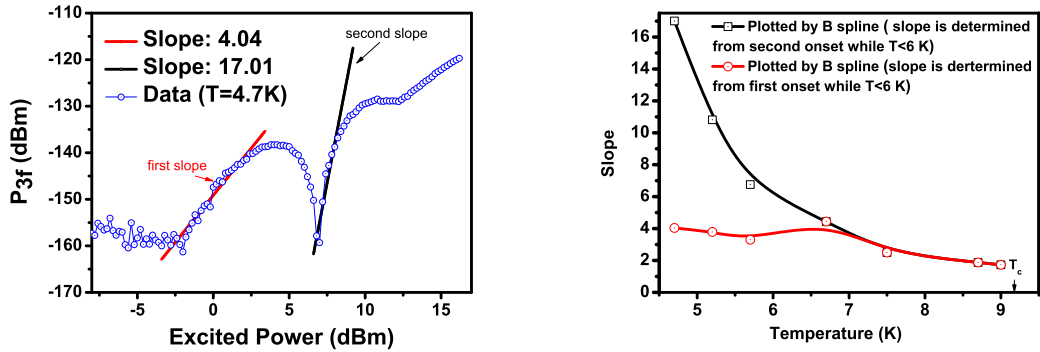
Fig. 5.22: (a) Illustration of how two slopes are selected from two onsets of P_{3f} versus P_f in Fig. 5.21. (b) Temperature dependent slope values for the data from Fig. 5.21 showing an analogue to upper and lower critical field versus temperature.
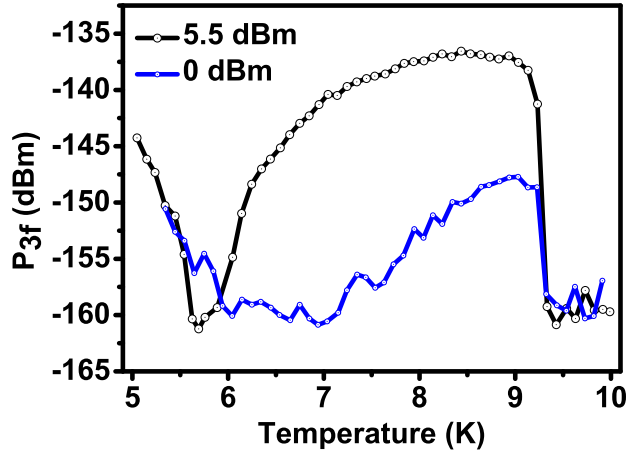
Fig. 5.23: The temperature dependent $P_{3f}(T)$ of the bulk Nb sample at two specific powers. The excitation frequency of the GT5 probe in this measurement is 5.025 GHz.

nonlinear mechanisms for bulk Nb will be discussed in Chapter 6.

5.5   Chapter 5 Conclusions

A clear reproducible nonlinear response signal from superconducting samples of TBCCO, MgB_2, sputtered Nb thin films and bulk Nb are all obtained by the magnetic write head probe. For thin film measurement, in addition to the P_{3f} peak at T_c due to the modulation of superconducting ordered parameter near T_c, the third harmonic response below T_c shows a nonlinearity likely from the Abrikosov vortex critical state and possible weak link Josephson junction on the surface. From the bulk Nb measurement, the third harmonic response is different from that of thin films. The nonlinearity due to the modulation of superconducting ordered parameter near T_c cannot be detected because the larger thickness dramatically reduces

this nonlinear mechanism. The measured nonlinearity of the bulk Nb samples shows a mechanism likely from the weak link Josephson junctions due to the contaminated surface in the fabrication process. The success of nonlinear excitation on bulk Nb also implies the magnetic field from the probe is higher than the H_{c1} of the measured bulk Nb sample. Therefore the nonlinear near-field magnetic field microwave microscope has great potential to identify the electrodynamic properties of bulk Nb materials and to image the electrodynamic defects on superconducting Nb in the GHz frequency region.

6. MODELING THE EXTRINSIC NONLINEARITY IN NB MATERIALS

Overview of the Chapter

This chapter will discuss the possible extrinsic nonlinear mechanisms for the Nb nonlinearity measurement, especially for the bulk Nb measurements in section 5.4. Three models will be covered here to study if the bulk Nb nonlinearity can be interpreted successfully by the existing models from the published literature and our newly proposed model. The three nonlinear models include the nonlinear mechanism from moving vortices [57], weak-link Josephson effect [87][88], and the proposed model of switching events between the vortex critical state and the Meissner state.

6.1 Model of nonlinearity coming from moving vortices in Type-II Superconductors

When the surface magnetic field approaches the lower critical field (B_{c1}) of type-II superconductors, vortices will overcome the barrier of the surface potential energy and penetrate into the superconductor. This surface barrier energy was first calculated by Bean and Livingston in type-II superconductors assuming a perfect

planar surface in a uniform and parallel applied field [83]. We consider the dynamic process of a strong AC magnetic field locally applied parallel to the surface of a bulk superconductor. This situation may occur for our GT5 longitudinal recording write head probe over the bulk Nb superconductor. Figure 6.1 illustrates the dynamical process in detail. Here we consider a simple process in which only a single vortex enters the superconductor in the first half of the RF cycle. In the beginning of the first half of the RF cycle, the Meissner screening currents on the surface increase with the increasing magnetic field to prevent the penetration of the applied magnetic field. However, once the applied field $B(t)$ exceeds the local penetration field (B_v), a vortex starts to nucleate on the surface of the superconducting material and a vortex semi-loop is created. After nucleation, the Meissner screening currents create a Lorentz force on the semi-loop vortex and push the vortex down into the material. Therefore, the vortex penetrates and moves into the material as shown in Fig. 6.1 (a). This vortex also creates a supercurrent circulating around the core and distorts the existing Meissner screening current due to the applied RF field near the surface. The total Meissner current is a combination of Meissner current coming from the applied RF field and the supercurrent from the vortex. The reduction of the total Meissner screening current between the surface and the vortex decelerates the moving vortex.

At the time when the RF field changes sign, the vortex penetrates to the maximum distance and then it turns around and starts coming back because the corresponding Lorentz force on the vortex changes sign. From Fig. 6.1 (b), during the reverse part of the RF cycle, the total Meissner screening current between the

95
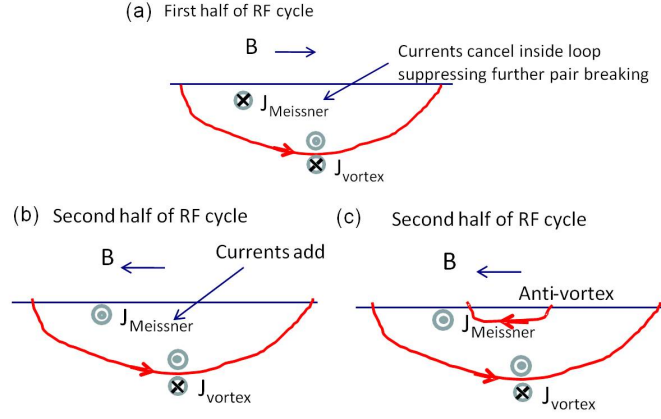
Fig. 6.1: Illustration of a vortex semi-loop nucleation, entry, exit and an anti-vortex nucleation, entry during one period of the RF cycle at a superconducting surface subjected to an intense localized magnetic field. The blue circles illustrate the direction of flow of screening currents in the superconductor.

surface and the vortex is now enhanced. Therefore once the total Meissner screening current reaches the depairing limit of Cooper pairs, an anti-vortex semi-loop will penetrate into the superconductor as shown in Fig.6.1 (c). Finally, the outgoing vortex will annihilate with the anti-vortex at some intermediate location. Generally speaking, this procedure of vortices moving in and annihilating in the film induces a dynamic instability and generates harmonic electromagnetic response. It is also a mechanism of dissipation of energy and results in suppression of the quality factor Q of SRF cavities [57][58].

Mathematically, the equation of motion of a vortex parallel to the surface of a semi-infinite superconductor is given by [57]

$$\eta \dot{u} = \frac{\Phi_0 B_0}{\mu_0 \lambda(T)} e^{-u/\lambda(T)} sin(\omega t) - \frac{\Phi_0^2}{2\pi \mu_0 \lambda^3(T)} K_1 \left(\frac{2\sqrt{u^2 + \xi_s^2}}{\lambda(T)} \right) \tag{6.1}$$
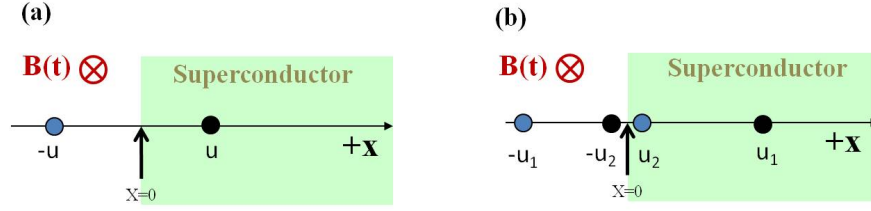
Fig. 6.2: (a) The solid black circle shows the position of the vortex which is pointing into the page and the solid blue circle shows the position of the antivortex image. Vortex is penetrating a distance $u(t)$ from the semi-infinite surface $(x = 0)$ exposed to a uniform parallel RF field $B(t)$. (b) The dots at u_1 and u_2 indicate the existing vortex and a newly created antivortex respectively. $-u_1$ is the position of the existing antivortex image and $-u_2$ is the position of the newly created vortex image.

where u is the coordinate of the vortex position with respect to the surface (x=0) as shown in Fig. 6.2 (a), $\lambda(T)$ is the temperature dependent penetration depth, $\eta = \frac{\Phi_0 B_{c2}}{\rho_n}$ is the Bardeen-Stephen vortex viscosity, ρ_n is the normal state resistivity, B_{c2} is the upper critical field of the superconductor, Φ_0 is the flux quantum, ω is the angular frequency of the oscillating field, μ_0 is the permeability of vacuum, B_0 is the magnitude of the RF magnetic field on the superconducting surface and $K_1(x)$ is the modified Bessel function. In addition the local coherence length ξ_s is also introduced to provide a cut-off in London theory. The left side of the equation is the viscous force on the moving vortex. This assumes that the vortex inertia $(m\ddot{u})$ and pinning force (ku), where m is the mass of the vortex and k is the pinning force constant, are negligible compared to the viscous force $(\eta\dot{u})$ [89]. The first term on the right hand side is the Lorentz force per unit length on the vortex due to the screening currents created by the driving field. The second term on the right is the force per unit length exerted by the image vortex that arises from the SC/vacuum

surface. This equation assumes a bulk superconductor.

The first vortex will penetrate into the superconductor when the impressed energy from the applied field $B(t)$ exceeds the Bean-Livingston surface barrier [83]. This barrier can be described in terms of a vortex penetration field, B_v. That is, the vortex will move into the superconductor when the applied field is bigger than B_v. Generally B_v can be approximated as $B_v \approx 0.71 * B_c$ [57] where B_c is the thermodynamic critical field. Therefore the time for the first vortex entry can be determined as [57],

$$
\begin{cases}
t_0 = \frac{\arcsin(B_v/B_0)}{\omega} \\[2mm]
u = 0,
\end{cases}
\tag{6.2}
$$

where we assume $B_v < B_0$. The vortex will move down into the material and reach the deepest depth at the time when the applied RF field changes sign during the RF cycle. After that, the vortex changes the direction of movement and begins to move toward the surface. An antivortex will nucleate when the Meissner current density due to the applied field plus the current density of the outgoing vortex (located at $x = u_c$) reaches $\frac{|B_v|}{\mu_0 \lambda}$ at the time t_c, at which point

$$
|\frac{B(t_c)}{\mu_0 \lambda}| + \frac{\phi_0}{\pi \mu_0 \lambda^3} K_1 \left(\frac{u}{\lambda}\right) = \frac{B_v}{\mu_0 \lambda}
\tag{6.3}
$$

Therefore once $t > t_c$, two anti-aligned vortices are inside the material and then move toward each other with coordinates u_1 for the outgoing vortex and u_2 for the newly created antivortex, as shown in Fig. 6.2 (b). The equation of motion for

these two vortices can be described as

$$\eta \dot{u}_1 = \frac{\Phi_0 B_0}{\mu_0 \lambda} e^{-u_1/\lambda} sin(\omega t) - \frac{\Phi_0^2}{2\pi\mu_0\lambda^3} \left[K_1\left(\frac{2u_1}{\lambda}\right) + K_1\left(\frac{u_1 - u_2}{\lambda}\right) - K_1\left(\frac{u_1 + u_2}{\lambda}\right) \right]$$

(6.4)

and

$$\eta \dot{u}_2 = \frac{\Phi_0 B_0}{\mu_0 \lambda} e^{-u_2/\lambda} sin(\omega t) - \frac{\Phi_0^2}{2\pi\mu_0\lambda^3} \left[K_1\left(\frac{2\sqrt{u_2^2 + \xi_s^2}}{\lambda}\right) - K_1\left(\frac{u_1 - u_2}{\lambda}\right) - K_1\left(\frac{u_1 + u_2}{\lambda}\right) \right]$$

(6.5)

A solution for the trajectory of the vortices describe by the above equations is shown in Fig. 6.3 (bottom frame) as a function of time for two RF cycles. The applied RF field $B(t)$ is also included on the top frame to illustrate the relation of the vortex position and the applied field with time. This calculation is performed under the assumption of 5 GHz excitation on the bulk Nb surface with B_c=200 mT ($B_v = 142\ mT$) and the peak value of applied field B_0= 160 mT. Besides, $\lambda = 40$ nm, $\xi_s = 3\ nm$, $\rho_n = 10^{-9}\ \Omega m$ and $B_{c2} = 400\ mT$ are assumed typically for bulk Nb. The second vortex will annihilate with the first vortex at time t_c, leaving the sample temporarily free of vortices. This procedure of vortex-antivortex entry and annihilation continues in the next RF cycle, and will generate a third harmonic signal, as shown below.

The reason why vortex-antivortex entry and annihilation creates a harmonic response is that this motion results in a complicated time dependent fluctuation of flux in the sample. Physically the induced electromotive force (voltage) is the time

99
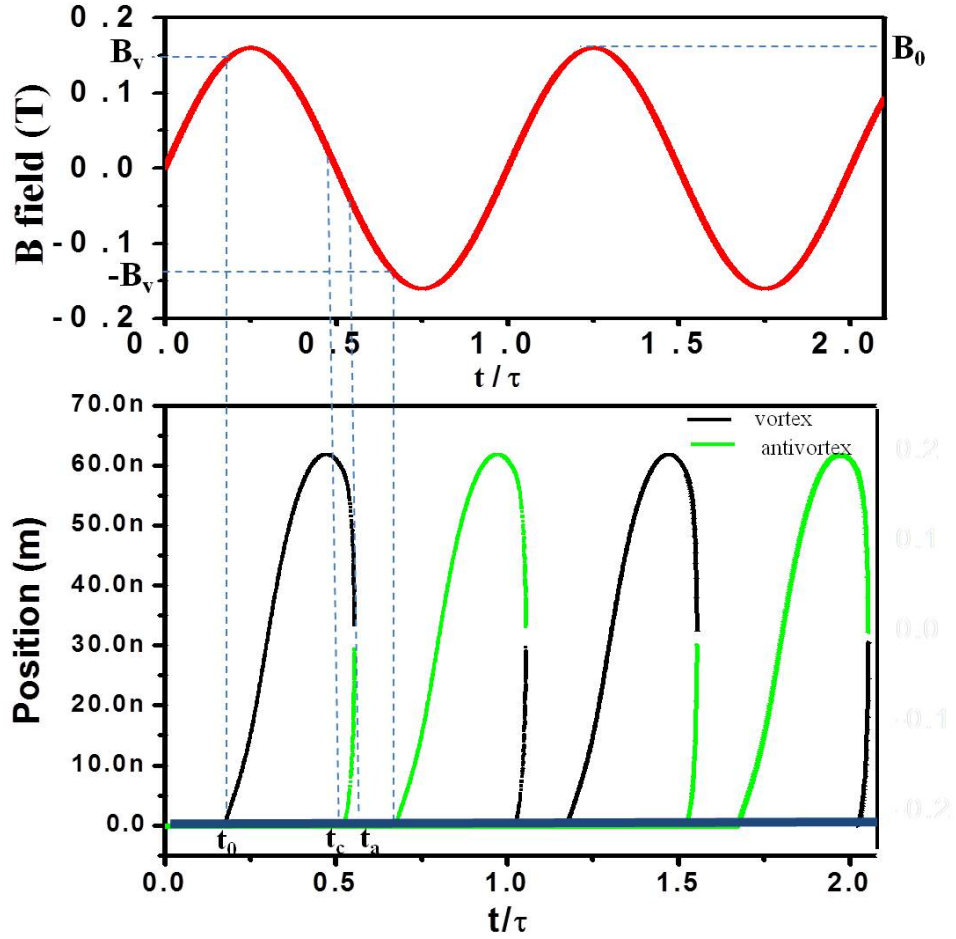
Fig. 6.3: Calculation of vortex position at 5 GHz excitation ($\tau = 200 \ ps$) bulk Nb with the relation of the applied RF field ($B(t)$) in two RF cycles. t_0 indicates the time when the applied magnetic field exceeds the Bean-Livingston barrier ($B(t) > B_v$). t_c indicates when an anti-vortex begins nucleating at the surface and t_a indicates the time when the vortex and the anti-vortex collide and annihilate each other. The calculation assumes $\lambda = 40 \ nm$ and $\xi_s = 3$ nm typically for bulk Nb with $\rho_n = 10^{-9} \ \Omega m$ and $B_{c2} = 400 \ mT$ to calculate the Bardeen-Stenphen vortex viscosity.

derivative of flux in the sample

$$V(t) = \frac{d}{dt}\Phi \qquad (6.6)$$

, where Φ is the flux in the sample.

Figure 6.4 schematically shows the change of normalized fluxoid number in the time domain during the RF cycle. One can clearly see that the change of fluxoid in the superconductor happens at the times t_{01}, t_{c1}, t_{02}, and t_{c2}, where t_{01} / t_{02} are the times of vortex/antivortex penetration into the superconductor. Similarly, t_{c1}/ t_{c2} are the times at which the total flux in the superconductor drops to zero because of the appearance of an antivortex/vortex pair. A time dependent voltage spike, which we approximate as a gaussian pulse, is assumed whenever a change of fluxoid number happens in the time domain,

$$V_t(t, \sigma, t_s) = e^{\frac{-(t-t_s)^2}{2\sigma^2}} \qquad \sigma \equiv \frac{h}{\Delta} \qquad (6.7)$$

where t_s is the time when the number of fluxoids inside the material changes, h is Planck's constant and Δ is the superconducting gap at zero temperature. σ is a time scale on the order of 1 ps. The amplitude of the third harmonic voltage, V_{3f} can be extracted by the numerical Fourier transform

$$
\begin{aligned}
V_{3fa} &= \frac{2}{\tau} \sum_{m=0}^{\frac{\tau}{\Delta t}-1} V_t sin(3\omega m \Delta t)\Delta t \\
V_{3fb} &= \frac{2}{\tau} \sum_{m=0}^{\frac{\tau}{\Delta t}-1} V_t cos(3\omega m \Delta t)\Delta t
\end{aligned}
\qquad (6.8)
$$
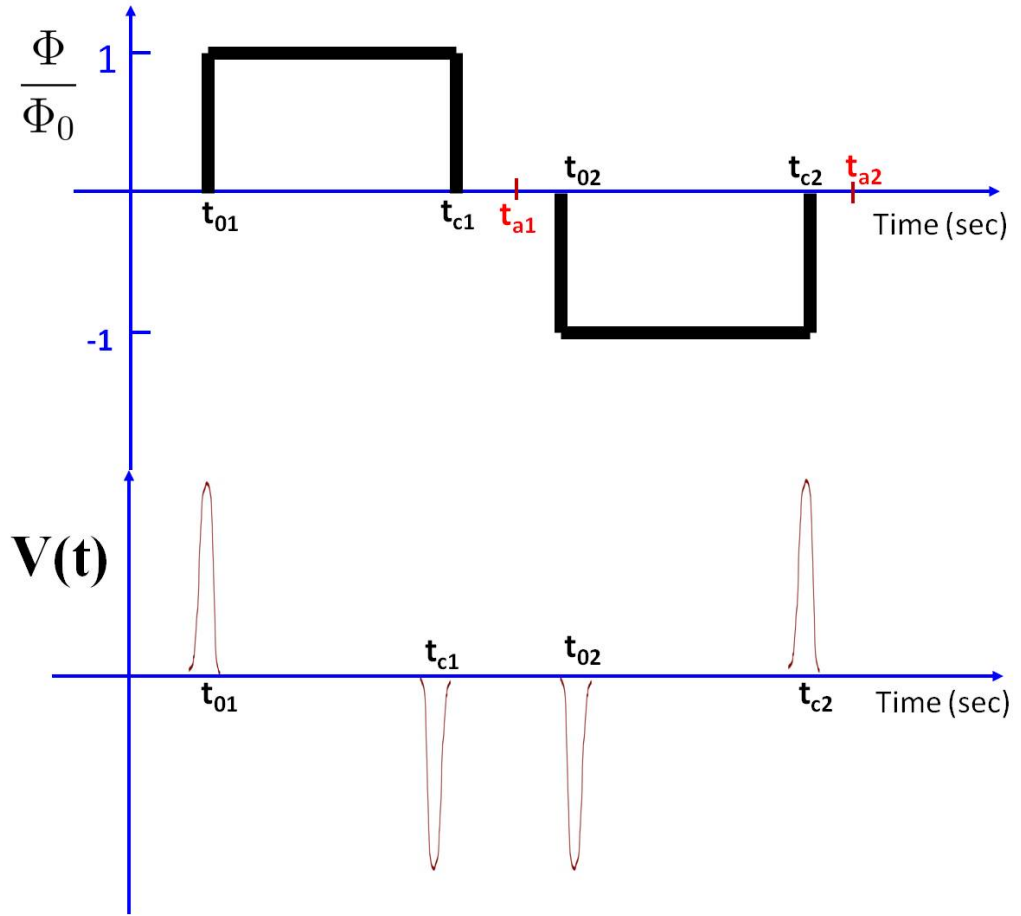
Fig. 6.4: (Upper Frame) Schematic illustration of the quantized fluxoid number during an RF cycle. t_{01} is the time when the penetration of the first vortex happens in the first half of the RF cycle. t_{c1} is the time when the first antivortex nucleates on the superconductor surface and t_{a1} is the time of annihilation for the first vortex and the antivortex in the first half of a RF cycle. For the second half of a RF cycle, t_{02} and t_{c2} mean the time of nucleation for another antivortex and vortex, respectively. Similarly, t_{a2} is the time of annihilation for this vortex-antivortex pair during the second half of the RF cycle. (Bottom Frame) The generated voltage spikes due to the change of the quantized fluxoid number in an RF cycle.
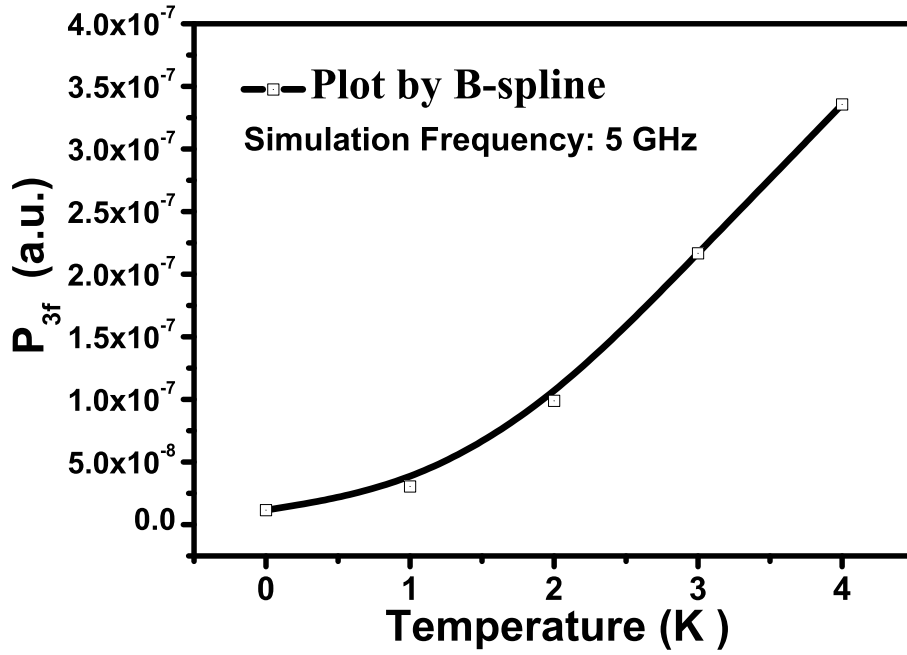
Fig. 6.5: Plot of calculated $P_{3f}(T)$ obtained from the vortex nucleation, penetration and annihilation model, in arbitrary units.

where the sum on m covers the RF time period (τ) in terms of m discrete time (Δt) steps. Finally, the third harmonic power generated by this vortex mechanism can be calculated using the following equation

$$P_{3f} = \frac{\sqrt{V_{3fa}^2 + V_{3fb}^2}}{2Z_0} \tag{6.9}$$

Fig. 6.5 shows the calculated temperature dependent $P_{3f}(T)$ from this simple vortex mechanism. The calculation is only done at 0K, 1K, 2K, 3K and 4K. Above 4K, the applied field (B_0) is already much larger than the vortex penetration field (B_v) and there is more than one vortex entering the sample. Hence at

103

higher temperature, the calculation will become very complicated. However, generally, this mechanism will produce small nonlinearity at low temperature but higher nonlinearity at higher temperature. This result seem to be at odds with most of our measurements. For our $P_{3f}(T)$ measurement under high power excitation (as shown in Fig. 5.9 or Fig. 5.20 at excitation power 12 dBm), the nonlinearity either increases or saturates with decreasing temperature. Nonlinearity due to the mechanism of vortex generation and annihilation is simply not consistent with most of our our measurements. The following statements may be possible reasons for this inconsistency.

(1) The vortex mechanism is actually significantly more complicated than this simple model, especially in a high RF magnetic field. In the vortex calculation, the applied field ($B_0 = 160$ mT) is just slightly higher than the vortex penetration field of Nb ($B_v = 142$ mT). If the amplitude of the applied field is much larger than the vortex penetration field ($B_0 \gg B_v$), a second or even a third vortex will nucleate before the annihilation of the first vortex and antivortex pair. This will result in a very complicated set of interactions. In addition, in the model, the pinning effect due to the presence of defects inside the superconductor is not included. In the real case, the vortex can be pinned by a chain of defects. The resulting vortex line will oscillate [57] and may create a measurable nonlinearity. In addition, the model does not include a voltage pulse associated with the annihilation of the vortex/anti-vortex pair inside the superconductor.

Additionally, the model assumes a flat superconducting surface. In a rigorous case, a geometry factor of the surface roughness should be taken into consideration

especially when the surface has roughness with characteristic length $\geq \xi$ (the coherence length) [90]. Generally, for a sharp corner on the surface, the Meissner screening current density will be enhanced and the penetration field of the first vortex entry (B_v) will decrease [90]. Finally, the calculation is done under the assumption of a straight vortex. If a vortex enters into the superconducting material in the form of a semi-loop due to the configuration of the magnetic field from the magnetic write head probe, considering the curvature of the vortex would be more realistic than the case of a straight vortex. The curvature of the vortex will influence the pinning effect on the defects and result in different harmonic response.

(2) Another possibility is that the write head itself has stray DC magnetic flux, and this flux may become pinned in the superconductor. The RF screening currents generated by the probe may create a nonlinear response of these trapped vortices.

(3) In addition to the nonlinearity from a moving vortex, there are other possible nonlinear mechanisms which can dominate the nonlinearity of the Nb superconductor. For example, the weak-link Josephson nonlinearity may happen due to the presence of surface oxides and hydrides that create Josephson tunnel barriers within a penetration depth of the surface. This nonlinearity is very significant at all temperatures ranges and becomes stronger at lower temperature. In addition, a nonlinearity from switching between the Meissner state and the vortex critical state may be another possible nonlinear mechanism. Both of the mechanisms will now be discussed in the following sections.
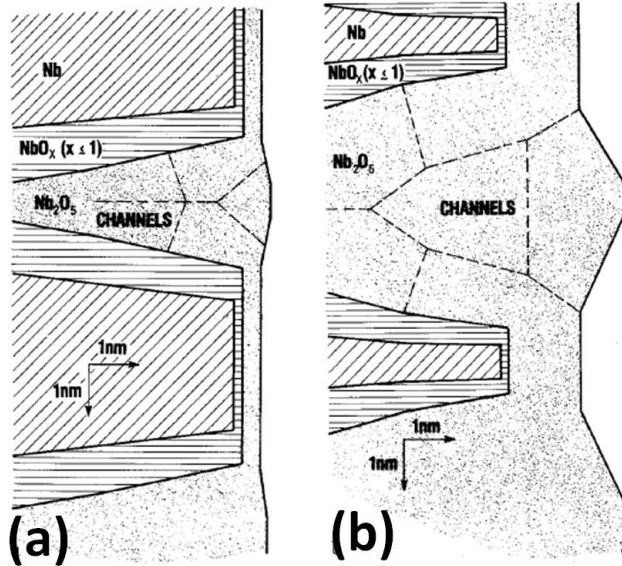
Fig. 6.6: The surface of Nb is undergoing exposure to air within 30 minutes in (a) to more than 1 week in (b). The fast serration and fast oxide growth is due to the strain caused by O dissolution in Nb and by Nb_2O_5 oxide nucleation at the Nb surface. Figure is taken from Ref.[49].

6.2   Nonlinearity from the weak-link Josephson effect

Another mechanism giving rise to the nonlinear electrodynamics of the super-conductor is the phase slip across a Josephson junction [88]. Josephson junctions will form on the inner surface of the bulk Nb cavities due to the inevitable oxidation in the air [50]. Fig. 6.6 shows the sketch of oxidation in air of a smooth, single crystal Nb with many oxide nuclei [49]. One can clearly see that from 30 min to one week exposure in an ambient environment, the NbO_x and Nb_2O_5 is still growing. This surface oxidation deteriorates the superconductivity because of the formation of possible S-I-S, S-N-S or S-C-S structures. Besides, Josephson junctions may also develop on the Nb surface due to the chemical surface treatment during fabrication.

106

For modeling the weak-link Josephson nonlinearity, one considers a perpendicular magnetic field component that induces a single screening current loop which consists of N identical superconducting grains as shown in Fig. 6.7. The superconducting grains are connected together and weakly coupled in a closed loop with area S. This loop can be driven by a combined DC field (B_{dc}) and RF field (B_1) on the superconducting surface giving rise to a total flux of

$$\Phi(t) = \Phi_{dc} - \Phi_1 cos(\omega t) \qquad where \qquad \Phi_{dc} = \frac{SB_{dc}}{\Phi_0} \qquad and \qquad \Phi_1 = \frac{SB_1}{\Phi_0} \quad (6.10)$$

where $\Phi(t)$ is the total magnetic flux through the loop, in units of the flux quantum Φ_0, Φ_{dc} is the normalized DC flux. Φ_1 and B_1 is the normalized flux and amplitude of the surface field from the RF field, respectively.

Figure 6.8 [88] shows the internal energy (E) of a loop of N grains versus the applied magnetic flux. The internal energy (E) is defined by the Josephson coupling Hamiltonian [88]. The applied magnetic flux as a function of time is also plotted on the bottom part of Fig. 6.8. In our experiment, Φ_{dc} is assumed to be zero because there is no applied DC field and because the P_{3f} measurement is performed in a well-shielded environment. Clearly, if $\Phi_1 > \Phi_c$, where $\Phi_c = 0.5$ corresponding to the first energy cusp, a phase slip will occur. Hence, for the amplitude shown, the phase slip will occur at 4 times in the RF cycle, at times t_1, t_2, $\tau - t_1$ and $\tau - t_2$ where τ is the RF period, $t_1 = (1/\omega)cos^{-1}[\frac{\Phi_{dc}+\Phi_c}{\Phi_1}]$ and $t_2 = (1/\omega)cos^{-1}[\frac{\Phi_{dc}+\Phi_c}{\Phi_1}]$. Note that in order to simplify the model, we don't consider the case while the applied field energy is higher than the second, third, etc. cusps in Fig. 6.8 because the calculation of
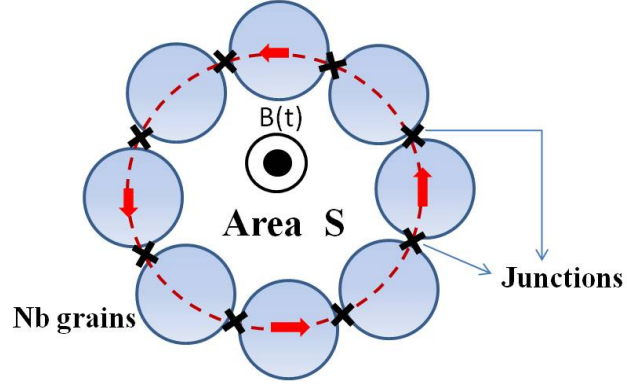
Fig. 6.7: Schematic illustration of an induced screening current loop created by the magnetic field pointing out of the paper. Multiple Nb grains are connected by weak link Josephson junctions between the grains. Note S is the area of the screening current loop.

$P_{3f}\left(P_f\right)$ would be more complicated.

The response voltage due to the phase slip of the Josephson junction is given by

$$V(t) = -\frac{\hbar}{2e}\frac{d\phi}{dt} \tag{6.11}$$

where ϕ is the phase difference across a Josephson junction. This voltage is a series of 4 delta functions in each RF period, corresponding to each of the 4 phase slip events. We project out the third harmonic voltage by making a sine and a cosine expansion in harmonics of the fundamental drive frequency.

$$
\begin{aligned}
V_{3fa} &= \frac{2}{\tau}\int_0^\tau V(t)sin(3\omega t)dt \\
V_{3fb} &= \frac{2}{\tau}\int_0^\tau V(t)cos(3\omega t)dt
\end{aligned}
\tag{6.12}
$$

108
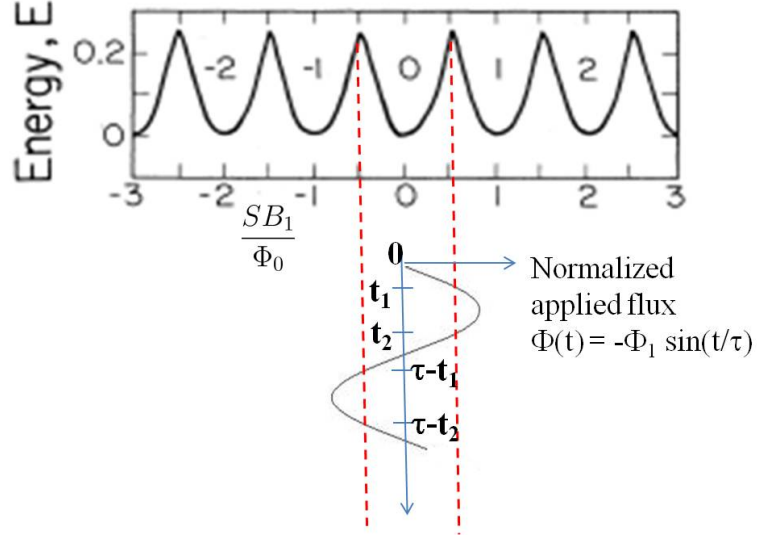
Fig. 6.8: Internal energy E of a loop of N grains vs normalized magnetic flux $\Phi = \frac{HS}{\Phi_0}$. The cusps of the energy appear when $\Phi = n+1/2$, $n = 0, \pm 1, \pm 2, ...$ Figure taken from Ref. [88]

This yields the following expression for the 3rd harmonic voltage:

$$
\begin{aligned}
V_{3fa} &= -\frac{\hbar}{e}\frac{2\pi\omega}{N}\Big[sin(3\omega t_1) + sin(3\omega t_2)\Big] \\
V_{3fb} &= -\frac{\hbar}{e}\frac{2\pi\omega}{N}\Big[cos(3\omega t_1) + cos(3\omega t_2)\Big]
\end{aligned}
\tag{6.13}
$$

where N is numbers of Josephson junctions in the loop.

In the experiment, the current loop couples back to the magnetic write head probe. Hence what we measure is an induced voltage in the magnetic write head probe given by $V_e = d\Phi_e/dt$ where Φ_e is the time dependent induced flux at the write head probe. To estimate the voltage induced on the magnetic probe, one can consider a magnetic dipole moment over the superconductor at a distance "a'' between the dipole and the superconducting surface [91] [92] [93]. The magnetic dipole can be described by a Dirac delta function $\mathbf{M} = \mathbf{m}\delta(x)\delta(y)\delta(z - a)$, where

m is the moment of the dipole. Therefore, the radial component of the generated screening current due to this dipole can be expressed as [75]

$$J_\rho(\rho, \theta) = -\frac{m\phi_0 sin\theta}{4\pi\lambda^3}\frac{\sqrt{\rho^2 + a^2} - a}{\rho^2\sqrt{\rho^2 + a^2}} \tag{6.14}$$

where ρ and θ indicate the radial distance and the azimuth angle with respect to an origin as shown in Fig. 6.9. The maximum current will be at the location $\rho \to 0$ and $\theta \to -\pi/2$.

$$J_\rho(\rho \to 0, \theta \to \pi/2) = \frac{m\Phi_0}{8\pi\lambda^3 a^2} \tag{6.15}$$

Note that the magnetic moment of the dipole M can be measured in units of $m_0 = \Phi_0\lambda$ so $m = \frac{M}{m_0} = \frac{M}{\Phi_0\lambda}$ [75] and probe height is also measured in unit of λ (that is $a \to \frac{a}{\lambda}$. Substituting the m into Eq. 6.15, the maximum current, J_{max} induced by a magnetic dipole moment M at a height "a" above the superconductor with penetration depth λ is given by.

$$J_{max} = \frac{M}{8\pi\lambda^2 a^2} \tag{6.16}$$

The magnetic dipole moment M also can be expressed in terms of the magnetic flux in the gap of the probe as $M = \Phi_e l_{gap}/\mu_0$, where l_{gap} is the length of the write gap. Hence the induced voltage on the probe can be written as

$$V_e = \frac{d\Phi_e}{dt} = \frac{d}{dt}\frac{\mu_0 M}{l_{gap}} = \frac{dJ}{dt}\frac{8\pi\mu_0\lambda^2 a^2}{l_{gap}} \tag{6.17}$$
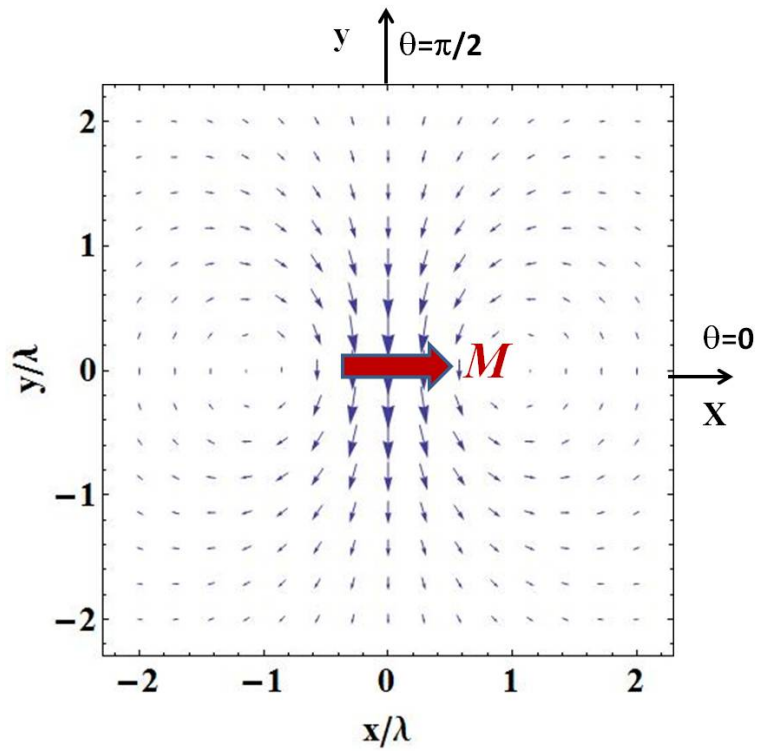
Fig. 6.9: The screening current (**J**) induced in a superconductor due to a point magnetic dipole **M** with a distance "*a*" above the superconducting surface plane (Z=a). Calculation from Ref. [75].

Take the 3rd harmonic current density $J_3 = I_3/(\lambda\ a)$, where I_3 is the third order harmonic current and combining with Eq. 6.13, one finds that the induced third harmonic voltage for sine and cosine expansion and the corresponding third harmonic power generated by this phase slip mechanism in the weak-link Josephson junction is given in the frequency domain by

$$V_{3fa}^e = \frac{96\mu_0\omega\lambda(T)aI_3(T)}{Nl_{gap}}[sin(3\omega t_1) + sin(3\omega t_2)]$$

$$V_{3fb}^e = \frac{96\mu_0\omega\lambda(T)aI_3(T)}{Nl_{gap}}[cos(3\omega t_1) + cos(3\omega t_2)] \tag{6.18}$$

$$P_{3f} = \frac{\sqrt{\left(V_{3fa}^e\right)^2 + \left(V_{3fb}^e\right)^2}}{2Z_0}$$

where $I_3 = I_c J_3(\beta)sin(3\omega t)$ with $\beta \equiv \frac{2\pi SB_1}{\Phi_0}$ coming from the third order expansion of the Fourier series for $I(t) = I_c sin(\beta sin(3\omega t))$ in terms of the Bessel function $J_n(\beta)$ [87]. Here I_c is the junction critical current and can be written as [94]

$$I_c(T) = \frac{\pi\Delta(T)}{2eR_n}tanh[\frac{\Delta(T)}{2k_bT}] \tag{6.19}$$

with $\Delta(T)$ the temperature dependent superconducting gap parameter, and R_n is the normal resistance of the junction.

The temperature dependence of the superconducting gap, $\Delta(T)$, can be computed numerically by the following equation [95]

$$\frac{1}{N(0)V} = \int_0^{\hbar\omega_c} \frac{tanh\frac{1}{2k_bT}(\xi^2 + \Delta(T)^2)^{1/2}}{(\xi^2 + \Delta(T)^2)^{1/2}}d\xi \tag{6.20}$$

112
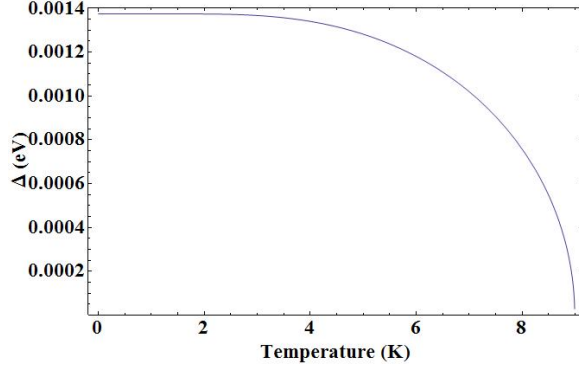
Fig. 6.10: Numerical calculation of temperature dependent BCS superconducting gap for Nb.

Here $N(0)$ is the density of states at the Fermi level, V is the potential energy of the two interaction electrons (pairing strength), k_b is Boltzman constant and T is temperature. The product of $N(0)V$ for Nb is approximated as $N(0)V \approx 0.39$ with the cut-off energy $\hbar\omega_c = ck_bT_c$ to determine the BCS temperature dependent superconducting gap for Nb. The constant, $c = 11.1$, is determined by numerically solving Eq. 6.20 to force $\Delta(T) = 0$ at the known T_c of the material. The numerical solution for Eq. 6.20 is shown in Fig. 6.10.

The BCS London penetration depth is defined by [98]

$$\lambda_L^2(T) \equiv \frac{1}{K(0,T)} \qquad ;$$

$$K(0,T) = \frac{1 - 2\int_{\Delta(T)+\epsilon}^{\hbar\omega_c} \frac{xe^{x/(k_bT)}}{\sqrt{x^2-\Delta(T)^2}k_bT\left(1+e^{x/(k_bT)}\right)^2}dx}{\lambda_0^2} \qquad (6.21)$$

Here the zero temperature London penetration depth of Nb, λ_0, is assumed to be 40 nm. $\epsilon = 10^{-12}$ is introduced to provide a cut-off in the integrand for numerical integration. Figure 6.11 is the fitting result to the bulk Nb $P_{3f}(T)$ data based

113

on this phase slip model. The experimental data is taken at 13 dBm excitation power and 5.44 GHz excitation frequency, similar to Fig. 5.20 at 12 dBm, 5.36 GHz excitation. In the calculation, the number of Josephson junction N in the current loop is assumed to be one. Both terms of $\left[sin(3\omega t_1) + sin(3\omega t_2) \right]$ and $\left[cos(3\omega t_1) + cos(3\omega t_2) \right]$ are also assumed to be on the order of one. Note that the product of $S * B_1$ (which comes from the definition of $\beta \equiv \frac{2\pi S B_1}{\Phi_0}$) and R_n will affect the calculated $P_{3f}(T)$. For simplicity, we assume S is a constant and the loop has the shape of a perfect circle with a diameter equal to the value of l_{gap}, which is 100 nm for the GT5 probe. In addition, Halbritter estimates that weak links on the surface of bulk Nb are about $10 \sim 100$ nm apart [96] [51]. Hence we take $S = 7.85 * 10^{-15}$ m^2. The distance between the probe and sample, a, is assumed to be 10 nm, which is the scale of flying height during the reading and writing process in the high speed magnetic recording [70] [76]. Therefore, two parameters, R_n and B_1, are left for fitting. The blue solid line in Fig. 6.11 is the fit result from this phase slip model with $R_n = 10.8$ Ω and $B_1 = 81$ mT. Here the value of B_1 was taken such that $\beta < 1$, in other words before the first peak of $J_3\left(\frac{2\pi S B_1}{\Phi_0} \right)$. Besides, Halbritter also estimated the specific junction resistance, which is resistance times cross-section area of the junction, to be $R_{bl} = 10^{-15}$ Ωm^2 [97] for a bulk Nb weak link junction. Take the weak link to be 10 nm deep [96] and assumed 100 nm long, the resistance will be on the order of 1 Ω. Compared to $R_n = 10.8$ Ω from my fit, the resistance value of my fit for weak link Josephson junction is physically reasonable. However, in general, both S and R_n should be temperature dependent parameters, as will be discussed later.

114
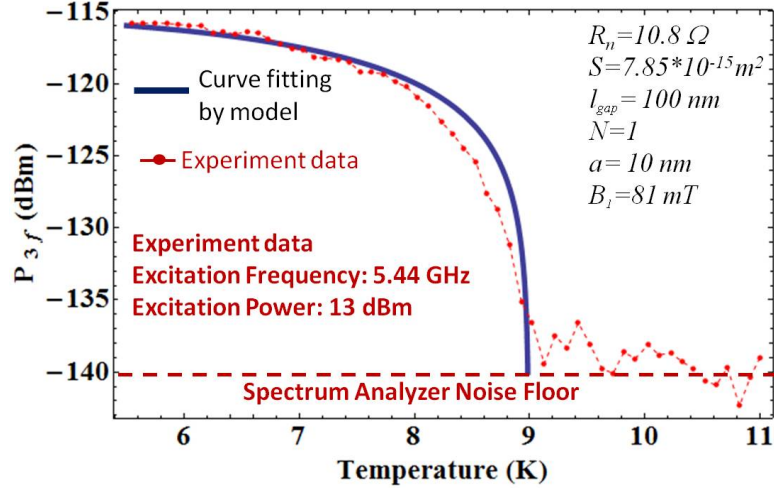
Fig. 6.11: Temperature dependence of the third harmonic response for the bulk Nb sample at the excitation power 13 dBm and excitation frequency 5.44 GHz measured by the GT5 probe (dot points). The noise floor of the spectrum analyzer at this excitation frequency is about -141 dBm. A calculated result (solid curve) based on the phase slip model is fit to the data. The fitting parameters are: $R_n = 10.8 \ \Omega$, and $B_1 = 81 \ mT$, with fixed values for the remaining parameters: $S=7.85 * 10^{-15} \ m^2$, $l_{gap}=100$ nm, $N = 1$, $a = 10 \ nm$.

From the power dependence measurement as shown in Fig. 5.16 and Fig. 5.21, one can see the probe nonlinearity, P_{3f}^{probe} always dominates the measurement at high excitation power. In order to extract the response from only the superconducting sample at high power, an effective P_{3f} is defined by taking the absolute value of the difference between the measured P_{3f} in the superconducting state and the measured P_{3f} in the normal state, without considering the phase of the measured nonlinearity. An offset to the original noise floor of the measurement is applied after taking the difference. Therefore, the effective P_{3f} can be regarded as the nonlinearity from just the superconducting sample, to first approximation.

The dot points in Fig. 6.12 and Fig. 6.13 show the effective P_{3f} at 9 K and 4.7 K, respectively, from the experimental data in Fig. 5.21. The solid line in Fig. 6.12

and Fig. 6.13 indicate the fit to the phase slip model for the temperatures of T=9 K and T=4.7 K, respectively. Due to the unknown coupling between the probe and the superconducting sample, the relation between the incident fundamental power, P_f, and actual surface magnetic field experienced on the bulk Nb surface is not possible to calculate. Therefore, we assertively take $P_f = kB_1{}^2$ with $k = 1$ directly for fitting the effective P_{3f}, where B_1 is the amplitude of the surface magnetic field on the bulk Nb superconductor and k is an arbitrary constant to connect power and magnetic field. The fits assume constant value of the probe height $a = 10\ nm$, the number of Josephson junctions $N = 1$, and the magnetic gap of the yoke $l_{gap} = 100$ nm. Two parameters, R_n and S, are varied to fit the model [Eq. 6.18] to the data. Varying R_n can adjust the amplitude of P_{3f} and varying S can laterally shift the theoretical curve to locate the first $P_{3f}(P_f)$ dip position in the experimental data. From Fig. 6.12, the dip position of the model at $P_f = 9.82$ dBm and $P_f = 13.52$ dBm are matched to the dip position of the effective P_{3f} measurement taken at 9 K under 5.025 GHz excitation by taking $S = 2.15 * 10^{-14}\ m^2$. The amplitude of P_{3f} at the first peak is matched to the model by taking $R_n = 90\ \Omega$. The fact that the amplitude of the effective P_{3f} does not match the theory for the second peak may be because the phase of the V_{3f}^{probe} is not included when subtracting the measured P_{3f} in the normal state from the measured P_{3f} in the superconducting state. For the data at T=4.7 K as shown in Fig. 6.13, the dip position of the model at $P_f = 10.69$ dBm is slightly different from the experimental data which shows a dip at $P_f = 11.4$ dBm. This slight difference may come from the effect of localized heating from the probe at low temperature because the heat sink at low temperature is not sufficient
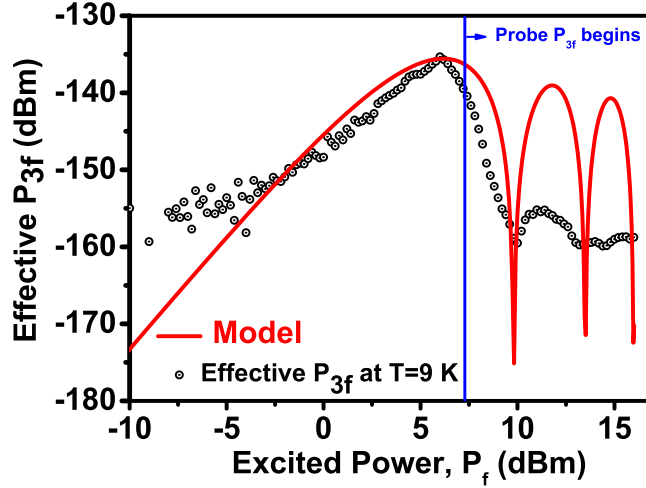
Fig. 6.12: Effective P_{3f} versus P_f for the bulk Nb sample measured by GT5 probe at 9 K under 5.025 GHz excitation as shown by the dot points. The solid line is the theoretical calculation based on the phase slip model of the Josephson junction. The parameters are as follows: T=9 K, Freqency=5.025 GHz, $R_n = 90$ Ω, $S = 2.15 * 10^{-14}$ m^2, $a = 10$ nm, N=1, $l_{gap} = 100$ nm. Only R_n and S were varied to perform the fit. The vertical blue line shows where the probe background nonlinearity has been naively subtracted from the data.

to carry away the generated heat. The S values for the fit at T=9 K (Fig.6.12) and at T=4.7 K (Fig. 6.13) are $S = 2.15*10^{-14}$ m^2 and $S = 3.0*10^{-14}$ m^2, respectively, equivalent to a circle with diameter $D = 165$ nm and $D = 195$ nm, respectively. The values of the circle diameters are on the scale of the magnetic gap (~ 100 nm) in the write head probe and imply the resolution of the magnetic write head probe in the near field microwave microscope. These length scales are also consistent with those put forward by Halbritter for the distance between weak links on the surface of air-exposed bulk Nb [49][51][96][97].

Comparing the R_n and S values from the model fits in Fig. 6.12 and Fig. 6.13, we see that these two parameters are temperature dependent. One reason for
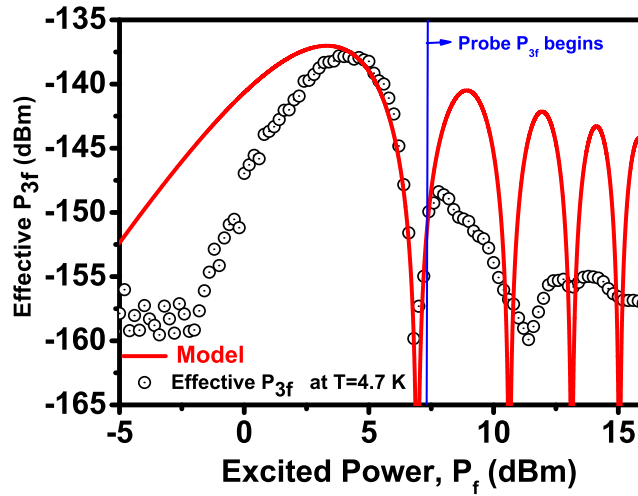
Fig. 6.13: Effective P_{3f} versus P_f for the bulk Nb sample measured by GT5 probe at 4.7 K under 5.025 GHz excitation as shown by the dot points. The solid line is the theoretical calculation based on the phase slip model of the Josephson junction. The parameters are as follows: T=4.7 K, Freqency=5.025 GHz, $R_n = 610\ \Omega$, $S = 3.0 * 10^{-14}\ m^2$, $a = 10\ nm$, N=1, $l_{gap} = 100\ nm$. Only R_n and S were varied to perform the fit. The vertical blue line shows where the probe background nonlinearity has been naively subtract from the data.

temperature dependent R_n and S is because the screening current loop will look for the easiest trajectory with highest critical current of the weak link Josephson junctions to pass through. A summary of the temperature dependent R_n and S from our model fits for the effective P_{3f} at different temperatures is shown in Fig. 6.14. One can see the R_n gradually goes up with decreasing temperature from 9 K to 6K. This is consistent with the decrease of quasi-particle density from high temperature to low temperature. Below 5.7 K, the normal resistance decreases with decreasing temperature. This decrease also corresponds to a decrease of the area S with decreasing temperature below 5.7 K. Halbritter has noted the existence of NbO_x material or proximity-coupled Nb in the vicinity of weak links in bulk Nb with reduced transition temperature of 5.1 K to 6.0K [51]. Although we don't know how to interpret this decrease at low temperature, several possible issues may be in play. For example, if there is a superconducting inhomogeneity with lower T_c than that of bulk Nb, R_n may suddenly change once the inhomogeneity become superconducting. This may explain the sudden rise of R_n at T=5.7 K. The localized heating of the probe at very low temperature may also be another possible reason for the non-monotonic dependence in Fig. 6.14. These possibilities may affect the screening current area S at low temperature and result in a corresponding change of R_n at low temperature.
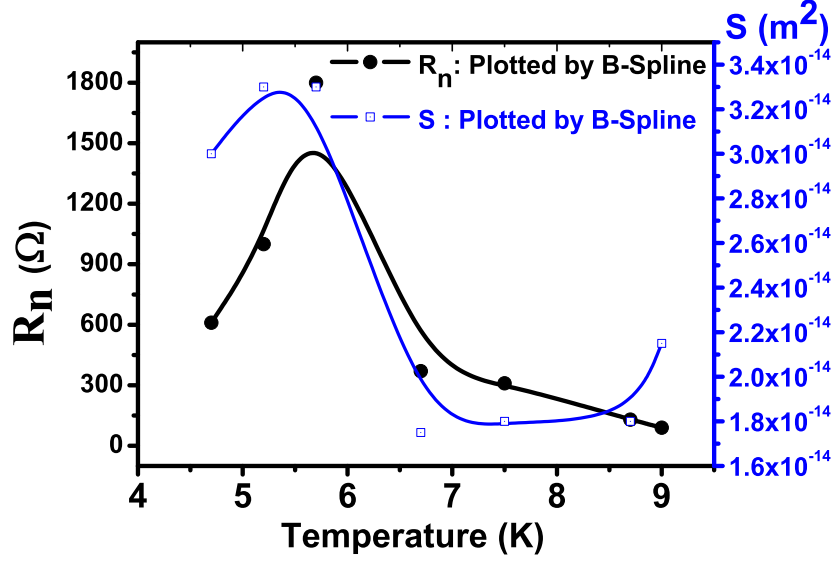
Fig. 6.14: Temperature dependent fitting parameters R_n (normal resistance of the junction) and S (area of the induced screening current loop). Each value is determined by the fitting method of the phase slip model from the P_{3f} versus P_f data in Fig. 5.21.

6.3 Nonlinearity coming from switching events

In addition to the nonlinear mechanisms discussed above, another possible nonlinear mechanism is the switching between the Meissner state and the mixed state during the RF cycle. That is, while the peak value of the applied RF magnetic field is higher than the surface penetration field of the superconductor, the material will switch into the critical vortex state from the Meissner state. The difference between this and the switching model from moving vortices is that the switching model doesn't consider the details of the interaction between moving vortices inside the materials but only consider the corresponding change of reluctance of the write head between the Meissner state and vortex critical state of the superconductor in

one RF cycle. This process of switching between states implies another source of harmonic response.

Similar to the linear response modeling discussed in Chapter 4, one also can model the superconducting states switching with an equivalent magnetic circuit to describe the time dependent flux inside the superconductor underneath the magnetic write head probe, as shown in Fig.6.15. The inductively coupled driving line provides a magnetomotive force (V_m) to the yoke with a reluctance R_y. A magnetic flux Φ is channeled down along the yoke to the gap. There the flux can divided into two branches : one directly goes through the gap with a reluctance R_g and the other shunts into the superconductor with a reluctance R_{sc}. Note that the reluctance of the superconductor R_{sc} is a tunable reluctance. It is the combination of a reluctance R_s from the nonlinear Meissner state and a reluctance R_v from the vortex critical state. While the surface applied field $B(t)$ is smaller than the penetration field B_v, the reluctance will remain at the value of R_s. Once $B(t) > B_v$, an additional reluctance channel R_v is created.

While the superconductor is in the nonlinear Meissner state, the circuit analysis is the same as that in the linear response model discussed in Chapter 4. As in Eq. 4.3, the reluctance of the nonlinear Meissner state is given by

$$R_s = \frac{d_{yoke}}{\lambda(T)} R_g \qquad where \qquad R_g = \frac{l_g}{\mu_0 l_y d_{yoke}} \tag{6.22}$$

Note that all notations have the same definitions as discussed in Eq. 4.3. On the
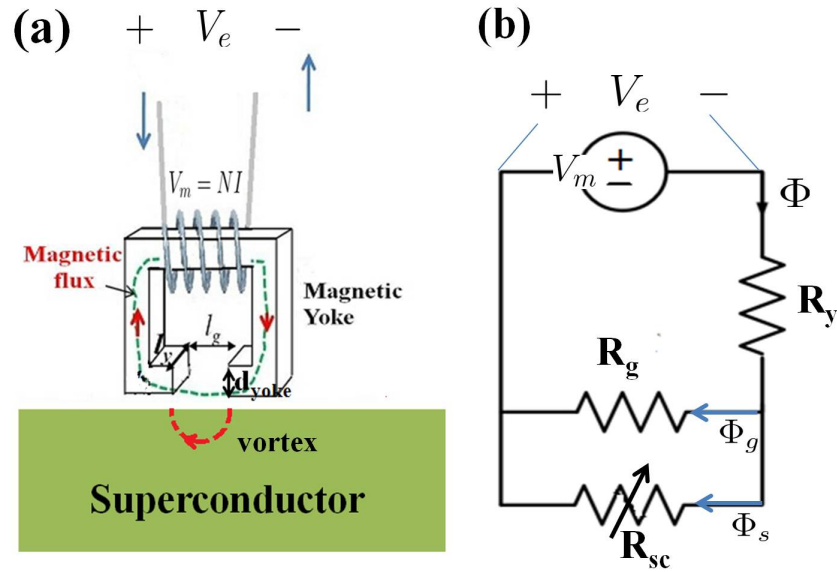
Fig. 6.15: (a) Schematic illustration that the magnetic flux coming from the yoke penetrates into the superconductor. Note that l_y, d_{yoke} and l_g represent the width, the thickness, and the length of the magnetic gap, respectively. (b) An equivalent magnetic circuit for the magnetic flux transport from the yoke to the superconductor. Note $R_{sc} = R_{sc}(R_s, R_v)$ is a time variable reluctance as a function of R_s and R_v, where R_s is the reluctance of the superconductor in the nonlinear Meissner state and R_v is the reluctance from the vortex critical state.

other hand, in the vortex critical state, we have the magnetomotive force as

$$\Phi_0 R_v = \int_{gap} H_0 dy = \frac{B_0 l_g}{\mu_0} \qquad \Phi_0 = B_0 \lambda^2 \qquad (6.23)$$

where Φ_0 is the flux quantum and the latter equation assumes that the vortex carries one unit of magnetic flux, which may not always be the case. Hence the reluctance of the vortex critical state is given

$$R_v = \frac{l_g}{\mu_0 \lambda^2} \qquad (6.24)$$

In addition to the nonlinearity of the penetration depth with RF field, we believe the transient variations between R_v and R_s will also induce a harmonic response which is measured in the experiment. This model in terms of $P_{3f}(T)$ and $P_{3f}(P_f)$ will be calculated in the future to see if this model produce anything different from Fig. 6.5.

6.4   Chapter 6 Conclusions

Three nonlinear models were discussed to interpret the measured nonlinearity on the bulk Nb. From the calculated nonlinearity, nonlinearity due to the mechanism of vortex generation and annihilation is simply not consistent with most of our measurements. Nonlinearity from the proposed switching events is not clearly related to the measured P_{3f}. Nonlinearity from the weak-link Josephson effect is the best model now to explain the measured nonlinear response on bulk Nb for

both $P_{3f}(T)$ and $P_{3f}(P_f)$ measurements. Therefore, the majority of the measured nonlinearity on bulk Nb comes from the mechanism of Josephson nonlinearity and Josephson vortices.

7. MAGNESIUM DIBORIDE NONLINEAR PROPERTIES INVESTIGATED UNDER LOCALIZED HIGH RF MAGNETIC FIELD EXCITATION

Preface of the Chapter

Due to the persistent problems of Nb surface issues in bulk Nb cavities, many alternative materials have been explored recently for application in Superconducting Radio Frequency (SRF) cavities. Materials such as Tri-Niobium Tin (Nb_3Sn) [1] and Magnesium Diboride (MgB_2) [99] have been examined. These compounds are easy to fabricate and their compound phases are stable over a broad composition range. However there are still many challenges to place either MgB_2 or Nb_3Sn into the SRF cavities applications. For example, uniformly coating these compounds on to the inner surface of large SRF cavity by existing deposition technology is not an easy processing task. For MgB_2, an H_{c1} value smaller than the thermodynamic critical field of traditional bulk Nb is also another issue. In this chapter, we will focus on MgB_2 to study it's nonlinear behavior and point out potential problems of MgB_2 in their application to SRF cavities.

7.1 Introduction

The discovery of superconductivity in MgB_2 in January 2001 [100] ignited enthusiasm and interest in exploring its material properties. Several remarkable features, for example a high transition temperature ($T_c \sim 40$ K), a high critical field, and a low RF surface resistance below T_c, shows great potential in several applications such as superconducting wires and magnets. The success of making high quality epitaxial MgB_2 thin films provides another promising application as an alternative material coating on superconducting radio frequency (SRF) cavities [101]. Over the past decade, the accelerating gradient of SRF cavities has achieved 59 MeV/m in fine-grain Niobium (Nb) single cell cavity [4]. In order to go further, new high T_c materials with low RF resistance are required for interior coating of bulk Nb (or Cu) cavities. High quality MgB_2 thin films may satisfy the demands for SRF coating materials because such films can avoid the weak link nonlinearity between grains, and lead to the possibility of making high-Q cavities that operate at high accelerating gradients [99].

However, there still exist mechanisms that produce non-ideal behavior at low temperatures under high RF magnetic fields, such as vortex nucleation and motion in the film [57]. In addition, due to the presence of the π band and σ superconducting bands, the intrinsic nonlinear response of MgB_2 at low temperature is large compared to single-gap s-wave superconductors [102] [103]. Finally, it has been proposed that MgB_2 has 6 nodes in its energy gap [104]. Intermodulation distortion (IMD) measurements show a strong enhancement at low temperature (T) as $P_{IMD}(T) \sim 1/T^2$

126

[105], similar to the characteristics of the nodal d-wave $YBa_2Cu_3O_{7-\delta}$ (YBCO) superconductor [63]. Note that the nodal nonlinear Meissner effect has only been measured by means of nonlinear microwave techniques up to this point. If MgB$_2$ is a nodal superconductor, the coating of MgB$_2$ on SRF cavities will limit the high-field screening response at low temperature and therefore degrade the performance of the SRF cavities. Based on the above concerns, the study of MgB$_2$ microwave nonlinear response in the high frequency region (usually several GHz in SRF applications) can reveal the dissipative and nondisipative nonlinear mechanisms and perhaps enable application of MgB$_2$ films as cavity coatings.

In our experiment the localized harmonic response of superconductors is excited by a GT5 magnetic write head probe. Based on the gap geometry of the magnetic write head probe, sub micron resolution is expected. We present our observation of the nonlinear response of high quality MgB$_2$ films below T_c. These films were grown on (0001) sapphire substrates by the hybrid physical-chemical vapor deposition technique (HPCVD) by collaborators at Temple University. A (0001)-oriented MgB$_2$ film with ($10\bar{1}0$) in-plane epitaxial structure was determined by θ-2θ and ϕ scans in X-ray diffraction, respectively. A detailed description of the growth technique and their structural analysis has been reported before [81].

It should be noted that the SRF cavities function at very low temperature and in RF magnetic fields of varying strength, depending on location in the cavity. However our microscope functions at temperatures down to 4.2 K, and with a localized high RF magnetic field. Therefore our microscope is best suited for finding the localized electromagnetic response of the surface. We expect to find electromagnetic

127

contrast due to surface defects in the materials making up the cavities. In this chapter, I report the MgB$_2$ experimental nonlinearity data from localized areas. These data will be interpreted as a combination of several nonlinear mechanisms including intrinsic nonlinear responses [103][104] and vortex nonlinearity [57].

7.2 Third Order Nonlinear Measurement Results

The experimental setup for amplitude and phase measurements of the superconductor harmonic response has been shown in Fig. 5.2 and Fig. 5.4 of Chapter 5. The measurement of the 3rd order harmonic power (P_{3f}) is performed near the center of several epitaxial MgB$_2$ films with the same thickness, 50 nm. The global T_c of these samples are around 32 K$\sim$35 K measured by the four point resistance method. These samples are all grown on sapphire substrates under the same deposition conditions by the HPCVD method. These samples can be grouped into two classes: Group A are the samples which are not well isolated from the ambient environment after growth. Group B are the samples which are kept in desiccated conditions immediately after deposition. At least two samples are measured from each group to examine their RF microwave properties. Fig. 7.1 shows a representative temperature dependent $P_{3f}(T)$ curve for the sample from group A at the excited frequency 5.33 GHz and excited power +14 dBm. Above 40 K a very small signal begins to arise above the noise floor of the spectrum analyzer. This P_{3f} is from the magnetic write head probe itself. We have measured the P_{3f} of the magnetic probe when it is placed on the surface of a bare sapphire substrate and in general

128
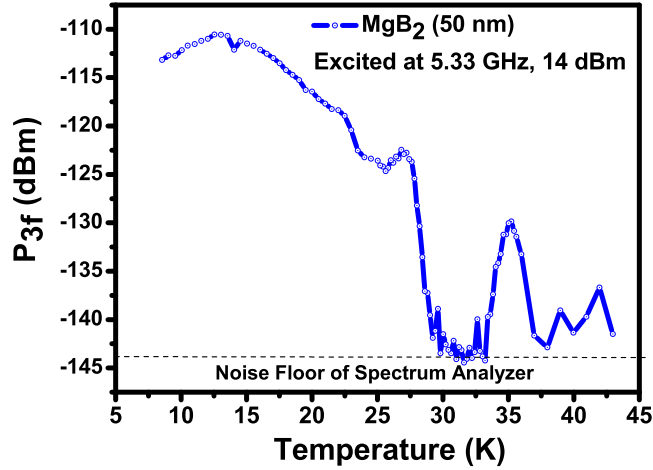
Fig. 7.1: Temperature dependence of 3rd harmonic power P_{3f} from a 50 nm thick MgB$_2$ of group A measured with an excited frequency of 5.33 GHz at +14 dBm.

this probe nonlinearity is negligible at excited powers under +14 dBm. Although excited powers above +14 dBm excites stronger nonlinearity from the probe, this nonlinearity is almost temperature independent in the Helium cooling temperature range. Therefore probe nonlinearity, if it is present, can be treated as a constant background signal above the noise floor of the spectrum analyzer/VNA. The mechanism of probe nonlinearity is the hysteretic behavior of the yoke material, and has been discussed previously [66].

From Fig. 7.1, a clear $P_{3f}(T)$ peak centered at 35 K shows up above the noise floor. This peak arises from the modulation of superconducting order parameter near T_c due to the enhanced sensitivity of superconducting properties as the superfluid density decreases to near-zero levels. This peak at T_c is also phenomenologically predicted by Ginzburg-Landau theory, and is similar to that discussed in the measurement of Nb thin film as shown in Fig. 5.9.

129

We also note the onset of a temperature dependent P_{3f} nonlinearity below 29 K, followed by a peak near 27 K, and then a gradually increasing P_{3f} down to 12.5 K. Finally, the P_{3f} decreases below 12.5 K.

Measurements of the dependence of P_{3f} on P_f are shown in Fig. 7.2 for the 50 nm thick MgB_2 film (group A) at some selected temperatures. In the normal state of MgB_2 (T=42K), the measured nonlinearity comes from the probe itself and shows a slope steeper than 3 at high excited power above +15 dBm. Near T_c, the slope is 2.74, close to the value of 3 predicted for the intrinsic nonlinear response [53]. Based in part on this evidence, we believe that in the high temperature region close to T_c, most of the P_{3f} comes from the intrinsic nonlinear mechanism related to the modulation of the order parameter near T_c. In the intermediate and low temperature regime, the slopes of P_{3f} vs. P_f are between 1~2. This value is similar to that predicted by many phenomenological models (between $1 \sim 2$) for YBCO films at low temperature [63] [106], implying that several possible nonlinear mechanisms are involved at low temperature for MgB_2 films. It should be noted that the low temperature nonlinearity can be easily excited at low power. Fig. 7.2 shows the P_{3f}-P_f slope evolution from an intrinsic nonlinear region around T_c to a regime with different behavior at lower temperature.

The representative curve of $P_{3f}(T)$ from a sample of group B is shown in Fig. 7.3. Compared with the measurement of $P_{3f}(T)$ from the sample of group A, as shown in Fig. 7.1, many temperature dependent nonlinear features are consistent and reproducible. From Fig. 7.3, the first peak at 32 K represents the first T_c of this sample. A second peak at 22.5 K, similar to that at 27 K (Fig. 7.1) is
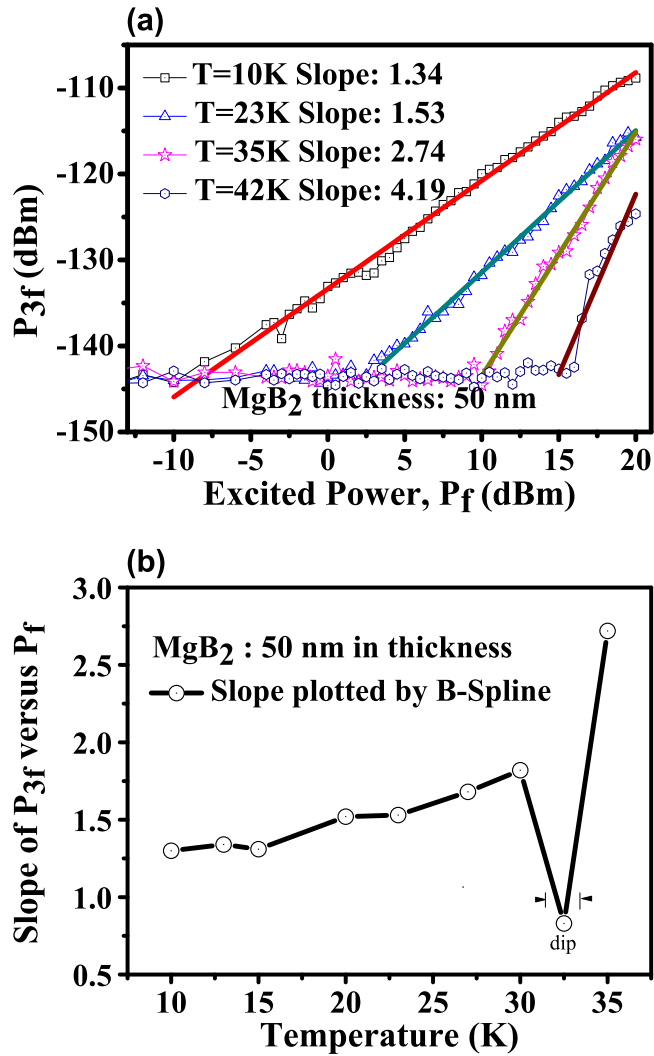
Fig. 7.2: (a) Measured power dependence of P_{3f} on P_f for the 50 nm thick MgB_2 film of group A. (b) Fitted slope at selected temperatures for the film of group A. The marked dip describes an almost nonlinearity-free region from the MgB_2 sample (see Fig. 7.1) and its small slope is likely due to the probe nonlinearity.

131
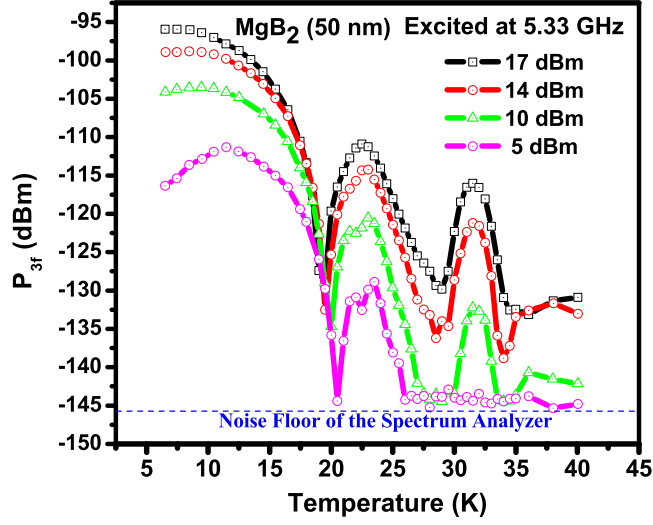
Fig. 7.3: Temperature dependence of 3rd harmonic power P_{3f} from a 50 nm thick MgB_2 film of group B measured with an excited frequency of 5.33 GHz at different excited powers.

distinctly visible in Fig. 7.3. The only difference is a second deep dip around 20 K for the sample from group B, versus a shallow dip at 25 K for the sample from group A in the $P_{3f}(T)$ measurement. The position of the dip and its depth also change with the excited power. This sharp dip indicates the near cancelation of all nonlinear mechanisms at this temperature. For both groups of samples, the nonlinearity gradually increases with reduced temperature below the second dip, followed by a saturation and finally a decrease at temperatures below 10 K, at least for lower excitation power.

Fig. 7.4 shows the dependence of P_{3f} on P_f for the sample from group B. At T_c (32 K), the slope of the power dependence is almost 3. Below T_c, the slope drops to a value between 1~2, the same as many published results on MgB_2 [78] [107], excluding the points near 20 K at which the slope drops below one. This point

132
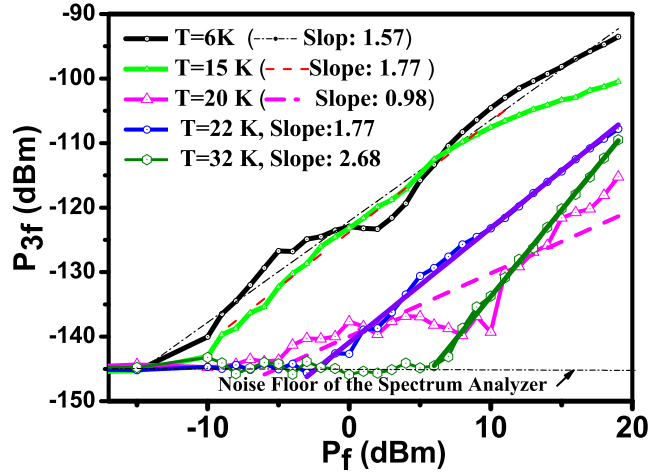
Fig. 7.4: Power dependence of P_{3f} on P_f for the 50 nm thick MgB$_2$ film of group B, taken at temperature of 6 K, 15 K, 20 K, 22 K, and 32 K.

(the second dip) shows very small nonlinearity from the superconductor below 10 dBm excitation. For high excitation power (above 10 dBm), the majority of the nonlinearity signal comes from the probe itself. In addition, at some temperatures (20 K, 15 K, 6 K), the power dependence curve shows several changes of slope. This implies that the nonlinear behavior is more complex at intermediate and low temperatures. Therefore based on the similar nonlinear behavior of many measured MgB$_2$ samples, we next discuss several possible mechanisms that may account for the basic common features of our experimental data.

7.3   Nonlinear Mechanisms of Magnesium Diboride

7.3.1   Intrinsic Nonlinearity of MgB$_2$ Around T_c

The modulation of the superconducting order parameter by the applied RF field generates nonlinearity. While the excitation field is much lower than the critical

field, nonlinearity will be generated due to the perturbation of the order parameter. This phenomenon is generally known as the nonlinear Meissner effect (NLME). When the excitation field approaches the critical field, the mechanism of intrinsic nonlinearity is still similar to the NLME and becomes more significant. For example, around T_c, this nonlinearity comes from the backflow of excited quasiparticles in a current-carrying superconductor, which results in an effective decrease of the superfluid density [103][104][108][109]. A two band quasiparticle backflow calculation has been applied to the MgB$_2$ intrinsic nonlinearity. Based on the work of Dahm and Scalapino[103], the temperature and induced current density dependent superfluid density $n_s(T, J)$ can be written as

$$\frac{n_s(T, J)}{n_s(T, 0)} = 1 - (\frac{J}{J_{NL}})^2; J_{NL} = \frac{J_{c,\pi}}{\sqrt{b_\pi(T) + b_\sigma(T)\frac{J_{c,\pi}^2}{J_{c,\sigma}^2}}} \tag{7.1}$$

where b$_\sigma$ and b$_\pi$ are the temperature dependent nonlinear coefficients for the σ band and π band, respectively, and their values are defined in reference [103]. Here $J_{c,\sigma} = 4.87 \times 10^8 A/cm^2$ and $J_{c,\pi} = 3.32 \times 10^8 A/cm^2$ are the pair-breaking current densities for the two bands. For a 50 nm thick MgB$_2$ thin film, the generated third harmonic power $P_{3f}(T)$ is estimated by substituting J_{NL} into Eq. 5.1 in Chapter 5. Here, the value of the geometry factor is estimated to be $8.3 * 10^5$ A^3/m^2, calculated from the Karlqvist equation for the magnetic field from a magnetic write gap under the assumption that the probe height is around 2 μm above the MgB$_2$ superconducting surface. The details about the calculation of $\Gamma(K_{RF})$ for the magnetic write head has been discussed in section 5.3.3. This geometry factor is a strong function of
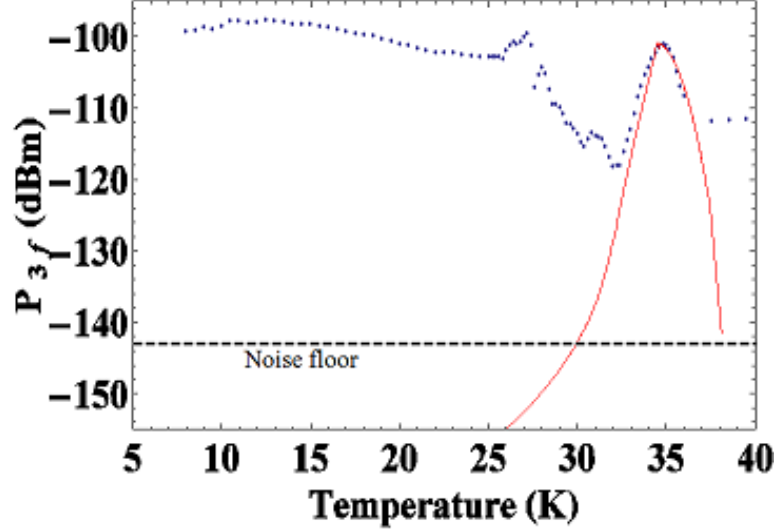
Fig. 7.5: The blue dots are the MgB$_2$ $P_{3f}(T)$ data at an excitation frequency of 5.33 GHz and excitation power of 18 dBm. The solid red line is the simulated result of the intrinsic nonlinearity from superconducting order parameter modulation near T_c of MgB$_2$ with thickness 50 nm under the assumption that the magnetic probe provides a field described by a geometry factor $\Gamma = 8.3 * 10^5$ A^3/m^2. Other parameters used in this calculation include $\lambda(0K)$= 100 nm, $J_{NL}(T \rightarrow 0K) \simeq 6.5*10^{12} A/m^2$, λ_{cutoff}= 800 nm, $J_{cutoff} = 4.2*10^{11}$ A/m^2 and T_c= 34.6 K with a standard deviation of Gaussian spread of δT_c= 1.3 K. The noise floor in the experiment is -143 dBm and the probe adds significant background nonlinearity in this case as well.

height and can lead to surface fields above the critical field of the superconductor [11] [12].

Finally, the $P_{3f}(T)$ calculated results from Eq. (5.1) for the 50 nm thick film at a 5.33 GHz excited frequency is shown as the solid red line in Fig. 7.5, assuming cutoff values for $\lambda(T \rightarrow T_c)$, $J_{NL}(T \rightarrow T_c)$, as well as a Gaussian distribution of T_c [53]. This intrinsic response has measurable values above the noise floor only in the high temperature region near T_c. The experimental data of the MgB$_2$ films from group A under a +18 dBm, 5.33 GHz microwave excitation is shown as blue dots. It is clear that this model predicts very low nonlinear response at low temperature. Hence other mechanisms must be responsible for $P_{3f}(T)$ at temperatures below T_c.

7.3.2 Nonlinearity Due to Second T_c with Leggett Mode at Low Temperature

Theoretically, the nonlinear response of a two-band superconductor should show a strong peak at the second T_c for completely decoupled bands [108]. With increasing interband coupling, the peak due to the second T_c will gradually shift to higher temperature and have a reduced peak value [108]. Therefore based on theory, it is possible that in addition to the nonlinearity coming from the first T_c, a proximity enhanced second T_c also contributes to the intrinsic nonlinearity. From the $P_{3f}(T)$ data shown in Fig. 7.1 and Fig. 7.3, the second peak at 27 K (Fig. 7.1) or at 23 K (Fig. 7.3) may be due to this intrinsic mechanism. Another $P_{3f}(T)$ experiment was carried out with a loop probe which utilizes a smaller RF magnetic field and a large excitation area. The loop probe, providing an almost 1 mT in-plane magnetic field on the MgB_2 surface, is made of a nonmagnetic coaxial cable with its inner conductor (200 μm in diameter) forming a $\sim$500 μm outer-diameter semicircular loop shorted with the outer conductor [10] [11]. This measurement is performed on the MgB_2 sample from group A and the loop probe is positioned on the same region of the sample where the magnetic write head probe was placed. In order to compare to the result measured by the magnetic write head probe, both $P_{3f}(T)$ curves are lined up to -100 dBm at their peaks around 27 K, as shown in Fig. 7.6. The loop probe measurement shows only one peak at 27.8 K almost the same temperature as the second peak measured by the magnetic write head probe. The lack of a peak at the first T_c for the loop probe measurement is due to the weak magnetic field and therefore a small value of Γ in Eq. 5.1 at the highest T_c. The inset of Fig. 7.6

shows the power dependence of P_{3f} on P_f measured by the loop probe at the peak temperature. The slope of P_{3f} on P_f is 2.85, very close to 3, the theoretical value for the intrinsic nonlinear Meissner effect. However, the slope of P_{3f} on P_f obtained with the magnetic write head probe at this temperature is just 1.68. This implies that our magnetic write head probe excites another nonlinear mechanism in this temperature region and there is interference with the nonlinearity from the second T_c. The magnetic write head probe provides more intense and localized parallel magnetic fields on the superconductor sample surface. A comparison of magnetic fields generated by the magnetic write head probe and the loop probe are reported in Ref. [66]. It is unclear why the nonlinearity from the proximity-enhanced second T_c is more significant than that from the first T_c in the loop probe measurement.

Besides the intrinsic nonlinearity from the proximity-enhanced second T_c, an additional intrinsic nonlinearity arising from Josephson coupling between the σ and π bands would be expected [110] below the second peak at 27 K in Fig. 7.1 or at 23 K in Fig. 7.3. This nonlinear response (arising from the Leggett mode) comes from the variable phase difference of the superconducting order parameters in the two bands of MgB_2, and will only be excited when a nonequilibrium charge imbalance appears both at short length scales and at temperatures where the proximity-induced π band becomes superconducting [110]. In our magnetic write head experiment, the perpendicular component of the RF magnetic field results in a charge imbalance and excitation of the Leggett mode would be expected. From the experimental data of $P_{3f}(T)$ in Fig. 7.1 and Fig. 7.3, the nonlinearity below the second peak gradually increases with decreasing temperature before saturation. In this temperature

137
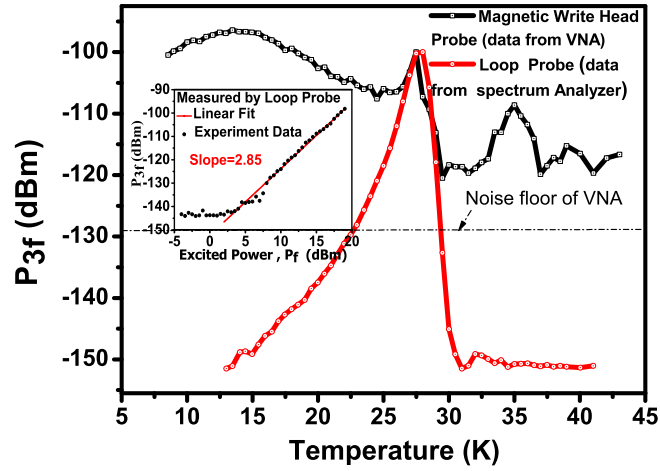
Fig. 7.6: Temperature dependence of P_{3f} from a 50 nm thick MgB_2 film (group A) measured by the loop probe (red curve), and magnetic write head probe (black curve), respectively. Both curves was shifted vertically to line up to -100 dBm at their peak around 27 K. The excited frequency for both measurement is 5.33 GHz. The excited power is 20 dBm and 14 dBm for loop probe and magnetic write head probe, respectively. Note that the VNA is used to perform the measurement with the write head probe and the spectrum analyzer is used in the measurement done by the loop probe. The VNA has higher noise floor $\sim$ -130 dBm. The inset shows the P_{3f} vs P_f dependence for the loop probe measurement at 27.8 K.

regime, the nonlinearity could arise from the Leggett mode mechanism, although no calculation of this nonlinearity exists, to my knowledge. However the observed temperature dependence of $P_{3f}(T)$ is reminiscent of that arising from Josephson weak links [87] or Josephson vortices in a large Josephson junction [11] [12] (see Fig. 6.11 for example). The absence of this signal in the macroscopic loop probe measurement is consistent with the charge imbalance mechanism.

7.3.3 Nonlinearity From the Reported Nodal Gap Symmetry

Although MgB$_2$ is commonly believed to be a conventional s-wave supercon-ductor, Agassi, Oates and Moeckly claim that MgB$_2$ has line nodes in the supercon-ducting gap, and they claim further that the gap has 6 nodes as, $\Delta(\phi,T)=\Delta_0(T)*\sin(6\phi)$ where ϕ is the azimuthal angle in the $\widehat{ab}$ plane of the hexagonal crystal, and $\Delta_0(T)$ is the weakly temperature dependent amplitude of the gap function at low tem-peratures [104]. From their IMD measurement on MgB$_2$ films, the temperature dependent $P_{IMD}(T)$ shows an upturn around $T < 10K$ and increases as $1/T^2$ [63]. Therefore, based on these observations and proposals, we would also expect our mea-surement of $P_{3f}(T)$ to show an increase in the same temperature range. However all of our experimental data show that $P_{3f}(T)$ tends to decrease at temperatures $T < 13K$. If the prediction of the nodal gap symmetry is correct, the observed downturn may be due to the interference between the Leggett mode nonlinearity (or some other nonlinearity) and the nonlinearity from this nodal gap behavior. An-other possibility may be that the RF magnetic fields employed in our experiment are too strong, or the temperatures are not sufficiently small to see the intrinsic

NLME due to the nodes. Yet another possibility is the nonlinear response of Andreev bound states, arising from a sign change of the superconducting gap, on the surface of MgB_2 [41] [112]. Further investigation at lower temperature and lower power is required.

7.3.4   Nonlinearity From Moving Vortices

Vortex nucleation and penetration into the film induces a dynamic instability and generates harmonic response [111]. Considering the relation of the penetration depth of MgB_2 ($\lambda \sim$140 nm at 0K) and our film thickness (50 nm), the tendency to create a straight vortex parallel to the film surface will be suppressed. However due to the magnetic field distribution from the magnetic write-head probe, a significant vertical component of magnetic field is expected. Fig. 7.7 shows a schematic illustration of our experiment in which the RF magnetic field from the magnetic write head probe interacts with the superconductor underneath the probe. A vortex and an antivortex nucleate perpendicular to the film and will move under the influence of the RF screening currents. One can model this situation with an equivalent point magnetic dipole that is horizontally-oriented and placed above the superconducting thin film [48]. The creation, motion and destruction of perpendicular vortex and antivortex pairs will generate high order harmonic response in the experiment. The nonlinear measurements in films from group A and group B would have nonlinearity from moving vortices in the entire temperature region under high RF magnetic field. In addition, vortex nonlinearity due to weak link coupling between each grain under the localized RF field (discussed in Section 6.2) may be another mechanism.

140

The nonlinearity from weak link vortices in a YBCO bi-crystal grain boundary has demonstrated a significant increasing nonlinearity with decreasing temperature following the temperature dependence of the critical current of the junction [11] [12]. From the $P_{3f}(T)$ measurement of MgB$_2$ in Fig. 7.1 and Fig. 7.3, the trends of temperature dependent nonlinearity below 30 K are very similar to the nonlinearity from the weak link vortices in a YBCO granular structure, except for the deep dip around 20 K in Fig. 7.3. Comparing the films of group A to that of group B, both Abrikosov vortex nonlinearity and weak link vortex nonlinearity of the films from group A would be expected to be more significant due to the exposure to air, which will degrade the film and therefore decrease the lower critical field of the weak links and grains. Models based on the creation and annihilation of perpendicular vortices and the weak link vortices would be applied to quantitatively analyze the MgB$_2$ data in the future.

7.4   Chapter 7 Conclusions

A strongly temperature-dependent third harmonic response is found from near field microwave microscopy measurements on high quality MgB$_2$ films. From the investigation of the third harmonic response as a function of temperature and input power level, the nonlinear mechanisms in high quality MgB$_2$ films appears to be quite complex. The nonlinear response near T_c can be well understood by a model relating modulation of the superconducting order parameter near T_c. However the nonlinear response at temperature less than T_c have several different possible nonlinear mech-
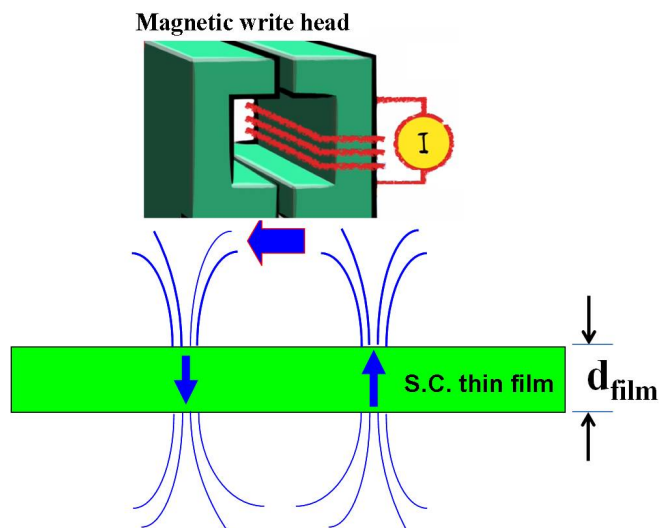
Fig. 7.7: Schematic illustration of the magnetic flux coming from the yoke of the magnetic write head to the superconducting thin film. This situation can be analogous to a magnetic dipole on the top of superconducting thin film (horizontal blue arrow). A vortex and antivortex perpendicular to the film tends to form if the film thickness $d_{film} \ll \lambda$. Figure not to scale.

anisms. The first is the intrinsic nonlinearity from the proximity-induced second T_c. The second is the intrinsic nonlinearity arising from Josephson coupling between the σ and π bands. The third is the potential nonlinearity from the proposed nodal gap symmetry of MgB_2. Finally is the nonlinearity due to the perpendicular vortex pairs as well as the inevitable weak link vortices created in the MgB_2 films by the high RF field probe.

8. FUTURE WORK

Overview of the Chapter

A number of projects were started during the course of this research, but not completed. These projects are important for the future utilization of my microwave microscope.

8.1   *Design of the Scanning System and P_{3f} imaging of bulk Nb*

defects

In our current work, an image of the nonlinear properties of bulk Nb superconductor is the final goal we want to achieve with our home-made high frequency RF magnetic field microscope. For scanning measurements with our current Desert Cryogenics tabletop cryogenic probe station, we refer to the design from the Prof. K. Moler group at Stanford University [113]. In their design, the probe is mounted to a high precision x-y-z stage and each axis is independently driven by mechanical motors as shown in Fig. 8.1. All of the motors are from the Orientalmotor Corporation : CRK Series 5-phase stepping motor unit. Due to the different required torque of the motion stage on each axis, each axis uses a different model of motor.

The model of the x-axis motor is the PK546PMA-R28L with a CRF507-KP driver and a built-in controller inside the driver. The y-axis motor uses model PK544PMA with the same driver as the x-axis. For the z-axis, a model PK523PMB motor is used with a CRD503-KP driver and a built-in controller. Each motor takes 1000 full steps per revolution of its shaft to produce 0.5 mm linear translation on the micrometer. As a result, the single step size of each mechanical motor is 0.5 μm. In order to further minimize the step size, an 80-tooth worm gear with incorporated antibacklash springs (Part ♯: AWFB83-D80 from W. M. Berg Inc.) is mounted to the end of the micrometer via the flexible coupling as shown in the inset of Fig. 8.1 on the z-axis. A double-thread worm screw (Part ♯: WFS-5D from W. M. Berg Inc.) is attached to the motor to turn the worm gear. Through the worm gear, one full step of the motor can produce a 50 nm linear translation. For the x-axis, a similar design is also involved to achieve a 50 nm linear translation per step of the motor. For the current y-axis, the motor directly rotates the micrometer with a corresponding 500 nm linear translation per step of the motor. A design of a worm gear on the y-axis can also be implemented in the future. The scanning system is controlled by a computer through motor drivers with built-in controllers. The setup for the drivers, power supplies, and controllers can be found in Appendix A.1.

A fixed point measurement of P_{3f} using the setup of Fig. 5.2 is performed before a raster scan to determine the excitation frequency and power. Then a raster scan in the x-y plane can be performed with the slider in physical contact with the superconductor surface. A preliminary raster scan experiment of the third harmonic image as a function of position is performed at T=15 K under 5.33 GHz
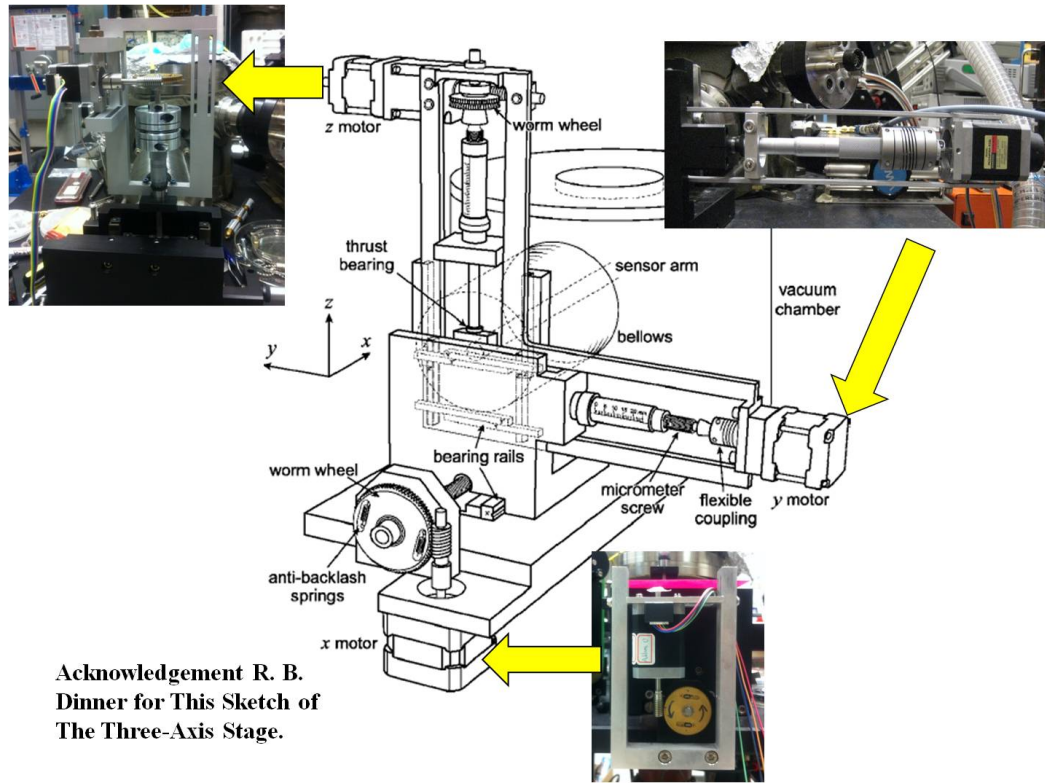
Fig. 8.1: Sketch of the three-axis stage that moves the magnetic write head probe arm [113]. Our current implementation of the scanning system for each axis is pictured in the three insets. Stepper motors mounted on the frames drive micrometer screws to generate linear motion. For the x and z axis, worm gears can achieve a minimum linear translation down to 50 nm per step of the motors. For the y axis, the motor is directly coupled to the micrometer screw and creates a 500 nm minimum linear translation per step.

and 16 dBm microwave excitation by the GT5 probe on a high quality MgB$_2$ sample with thickness 200 nm. The scan direction is along the y-axis micrometer first, and then the probe traces back to the beginning point, and an increase by one step in the x-axis micrometer is made without lifting the probe. The step sizes for both x-axis and y-axis motors are 10 μm in this raster scan. Fig. 8.2 (a) and Fig. 8.2 (b) show the P_{3f} image and the relative phase of $V_{3f}^{MgB_2}(T)/V_{3f}^{ref}$ on this 200 nm thick MgB$_2$ sample, respectively. The P_{3f} contrast shows stronger harmonic signal at the right part of the image but the difference of the position-dependent P_{3f} is small, roughly 1 dB. We think this contrast in P_{3f} is mainly due to the uncontrolled height of the write head in contact mode. The relative phase mapping shows a big contrast and we have confirmed this phase contrast is due to the mechanical movement of the flexible coax cable during the raster scan by changing the scanning direction. From this preliminary result, we realize that there are many improvements required to prepare a reliable raster scan image of P_{3f} on the bulk Nb sample in the future.

8.1.1   Probe/Sample Height Control

In addition, we know that the z separation of probe and sample will affect the magnitude of RF magnetic field on the sample surface. From Fig. 5.6 and 5.11, one can see the P_{3f} response from the tested superconductor is significantly dependent on the probe height and the geometry factor Γ also decays significantly with the increasing probe height. Therefore, the need for controlling the slider height and the magnitude of the field at the sample surface is very important during the scanning. A tapping mode design utilizing the piezoelectric quartz tuning fork to

146
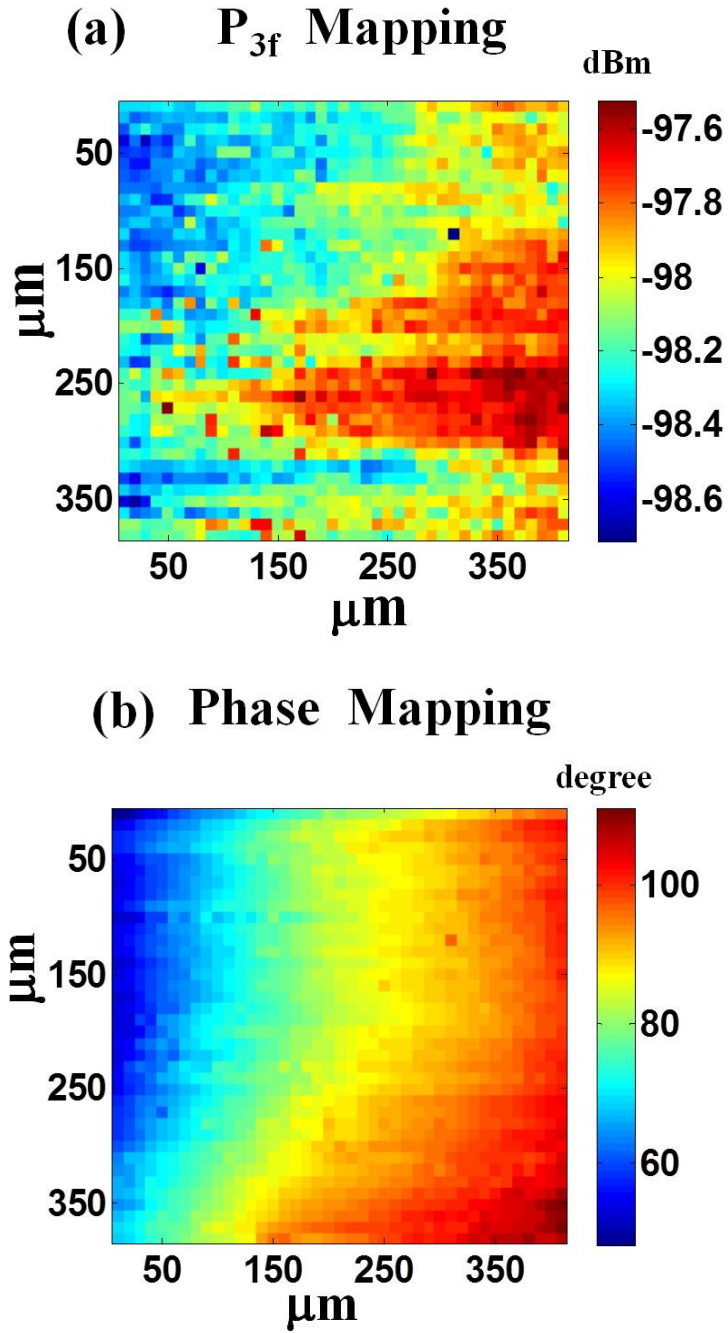
Fig. 8.2: (a) A P_{3f} image on high quality MgB$_2$ with thickness 200 nm. (b) A relative phase image of $V_{3f}^{MgB_2}(T)/V_{3f}^{ref}$. Both images are taken simultaneously at T=15 K under 5.33 GHz and 16 dBm microwave excitation. Each pixel corresponds to a 10 μm by 10 μm square area.

precisely control the probe height is widely used for tip-on-chip microscopy [114] [115]. Therefore, we propose to mount the magnetic write head probe onto a quartz turning fork. A Hall probe sensor of similar dimensions to our slider has been successfully mounted to a tuning fork [116]. Fig. 8.3 shows my new probe stage design to combine the write head probe and turning fork together. Two SMA hex connectors will be used to connect signal to the turning fork and the magnetic probe through wiring. The tuning fork can be driven by an audio wave form generator at a resonant frequency of the loaded tuning fork. While the probe approaches the sample, the resonant frequency of the tuning fork will shift. The value of the frequency shift (Δf) depends on the spacing between the sample and probe. An electronic system (either an oscilloscope or lock-in amplifier) measures the frequency shift of this signal and sends it to a feedback controller. The controller keeps the $\triangle f$ constant during the entire raster scan, ensuring a constant height above the surface. This height can be kept in the range of 100 nm or less, preserving most of our spatial resolution. By upgrading our existing scanning system, a high resolution P_{3f} image on Nb sample will be expected.

8.2 Experimentally measure the RF field experienced by the sample surface and determine the spatial resolution

With the capability of precision control of the probe height in our system, we then need to accurately estimate the field on the superconductor samples for any specific height of the probe. In addition, because the relative permeability (μ_r) of the
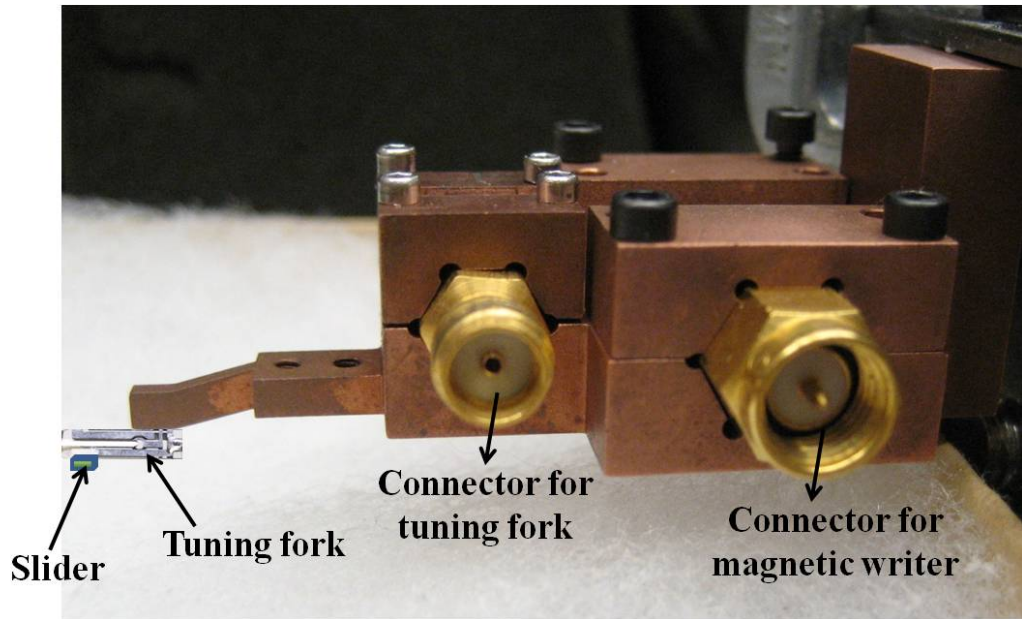
Fig. 8.3: A completed new probe stage which can hold two SMA connectors to connect wiring to the tuning fork and the magnetic write head individually. The magnetic write head is on the front edge of the slider body (far left in the picture.
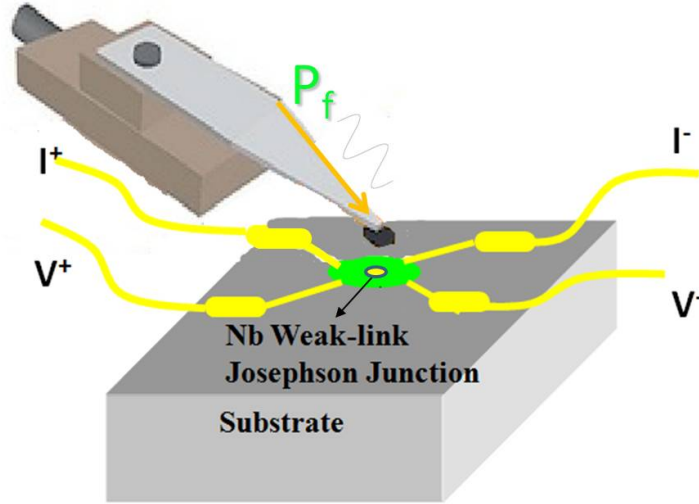
Fig. 8.4: A schematic illustration of experimentally measuring the RF field coming from the magnetic write head probe. The sample is a Nb weak link Josephson junction and an I-V measurement is performed while shining a RF magnetic field from the magnetic write head probe.

yoke materials (usually permalloy/ferrite) is dependent on frequency, a frequency dependence of the emanating fields from the write head probe is expected. Our idea is to put the probe on the top of a superconductor-constriction-superconductor (SCS) junction as schematically shown in Fig.8.4.

The SCS junction is fabricated by e-beam lithography on PMMA e-beam-resist to define the size of the SCS junction. After developing, Nb is sputtered onto the e-beam-resist pattern, followed by lift-off. The gold contacts are also fabricated by the method of photolithography before fabrication of the SCS junction. A finished SCS junction fabricated in this manner is shown in Fig. 8.5 (a) and the center constriction bridge is highlighted in Fig. 8.5 (b). By shining different values of the RF magnetic field on to this junction with our write head, we would expect to see an output response in the form of Shapiro steps [117] in the I-V curve of the
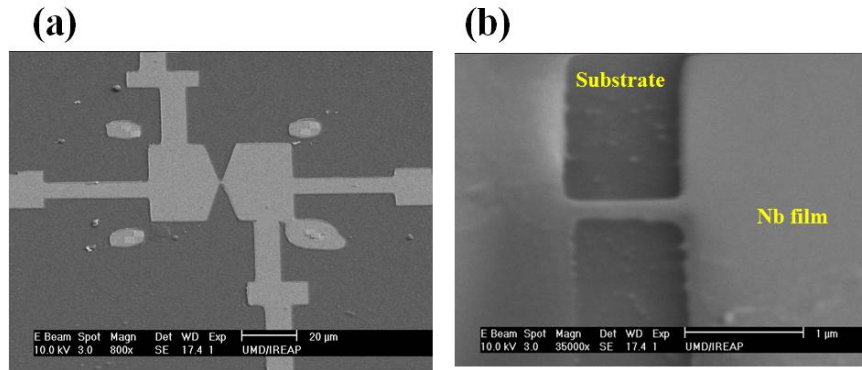
Fig. 8.5: (a) A SEM image of the Nb weak link Josephson junction. (b) A zoom-in region from the center constriction bridge. Note the width of the constriction bridge is 100 nm and the length is 1 μm.

junction. From the step height and their modulation with RF field level, we can get the absolute magnitude of the applied RF field on the sample surface. By translating the write head over this sample, we can also estimate the field profile created by our probe while over a superconducting sample. The method will also let us understand the difference of the field configuration between the longitudinal recording probe (GT5 Probe) and the perpendicular recording probe (Pinnacle Probe).

In order to understand what the spatial resolution of the near field magnetic microwave microscope will be, a sample with defects of known size, situated at known locations, is required. Tantalum (Ta) is one of the major foreign elements in the form of Ta clusters on the surface of Nb cavities due to the nearly identical chemical properties of Ta and Nb [118]. Hence I created a standard defect sample by embedding Ta thin film in a Nb thin film. The procedure to fabricate a column and a row of Ta inclusions in the shape of a cross pattern is shown in detail in Fig. 8.6. An atomic force microscopy (AFM) topography image of this finished sample
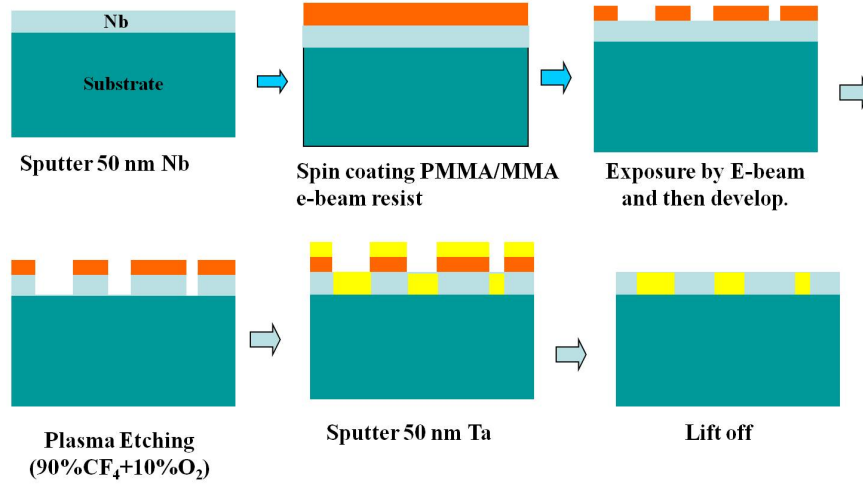
Fig. 8.6: Lithography procedure for fabricating sub-micron scale Tantalum (Ta) inclusions on the surface of Nb. Electron beam lithography was used in one step to develop patterns with different sizes of square shapes on in the e-beam resist (PMMA/MMA) and then followed by plasma etching of the Nb thin film. After this, Ta was deposited by sputtering, followed by lift-off to get rid of the e-beam resist.

is shown in Fig. 8.7 (a). The AFM image shows that shows the Ta inclusions are higher than the surface of the Nb thin film. A Laser Scanning Microscopy (LSM) reflectivity image for this Ta inclusion sample is also shown in Fig. 8.7 (b). The imaging technique of LSM reflectivity can be found in references [112] [120] and Fig. 8.7 (b) shows the reflected intensity of the laser beam with wavelength 405 nm. Note that this image is taken at ambient temperature and pressure. The reflectivity of Ta is lower than that of Nb. This implies that the surface of the Ta inclusions has more roughness compared to the relatively flat plane of the Nb thin film. By performing raster scanning of the write head under Nb superconducting temperatures, we expect a P_{3f}^{sample} contrast due to these Tantalum inclusions on the flat Nb surface. The relation of defects and its corresponding microwave performance
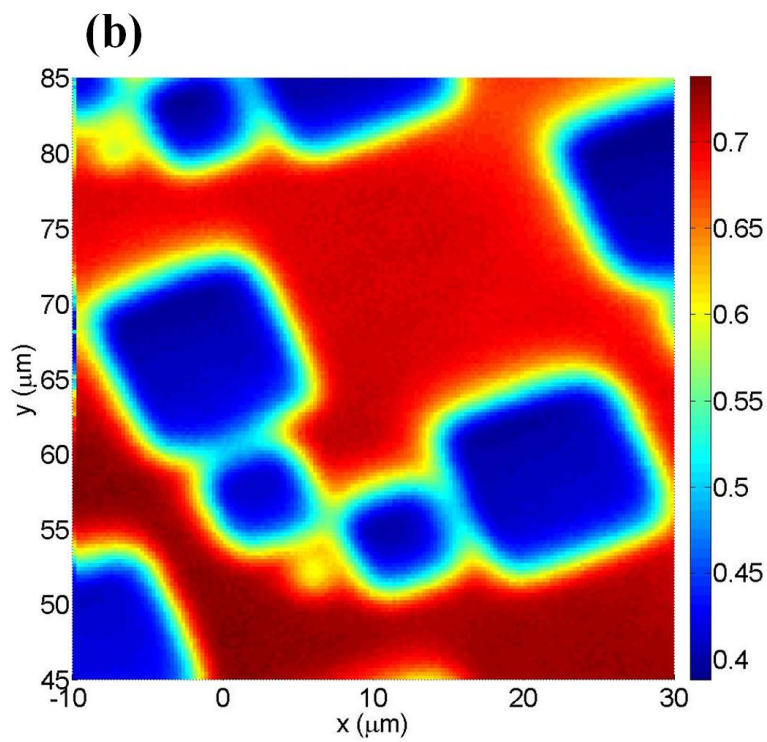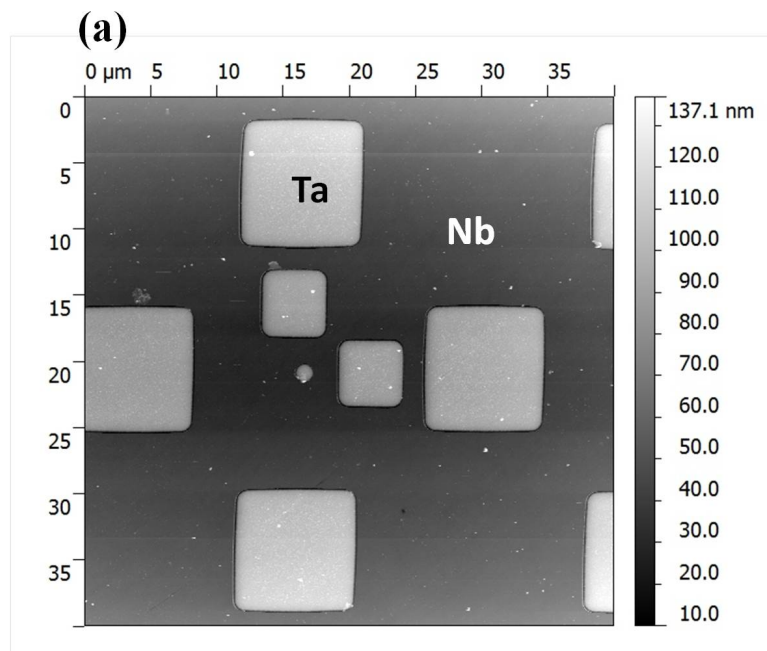
Fig. 8.7: (a)AFM topography image of the Ta inclusions embedded in Nb thin film with thickness 50 nm. (b) Laser scanning microscope reflectivity image of the Ta inclusions sample.

also can be quantitatively analyzed by the nonlinear models discussed in previous chapters.

8.3   Examination of New Physics Phenomena in Traditional and Novel Materials

Another motivation for building this localized and strong RF magnetic field near-field microscope is to explore theoretically predicted phenomena and discover novel physics in high T_c superconductors such as pnictides and traditional cuprate superconductors. For example, d-wave superconductors theoretically have a strong surface contribution to the nonlinear Meissner effect due to Andreev bound states at low temperatures [41]. We hope our near-field magnetic field microscope can experimentally demonstrate this surface phenomenon on d-wave cuprate superconductors in the future. For MgB_2, researchers recently predicted that its superconducting properties are intermediate between type-I and type-II superconductors due to its two Ginzburg-Landau κ values ($\kappa_\pi = \lambda_\pi(0)/\xi_\pi(0) = 0.66 \pm 0.02 < 1/\sqrt{2}$, and $\kappa_\sigma = \lambda_\sigma(0)/\xi_\sigma(0) = 3.68 > 1/\sqrt{2}$) [121]. The coexistence of both type-I and type-II characteristics leads to a special intervortex interaction [121]. We also expect to see similar dual behavior experimentally in a vortex critical state with our microwave microscope.

9. CONCLUSIONS

A magnetic write head is successfully integrated into the near-field magnetic microwave microscope operating at cryogenic temperatures and providing a localized strong rf magnetic field. Using this probe, a clear reproducible linear microwave response of superconductors can be measured on a sub-micron length scale. A model describing the linear response measurement is successfully constructed. This measurement and model can be applied to determine the penetration depth of new superconductors in the future.

For the nonlinear measurement, a third harmonic response signal from many superconducting samples (TBCCO, high quality MgB_2 films, Nb films and the bulk Nb sample) were obtained by the magnetic write head probe. Different superconductors present different nonlinear responses including an intrinsic Meissner nonlinearity and extrinsic nonlinearity. The bulk Nb measurement only shows extrinsic nonlinearity, consistent with the nonlinear mechanisms of Josephson junctions and Josephson vortices. In addition, nonlinearity coming from vortex generation and annihilation inside the material and the state switching between the Meissner state and the Abrikosov vortex critical state may also contribute a measurable nonlinear response in the P_{3f} measurement.

On the other hand, the measurements on Nb and MgB_2 thin films show not

only the extrinsic nonlinearity due to the vortex mechanism, but also intrinsic non-linearity. For extrinsic nonlinear mechanisms in thin films, nonlinearity due to the perpendicular vortex pair generation as well as the inevitable weak link vortices will be created by the high RF field probe in both Nb films and high quality MgB_2 films. However, the intrinsic nonlinearity of single-gap Nb and that of two-gap MgB_2 are completely different. Although both materials show a peak at T_c, which comes from the modulation of the superconducting order parameter near T_c, two-gap MgB_2 still has many intrinsic nonlinearity mechanisms. The first is the intrinsic nonlinearity from the proximity-induced second T_c. The second is the intrinsic nonlinearity arising from Josephson coupling between the σ and π bands . The third is the potential nonlinearity from the proposed nodal gap symmetry of MgB_2.

Future work will make use of topography sensitivity in the vortex critical state to get defect imaging on these type II superconductors, especially on bulk Nb. In addition, from the temperature dependence of the P_{3f} on bulk Nb measurement, we can approximately say the RF field coming from the magnetic write head probe can almost reach the thermodynamic critical field of Nb. A precise control of the height can allow for accurate control of the surface field applied on the superconductor and build a relationship between structural defects and electromagnetic imaging.

APPENDIX

A.1 Scanning System Drivers/Controllers Setup

The scanning system has been addressed in section 8.1. The detailed setup for the drivers and the cable connections will be addressed here. Most of the information and detailed functions of the step motor drivers can be found on the Orientalmotor web site (http://www.orientalmotor.com/). The manual can be downloaded from the Orientalmotor web site and an electric copy is also available on Prof. Anlage's Lab Wiki page. Here I only mention the functions I needed for building a raster scanning system.

The motors are 5-phase stepping motors and the drivers are CRK series drivers with built-in controllers. The 5-phase stepping motors offer high torque with low vibration. The drivers support I/O control and RS-485 communication. Figure A.1 shows the front of a driver with the top of the driver on the inset.

In my experiment, multi-axis mode is required to control three axes of the probe stage. Hence the SW2-No.2 switch on the three drivers should be switched to ON. The address number switch (SW1) is set to 0, 1, 2 respectively on the three drivers. The baud rate of all three drivers should be 9600 bps. The baud rate switches are SW2-No.1, SW2-No.2, SW2-No.3 and all baud rate switches should be at the OFF position to get a baud rate of 9600 bps.

Fig. A.2 shows the system configuration for three axes step motor units. The motor connector and encoder connector on drivers should connect to the step motors. The encoders can be mounted on double shaft step motors to enhance the precision in lateral translation. Each driver is powered by a 24 VDC power
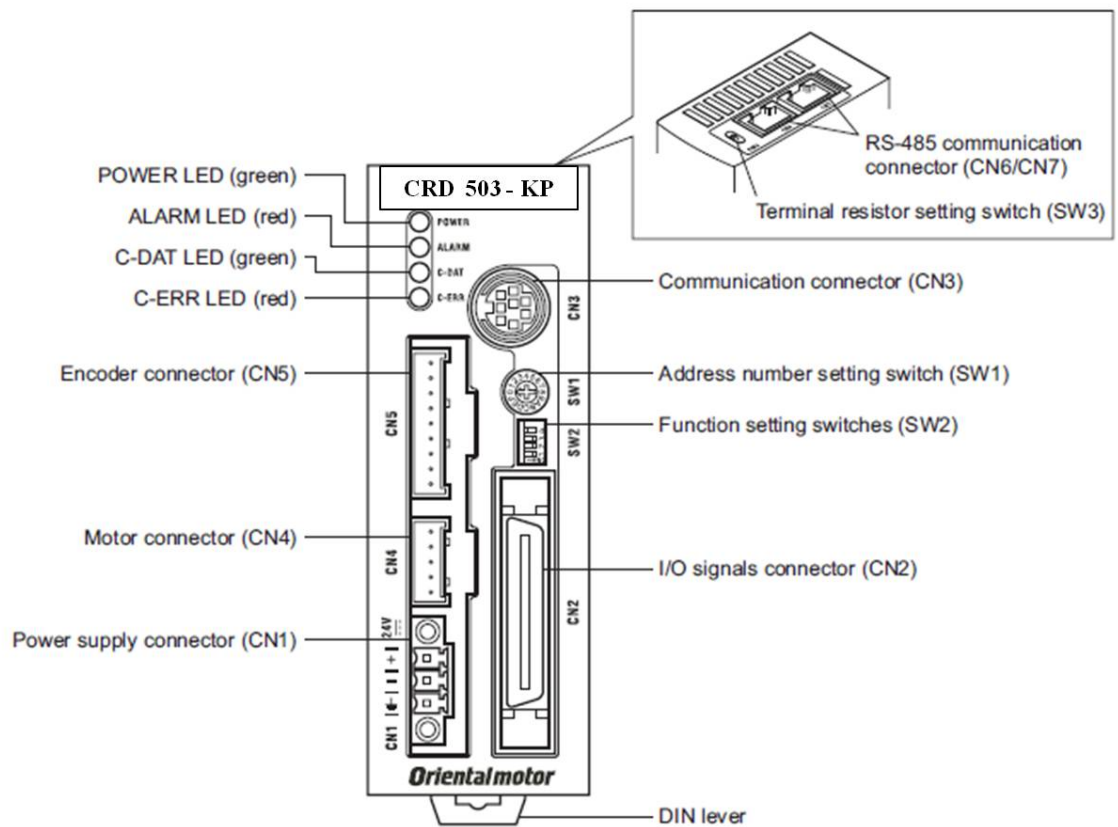
Fig. A.1: Front and top of the Orientalmotor CRK series motor driver with built-in controller. Note the top view can been seen in the inset.
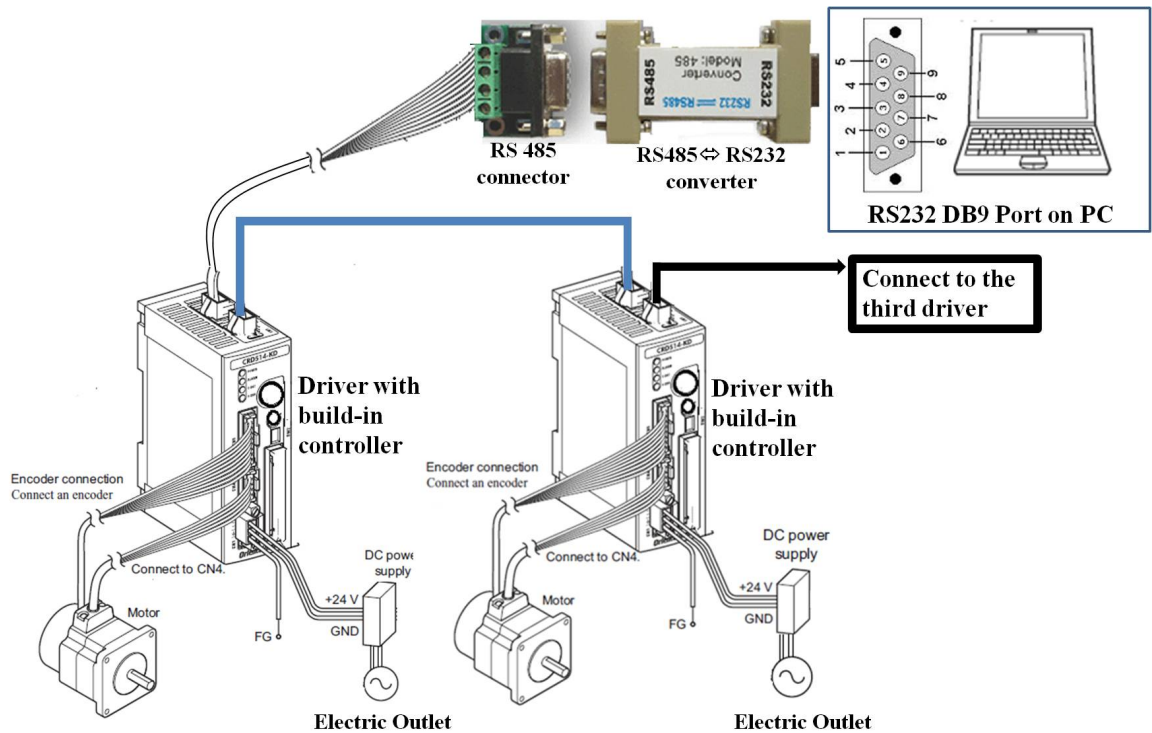
Fig. A.2: A configuration of setup for the step motor system for 3 axes stage translation.

supply, coming from a Mean Well Inc. DR-30 series DIN rail power supply. To communicate with three built-in controllers inside the drivers via a computer, the cat 5 ethernet cables are used to connect the drivers and the computer. Because the communication interface on the driver is RS-485, a RS-485 to RS-232 converter is used before connecting the cable to the DB9 port of the computer.

For this 5-phase stepping motor unit package, a free compiler is provided by Orientalmotor to operate the motor through the computer. In the manual, many ASCII commands are listed too. These ASCII commands are compatible with many assembler languages such as Java, C/C++ or Matlab, to compose a 2D raster scan program and perform the raster scan. In my experiment, I use Matlab to perform

160

the 2D rater scan on MgB$_2$ thin films. The Matlab code can be found on Prof. Anlage's Wiki page.

A.2 Data Acquisition methods for P_{3f} Nonlinearity Measurement

In this section, the detailed step by step procedure to get the P_{3f} signal from the bulk Nb sample will be addressed in detail. This procedure is applied to get P_{3f} responses from all superconducting materials we discussed in this thesis. The reason I use the bulk Nb measurement as an example is because getting P_{3f} responses from the bulk Nb sample is the most challenging one.

The first step is to rotate the micrometer on the z-axis to let the magnetic probe vertically approach the bulk Nb sample surface under vacuum and at cryogenic temperatures. The probe can gently contact with the bulk Nb surface to get the magnetic writer as close as possible to the sample surface.

The second step is to measure the S_{11} as a function of frequency using the linear response setup in Fig. 4.1. Fig. A.3 (a) shows the frequency dependent S_{11} on the bulk Nb sample. The S_{11} is measured at two selected temperatures, one is above the T_c and the other is below the T_c of the bulk Nb sample. One can clearly see the deepest resonance dip is around 4.5 GHz at this probe height for both curves. A slightly S_{11} amplitude difference at this dip for the two selected temperature measurements can be also identified from this figure.

After S_{11} measurement, I change the linear response setup to the P_{3f} measurement setup as shown in Fig. 5.2. Then the third step is to measure the P_{3f} as a

161
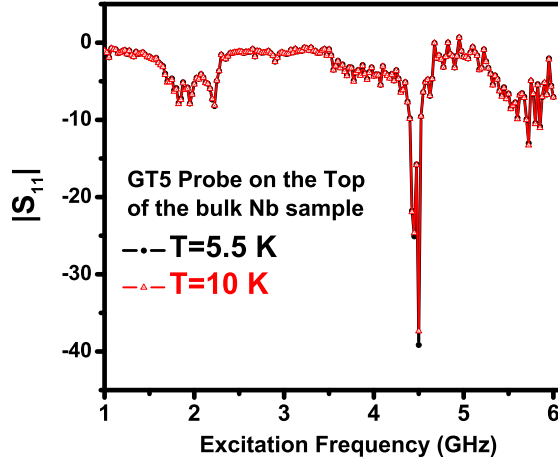
Fig. A.3: Frequency dependence of $|S_{11}|$ in dB measured at two different temperatures by the GT5 probe on the bulk Nb sample.

function of incident frequency around the deepest resonant dip at the two selected temperatures. I use the microwave synthesizer to sweep the incident frequency (f) and phase lock the third harmonic (3f) measurement by the spectrum analyzer with only 2 ∼ 3 averages of the signal to save liquid helium during the measurement. A 100 Hz span centered at the locked 3f frequency and 100 points in this 100 Hz span are also used for the data acquisition on the spectrum analyzer. Fig. A.4 (a) is the measurement result of P_{3f} as a function of stimulus frequency at two selected temperatures and the same excitation power (-13 dBm) on the bulk Nb sample. Taking the difference between the two curves and defining this new curve as an enhanced P_{3f} due to the contribution of the nonlinearity from the superconductive sample is shown in Fig. A.4 (b). One can see the peak is at the frequency 4.475 GHz, indicating a 16 dB enhancement.
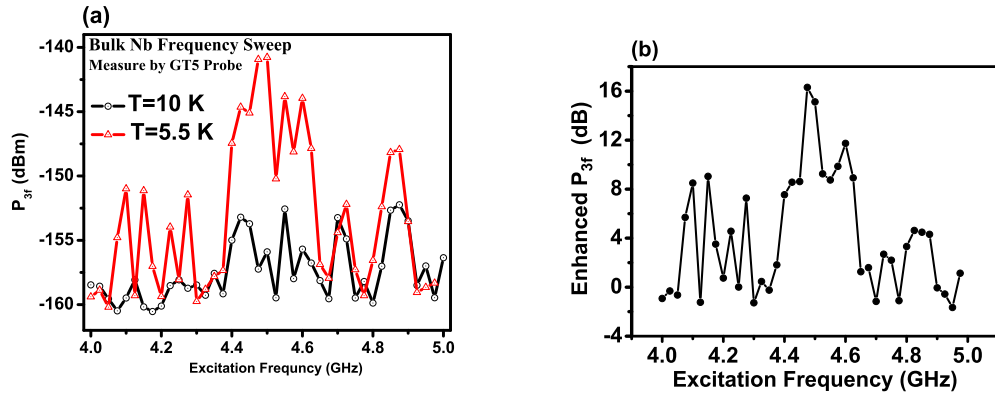
Fig. A.4: (a) Excitation Frequency dependence of P_{3f} measured at two different temperatures by the GT5 probe on the bulk Nb sample. The excitation power of the microwave synthesizer is -13 dBm for both curves. Note that the data is taken by sweeping the fundamental frequency of the microwave synthesizer and phase-locking the third harmonic frequency of the spectrum analyzer with $2 \sim 3$ time averaging to reduce the noise floor in the 100 Hz span. (b) The difference of two P_{3f} measurements at different temperatures from Fig. A.4 (a).

Finally, I slightly change the probe height again and use the slider on the write head probe to slide the probe assembly back and forth on the bulk Nb sample surface. I then repeat step 2 to find out the new resonant frequency at the new height. I repeat step 3 to look for where the best excitation frequency is. I then check if the P_{3f} enhancement at this excitation frequency is higher than that at the previous height. I repeat step 2 and step 3 again and again until the maximum enhancement is achieved. It usually takes 2 to 3 hours to find a good P_{3f} signal from the tested superconductor.

BIBLIOGRAPHY

[1] Eric Hand, "Can Tri-niobium Tin Shrink Accelerators," Nature **456**, 555, (2008).

[2] H. A. Schwettman, J.P. Turneaure and W.M. Fairbank, T.I Smith, M.S. McAshan, F.B. Wilson, E.E Chamber, "Low Temperature Aspects of a Cryogenic Accelerator," IEEE Transaction on Nuclear Science **14**, (3), 336, PAC (1967).

[3] Hasan Padamsee, Jens Knobloch, Tomas Hays "RF Superconductivities on Accelerators (Wiley Series in Beam Physics and Accelerator Technology), Chapter 13," ISBN: 978-3-527-40842-9, (1998).

[4] R. L. Geng, G.V. Eremeev, H. Padamsee, and V. D. Shemelin, "High Gradient Studies for ILC With Single-cell Re-entrant Shape and Elliptical Shape Cavities Made of Fine-Grain and Large-Grain Niobium," in Proceedings of the 2007 Particle Accelerator Conference, Albuquerque, New Mexico (IEEE, New York, 2007), p. 2337.

[5] Claire Antoine, "SRF issues about materials and surfaces," SRF-2011 tutorials, Argonne National Lab. `https://twindico.hep.anl.gov/indico/conferenceOtherViews.py?view=standard&confId=631`

[6] Hasan Padamsee, Jens Knobloch, Tomas Hays, "RF superconductivities on Accelerators (Wiley Series in Beam Physics and Accelerator Technology), Chapter 21," ISBN: 978-3-527-40842-9, (1998).

[7] `http://www.linearcollider.org/ILC`

[8] Y. Iwashita, Y. Tajiro, H. Hayano, "Development of high resolution camera for observations of superconducting cavities," Phys. Rev. ST Accel. Beams **11**, 093501, (2008).

[9] S. M. Anlage, V. V. Talanov, A. R. Schwartz, "Principles of Near-Field Microwave Microscopy in Scanning Probe Microscopy: Electrical and Electromechanical Phenomena at the Nanoscale," New York: Springer-Verlag, **1**, 215-253, (2007).

[10] S.-C. Lee, S. M. Anlage, "Study of Local Nonlinear Properties Using a Near-Field Microwave Microscope," IEEE Trans. Appl. Supercond. **13**, 3594, (2003).

[11] S.-C. Lee, S. M. Anlage, "Spatially resolved nonlinearity measurements of $YBa_2Cu_3O_7$ bi-crystal grain boundaries," Appl. Phys. Lett. **82**, 1893, (2003).

[12] S.-C. Lee, S.-Y. Lee, S. M. Anlage, "Microwave Nonlinearities of an Isolated Long $YBa_2Cu_3O_{7-\delta}$ Bicrystal Grain Boundary," Phys. Rev. B **72**, 024527, (2005).

[13] Helmut Kronm$\ddot{u}$ller, Stuart S P Parkin, "Handbook of Magnetism and Advanced Magnetic Materials," Hoboken, NJ : John Wiley & Sons, Online ISBN: 9780470022184, (2007).

[14] R. C. Black, A. Mathai, and F. C. Wellstood, E. Dantsker, A. H. Miklich, D. T. Nemeth, J. J. Kingston, and J. Clarke, "Magnetic microscopy using a liquid nitrogen cooled $YBa_2Cu_3O_7$ superconducting quantum interference device," Appl. Phys. Lett. **62** (17), 2128-2130, (1993).

[15] Boris Chesca, Reinhold Kleiner, Dieter Koelle, "The SQUID Handbook, Vol. I: Fundamentals and Technology of SQUIDs and SQUID Systems," Weinheim: Wiley-VCH. pp. 46-48, ISBN 3-527-40229-2, (2004).

[16] A. M. Chang, H. D. Hallen, L. Harriott, H. F. Hess, H. L. Kao, J. Kwo, R. E. Miller, R. Wolfe, J. van der Ziel, T. Y. Chang, "Scanning Hall probe microscopy," Appl. Phys. Lett. **61**, (16), 1974, (1992).

[17] Jie Li, Min-Sang Lee, Wei He, Bj$\ddot{o}$rn Redeker, Arndt Remhof, Edward Amaladass, Christoph Hassel, and Thomas Eim$\ddot{u}$ller, "Magnetic imaging with femtosecond temporal resolution," Review of Scientific Instruments, **80**, (7), 073703, (2009).

[18] C. P. Vlahacos, J. Matthews, F. C. Wellstood, "A cryo-cooled scanning SQUID Microscope for imaging high-frequncy magnetic fields," IEEE Trans. Appl. Supercond. **21**, no. 3, 412-415, (2011).

[19] J. R. Kirtley, M. V. Ketchen, K. G. Stawiasz, J. Z. Sun, W. J. Gallagher, S. H. Banton, S. J. Wind, "High-resolution scanning SQUID microscope," Appl. Phys. Lett. **66**, 1138, (1994).

[20] R. Proksch, P. Neilson, S. Austvold, and J. J. Schmidt, "Measuring the gigahertz response of recording heads with the magnetic force microscope," Appl. Phys. Lett. **74**, 1308, (1999).

165

[21] M. R. Koblischka, J.-D. Wei, T. Sulzbach, A. D. Johnston, U. Hartmann, "Observation of stray fields from hard-disk writer poles up to 2 GHz," IEEE Trans. on Magnetics, vol. **43**, (6), 2205, (2007).

[22] M. R. Koblischka, J. D. Wei, and U. Hartmann, "High-frequency properties of stray fields emanating from hard disk writer poles up to 2 GHz," J. Magn. Magn. Mater. **322** (9-12), 1694, (2010).

[23] D. I. Mircea and T. W. Clinton, "Near-field microwave probe for local ferromagnetic resonance characterization," Appl. Phys. Lett. **90**, 142504, (2007).

[24] T. W. Clinton, N. Benatmane,J. Hohlfeld, Erol Girt, "Comparison of a near-field ferromagnetic resonance probe with pumpprobe characterization of CoCrPt media," J. Appl. Phys. **103**, (7), 07F546, (2008).

[25] G. Lamura, "First critical field measurements of superconducting films by third harmonic analysis," J. Appl. Phys, **106**, 053903, (2009).

[26] K. Mackay, M. Bonfim, D. Givord, and A. Fontaine, "50 T Pulsed Magnetic Fields in Microcoils," J. Appl. Phys. **87**, 1996, (2000).

[27] T Takamasu, K Sato, Y Imanaka and K Takehana, "Fabrication of a micro-coil pulsed magnet system and its application for solid state physics," Journal of Physics: Conference Series **51**, 591, (2006).

[28] N. Kikuchi, S. Okamoto, O. Kitakami, "Generation of Nanosecond Magnetic Pulse Field for Switching Experiments on a Single Co/Pt Nanodot," J. Appl. Phys. **105**, 07D506, (2009).

[29] Georg Woltersdorf, Christian H. Back, "Microwave Assisted Switching of Single Domain $Ni_{80}Fe_{20}$ Elements," Phys. Rev. Lett. **99**, 227207, (2007).

[30] C. H. Sim, M. Moneck, T. Liew, J.G. Zhu, "Frequency-tunable Perpendicular Spin Torque Oscillator" J. Appl. Phys. **111**, 07C914, (2012).

[31] X. Zhu, J. G. Zhu, "Bias-Field-Free Microwave Oscillator Driven by Perpendicularly Polarized Spin Current," IEEE Trans. Mag. **42**, 2670, (2006).

[32] K. Yoshida., E. Uda, N. Udagawa, and Y. Kanai, "Investigation on Magnetic Fields From Field-Generating Layer in MAMR," IEEE Trans. Mag. **44**, 3408, (2008).

[33] Tamin Tai, B. G. Ghamsari, Steven M. Anlage, "Nanoscale Electrodynamic Response of Nb Superconductors," IEEE Trans. Appl. Supercond. **23**, 7100104, (2013).

[34] M. Muck, C. Welzel, A. Farr, F. Schloz, and W. Singer, "Nondestructive Testing of Niobium Sheets for Superconducting Resonators," IEEE Trans. Appl. Supercond., **13**, no. 2, p. 239, Jun. 2003.

[35] H. Kamerlingh Onnes, "The Disappearance of the Resistance of Mercury," Comm. Phys. Lab. Univ. Leiden; No. 124c, (1911).

[36] V.L. Ginzburg and L.D. Landau, Zh. Eksp. Teor. Fiz. (in Russian) **20**, 1064, (1950). English translation in: L. D. Landau, Collected papers (Oxford: Pergamon Press, 1965) p. 546

[37] C. W. Lam, D. M. Sheen, S. M. Ali, D. E. Oates, "Modeling the nonlinearity of superconducting strip transmission lines," IEEE Trans. Appl. Supercond. **2**, 58, (1992).

[38] S. K. Yip, J. A. Sauls, "Nonlinear Meissner effect in CuO Superconductors," Phys. Rev. Lett. **69**, 2264, (1992).

[39] D. Xu, S. K. Yip, J. A. Sauls, "Nonlinear Meissner effect in unconventional superconductors," Phys. Rev. B. **51**, 16233, (1995).

[40] T. Dahm, D. J. Scalapino, "Theory of intermodulation in a superconducting microstrip resonator," J. Appl. Phys. **81**, 2002, (1997).

[41] A. Zare, T. Dahm, N. Schopohl, "Strong Surface Contribution to the Nonlinear Meissner Effect in d wave superconductors," Phys. Rev. Lett. **104**, 237001, (2001).

[42] A. A. Abrikosov, "On the Magnetic Properties of Superconductors of the Second Group," Soviet Physics JETP **5**, 1174, (1957).

[43] H. F. Hess, R. B. Robinson, R. C. Dynes, J. M. Valles, Jr., and J. V. Waszczak, "Scanning-Tunneling-Microscope Observation of the Abrikosov Flux Lattice and the Density of States near and inside a Fluxoid," Phys. Rev. Lett. **62**, 214-216, (1989).

[44] K. Harada, T. Matsuda, J. Bonevich, M. Igarashi, S. Kondo, G. Pozzi, U. Kaeabe, A. Tonomura, "Real-time observation of vortex lattices in a superconductor by electron microscopy," Nature **360**, 51-53, (1992).

[45] A Oral, S. J. Bending, R. G. Humphreys, M. Henini, "Microscopic measurement of penetration depth in $YBa_2Cu_3O_{7-\delta}$ thin films by scanning Hall probe microscopy," Superconductor Science and Technology **10**, 17, (1997).

[46] A. Y. Aladyshkin, A. V. Silhanek, "Nucleation of superconductivity and vortex matter in superconductor−ferromagnet hybrids," Superconductor Science and Technology **22**, (5), 053001, (2009).

[47] A. Bad́ia, "Inverse magnetic force microscopy of superconducting thin films," Phys. Rev. B **63**, (9), 094502, (2001).

[48] G. Carneiro, "Pinning and creation of vortices in superconducting films by a magnetic diople," Phys. Rev. B **69**, 214504, (2004).

[49] J. Halbitter, "On the Oxidation and on the Superconductivity of Niobium," Appl. Phys. A-Mater. **43**, (1), 1-28 (1987).

[50] G. Ciovati and J. Halbritter, "Analysis of the medium field Q-slope in superconducting cavities made of bulk niobium," Physica C: Superconductivity **441**, (1-2), 57-61 (2006).

[51] J. Halbritter, "On Extrinsic - Weak Link - Effects in the Surface Impedance of Cuprate - and Classical - Superconductors," Fifth Workshop on RF Superconductivity, DESY, Hamburg, Germany (1991).

[52] J. C. Booth, L. R. Vale, R. H. Ono, "On-wafer measurements of nonlinear effects in high temperature superconductors," IEEE Trans. on Appl. Supercond. **11**, 1387, (2001).

[53] S-C. Lee, M. Sullivan, G. R. Ruchti, S. M. Anlage, B. S. Palmer, B. Maiorov, E. Osquiguil, "Doping-denpendent nonlinear Meissner effect effect and spontaneous currents in high-T_c superconductors," Phys. Rev. B **71**, 014507, (2005).

[54] Hasan Padamsee, Jens Knobloch, Tomas Hays "RF Superconductivities on Accelerators (Wiley Series in Beam Physics and Accelerator Technology). " ISBN: 978-3-527-40842-9, (1998).

[55] P. J. Lee, A. A. Polyanskii, A. Gurevich, A. A. Squitieri, D. C. Larbalestier, "Grain Boundary Flux Penetration and Resistivity in Large Grain Niobium Sheet," Physica C **441**, (1-2), 126 (2006).

[56] Taichiro Nishio, Vu Huang Dao, Qinghua Chen, Liviu F. Chibotaru, Kazuo Kadowaki, Victor V. Moshchalkov, "Sanning SQUID microscopy of vortex clusters in multiband superconductors," Phys.Rev. B **81**, 020506(R), (2010).

[57] A. Gurevich, G. Ciovati, "Dynamics of vortex penetration, jumpwise instabilities, and nonlinear surface resistance of type-II superconductors in strong rf fields," Phys. Rev. B **77**, 104501, (2008).

[58] G. Ciovati, G. Myneni, F. Stevie, P. Maheshwari, D. Griffis, "High field Q slope and the baking effect: Review of recent experimental results and new Data on Nb heat treatments," Phys. Rev. Special Topics-Accerlerators and Beams **13**, 022002, (2010).

[59] H. Padamsee, "Basic Principles of RF Superconductivity and SC Cavities," SRF-2009 tutorials, Dresden, Berlin. `http://www.helmholtz-berlin.de/events/srf2009/programs/tutorials_de.html`

[60] A. B. Pippard, "The surface impedance of superconductors and normal metals at high frequency," Proc. Roy. Soc. A **191**, 370-384, (1947).

[61] L. C. Maier, J. C. Slater, "Field strength measurements in resonant cavities," J. Appl. Phys. **23**, 68, (1952).

[62] C.E. Gough, N. J. Exon, "Microwave response of anisotropic high temperature superconductor crystals," Phys. Rev. B. **50**, 488, (1994).

[63] D. E. Oates, S. -H. Park, G. Koren, "Observation of nonlinear Meissner effect in YBCO thin films: evidence for a d-wave order parameter in the bulk of the cuperate superconductors," Phys. Rev. Lett. **93**, 197001, (2004).

[64] S. M. Anlage, D. E. Steinhauer, C. P. Vlahacos, B. J. Feenstra, A. S. Thanawalla, W. Hu, S. K. Dutta, and F. C. Wellstood, "Superconducting Material Diagnostics using a Scanning Near-Field Microwave Microscope," IEEE Trans. Appl. Supercond. **9**, 4127, (1999).

[65] D. I. Mircea, H. Xu, S. M. Anlage, "Phase-sensitive Harmonic Measurements of Microwave Nonlinearities in Cuprate Thin Films," Phys. Rev. B **80**, 144505, (2009).

[66] Tamin Tai, X. X. Xi, C. G. Zhuang, D. I. Mircea, S. M. Anlage, "Nonlinear Near-Field Microwave Microscope for RF Defect Localization in Superconductors," IEEE Trans. Appl. Supercond. **21**, 2615, (2011).

[67] `http://www.spring8.or.jp/en/news_publications/research_highlights/no_51/`

[68] Sharat Batra, M. Covington, T. M. Crawford, Bill Crue, P. A. A. van der Heijden, J. Jayashankar, Earl C. Johns, Mark Kryder, Kevin Minor, Robert

169

Rottmayer, Ut Tran, Jeffrey West, "A Perpendicular Write Head Design for High-Density Recording," IEEE Trans. Magn. **38**, No. 1, 157, (2002).

[69] Masayuki Abe, Yoichiro Tanaka, "A Study of High-Frequency Characteristics of Write Heads With the AC-Phase High-Frequency Magnetic Force Microscope," IEEE Trans. Magn. **38**, 45, (2002).

[70] Klaas B. Klaassen, Jack C.L. van Peppen, "Nanosecond and Sub-Nanosecond Writing Experiments," IEEE Trans. Magn. **35**, No.2, 625, (1999).

[71] K. Z. Gao, O. Heinonen, Y. Chen, "Read and write processes, and head technology for perpendicular recording," J. Magn. Magn. Mater., **321**, 495-507, (2009).

[72] S. X. Wang and A. M. Taratorin, *Magnetic Information Storage Technology*, Academic Press, San Diego, p. 89. (1999).

[73] M. R. Koblischka, J. D. Wei, M. Kirsch, U. Hartmann, "High frequency magnetic force microscopy-imaging of harddisk write heads," Japanese J. Appl. Phys. **45**, 2238-2241, (2006).

[74] http://en.wikipedia.org/wiki/Quantum_Bigfoot_(hard_drive)

[75] M. V. Milošević, S. V. Yampolskii, and F. M. Peeters, "Magnetic pinning of vortices in a superconducting film: The antivortex magnetic dipole interaction energy in the London approximation," Phys. Rev. B **66**, 174519, (2002).

[76] F. H. Liu, S. Shi, J. Wang, Y. Chen, K. Stoev, L. Leal, R. Saha, H.C. Tong, S. Dey, M. Nojaba, "Magnetic recording at a data rate of one gigabit per second," IEEE Trans. Appl. **37**, (2), 613-618, (2001).

[77] M. Tinkham, "Introduction to Superconductivity" Second Edition, Chapter **3**, 105, ISBN-10: 0486435032 — ISBN-13: 978-0486435039.

[78] D. E. Oates, Y. D. Agassi, B. H. Moeckly, "Intermodulation Distortion and Nonlinearity in MgB_2: Experiment and Theory," IEEE Trans. Appl. Supercond. **17**, (2), 2871-2874, (2007).

[79] D. W. Face, R. J. Small, M. S. Warrington, F. M. Pellicone, P. J. Martin. "Large area $YBa_2Cu_3O_7$ and $Tl_2Ba_2CaCu_2O_8$ thin films for microwave and electronic applications," Physica C, **357**, pp. 1488-1494, (2001).

[80] Charles P. Bean, "Magnetization of High-Field Superconductors," Rev. Mod. Phys. **36**, 31, (1964).

[81] X. Zeng, A. V. Pogrebnyakov, A. Kotcharov, J. E. Jones, X. X. Xi, E. M. Lysczek, J. M. Redwing, S. Y. Xu, J. Lettieri, D. G. Schlom, W. Tian, X. Q. Pan, Z. K. Liu, "In Situ Epitaxial MgB_2 Thin Films for Superconducting Electronics," Nature Materials **1**, 35, (2002).

[82] L. Ji, R. H. Sohn, G. C. Spalding, C. J. Lobb, and M. Tinkham, "Critical state model for harmonic generation in high-temperature superconductors," Phys. Rev. B **40**, 10936-10945, (1989).

[83] C. P. Bean, J. D. Livingston, "Surface barrier in Type-II superconductors," Phys. Rev. Lett. **12**, 14-16, (1964).

[84] Sheng-Chiang Lee, "Measurement of doping dependent microwave nonlinearities in high temperature superconductors," *Ph.D Dissertation, University of Maryland-College Park*, (2004), http://hdl.handle.net/1903/1372.

[85] S. X. Wang and A. M. Taratorin, "Magnetic Information Storage Technology," San Diego, CA: Academic Press, Chapter 2, p. 38, (1999).

[86] Di Kang, Derek C. Baars, Thomas R. Bieler, and Chris C. Compton, "Characterization of Large Grain Nb Ingot Microstructure Using EBSP Mapping and Laue Camera Methods," AIP Conf. Proc. **1352**, 90-99, (2010).

[87] Carson Jeffries, Q. Harry Lam, Youngtae Kim, L. C. Bourne, and A. Zettl, "Symmetry breaking and nonlinear electrodynamics in the ceramic superconductor $YBa_2Cu_3O_7$," Phys. Rev. B. **37**, 9840, (1988).

[88] Ting-kang Xia, D. Stroud, "Nonlinear electrodynamics and nonresonsnt microwave absoption in ceramic superconductors," Phys. Rev. B. **39**, (7), 4792, (1989).

[89] Jonathan I. Gittleman, Bruce Rosenblum, "Radio-Frequency Resistance in the Mixed State for Subcritical Currents," Phys. Rev. Lett. **16**, 734, (1966).

[90] Ernst Helmut Brandt, "Electrodynamics of superconductors exposed to high frequency fields," arxiv:1008.2231.

[91] M. V. Milošević, F. M. Peeters, "Vortex pinning in a superconducting film due to in-plane magnetized ferromagnets of different shapes: The London approximation," Phys. Rev. B. **69**, 104522, (2004).

171

[92] A. V. Kapra, V. R. Misko, D. Y. Vodolazov and F. M. Peeters, "The guidance of vortex-antivortex pairs by in-plane magnetic dipoles in a superconducting finite-size film," Supercond. Sci. Technol. **24**, 024014, (2011).

[93] M. J. Van Bael, J. Bekaert, K. Temst, L. Van Look, M. V. Moshchalkov, Y. Bruynseraede, G. D. Howells, A. N. Grigorenko, S. J. Bending "Local observation of field polarity dependent flux pinning by magnetic dipoles," Phys. Rev. Lett. **86**, (1), 155-158, (2001)

[94] V. Ambegaokar and Baratoff, "Tunneling Between Superconductors," Phys. Rev. Lett. **10**, 486, (1963)

[95] Michael Tinkham, "Introduction to superconductivity," 2nd Edition, ISBN-10: 0486435032 — ISBN-13:978-0-486-43503-9, Chapter 3, p63, (2004).

[96] J. Halbritter, "Materials science and surface impedance Z (T,f,H) of Nb and YBCO and their quantitative modelling by the leakage current of weak links," Supercond. Sci. Tech. **12**, (11), 883-886, (1999).

[97] J. Halbritter, "Granular superconductors and their intrinsic and extrinsic surface impedance," Journal of Superconductivity **8**, (6), 691-703, (1995).

[98] J.R Waldram, "Superconductivity of Metals and Cuprates," Chapter **10**. (The non-local form of BCS theory) ISBN-10: 0852743378 — ISBN-13: 978-0852743379, (1996).

[99] T. Tajima, A. Canabal, Y. Zhao, A. Romanenko, B. H. Moeckly, C. D. Nantista, S. Tantawi, L. Phillips, Y. Iwashita and I. E. Campisi, "MgB$_2$ for Application to RF Cavities for Accelerators," IEEE Trans. Appl. Supercond. **17**, 1330-3, (2007).

[100] J. Nagamatsu, Norimasa Nakagawa, Takahiro Muranaka, Yuji Zenitani, Jun Akimitsu, "Superconductivity at 39K in Magnesium Diboride," Nature **410**, 63, (2001).

[101] X. X. Xi, "Topical Review - MgB$_2$ Thin Films," Supercond. Sci. Technol. **22**, 043011, (2009).

[102] G. Cifariello, M. Aurino, E. D. Gennaro, G. Lamura, A. Andreone,P. Orgiani, X. X. Xi, "Intrinsic Nonlinearity Probed by Intermodulation Distortion Microwave Measurements on High Quality MgB$_2$ Thin Films," Appl. Phys. Lett. **88**, 142510, (2006).

[103] T. Dahm, D. J. Scalapino,"Nonlinear Microwave Response of MgB_2," Appl. Phys. Lett. **85**, 4436, (2004).

[104] Y. D. Agassi, D. E. Oates, and B. H. Moeckly, "Evidence for non-s-wave Symmetry of the π Gap in MgB_2 From Intermodulation Distortion Measurements," Phys. Rev. B **80** (17), 174522, (2009).

[105] D. E. Oates, Y. D. Agassi, and B. H. Moeckly, "Microwave Measurements of MgB_2: Implications for Applications and Order-parameter Symmetry," Supercond. Sci. Technol. **23** 034011, (2010).

[106] D. Agassi, D. E. Oates, "Nonlinear Meissner Effect in a High-temperature Superconductor," Phys. Rev. B **72**, 014538, (2005).

[107] A. A. Gallitto, G. Bonsignore, M. L. Vigni, "Third-Harmonic Emission in MgB_2 Superconductor at Microwave Frequencies," International Journal of Modern Physics B **17**, 535-541, (2003).

[108] E. J. Nicol, J. P. Carbotte, D. J. Scalapino, "Nonlinear Current Response of One- and Two-band Superconductors," Phys. Rev. B **73**, 014521, (2006).

[109] J. Gittleman, B. Rosenblum, T. E. Seidel, and A. W. Wicklund, "Nonlinear Reactance of Superconducting Films," Phys. Rev. **137**, A527, 536, (1965).

[110] A. Gurevich and V. M. Vinokur, "Interband Phase Modes and Nonequilibrium Soliton Structures in Two-Gap Superconductors," Phys. Rev. Lett. **90** (4), 047004, (2003).

[111] T. B. Samoilova, "Non-linear Microwave Effects in Thin Superconducting Films," Supercond. Sci. Technol. **8**, 259, (1995).

[112] A. P. Zhuravel, B. G. Ghamsari, C. Kurter, P. Jung, S. Remillard, J. Abrahams, A. V. Lukashenko, Alexey V. Ustinov, Steven M. Anlage, "Imaging the Anisotropic Nonlinear Meissner Effect in in Nodal $YBa_2Cu_3O_{7-\delta}$ Thin-Film Superconductors," Phys. Rev. Lett. **110**, 087002, (2013).

[113] Rafael B. Dinner, M. R. Beasley, and Kathryn A. Moler, "Cryogenic scanning hall-probe microscope with centimeter scan range and submicron resolution," Review of Scientific Instruments **76**, 103702, (2005).

[114] J. Hayton, J. Polesel-Maris, R. Demadrille, M. Brun, F. Thoyer, C. Lubin, J. Cousty, B. Grévin "Atomic Force Microscopy Imaging Using a Tip-on-chip: Opening the door to Integrated Near Field Nanotools," Review of Scientific Instruments **81**, 093707, (2010).

[115] Din Ping Tsai, Yuan Ying Lu, "Tapping-mode tuning fork force sensing for near-field scanning optical microscopy," Appl. Phys. Lett. **73**, 2724, (1998).

[116] M. Dede, K. Ürkmen, Ö. Girisen, M. Atabak, A. Oral, I. Farrer, and D. Ritchie, "Scanning Hall Probe Microscopy (SHPM) Using Quartz Crystal AFM Feedback," Journal of Nanoscience and Nanotechnology, Vol.**X**, 1V4, (2007).

[117] Ke Chen, Y. Cui, Qi Li, X. X. Xi, Shane A. Cybart, R. C. Dynes, X. Weng, E. C. Dickey, and J. M. Redwing,"Planar MgB_2 superconductor-normal metal-superconductor Josephson junctions fabricated using epitaxial MgB_2 /TiB_2 bilayers," Appl. Phys. Lett. **88**, 222511, (2006).

[118] W. Singer, D. Proch, A. Brinkmann, "Diagnostic of defects in high purity niobium," Particle Accelerators, **60**, (1-4), 83, (1998).

[119] A. P. Zhuravel, A.G. Sivakov, O.G. Turutanov, A.N. Omelyanchouk, Steven M. Anlage, A.V. Ustinov, "Laser Scanning Microscope for HTS Films and Devices," Low Temperature Physics **32**, 592-607, (2006).

[120] Behnood G. Ghamsari, Jacob Tosado, Mahito Yamamoto, Michael S. Fuhrer, Steven M. Anlage, "Determination of the Optical Index for Few-Layer Graphene by Reflectivity Spectroscopy," arXiv:1210.0575.

[121] Victor Moshchalkov, Mariela Menghini, T. Nishino, Q. H. Chen, A. V. Silhanek, V. H. Dao, L. F. Chibotaru, N. D. Zhigadlo, J. Karpinski, "Type-1.5 Superconductivity," Phys. Rev. Lett. **102**, 117001, (2009).

174

Tamin Tai

3504 Susquehanna Dr. Beltsville MD 20705

Cell Phone: 240-338-7974   Email: tamin@umd.edu

EDUCATION

Ph.D. in Electrical and Computer Engineering   August/2013
University of Maryland, College Park, MD

M.S. in Electrical and Computer Engineering, electro-physics   December/2012
University of Maryland, College Park, MD

M.S. in Material Science and Engineering   June/2004
National Tsing Hua University, Hsin-Chu, Taiwan.

B.S. in Material Science and Engineering   June/2002
National Tsing Hua University, Hsin-Chu, Taiwan.

KNOWLEDGE, SKILLS

Languages/Programming: C language, Matlab, Labview, Mathematica, ANSYS High Frequency Structure Simulator (HFSS), ANSYS Computer Simulation Technology (CST) Microwave Studio, AutoCAD 3D Modeling.

Nano Technology: Transmission Electron Microscope (TEM), Scanning Electron Microscope (SEM), Electron Beam Lithography, Focus Ion Beam System (FIB). Scanning Probe Microscope (AFM, MFM, KFM), Near Field Microwave Microscope, Cryogenic Probe Station.

Fabrication: Physical Vapor Deposition, Chemical Vapor Deposition, Ion Milling, Plasma etching.

Instrumentation: Oscilloscopes, Locking Amplifier, Network Analyzers, Spectrum Analyzer, Laser System (CW laser and Mode Locking laser).

EXPERIENCE

Graduate Research Assistant, Center for Nanophysics and Advance Materials (CNAM), *University of Maryland, College Park, College Park MD.*   *9/2009~Present*

- Design and fabricate different kinds of nano-scale magnetic probes (magnetic writers), Josephson junctions and SQUID devices by the method of e-beam lithography and focus ion beam (FIB).

- Develop a novel Near-Field Scanning Microwave Microscope (NSMM) where a Scanning Tunneling Microscope (STM) is used for tip-to-sample distance control.

- Integrate nano-scale magnetic probes (magnetic writers) into a novel high resolution near-field scanning microwave microscope operating at cryogenic temperatures down to 4.2K and high frequency up to 20 GHz to identify defects on Superconductors.

- Design a height control feedback loop in the scanning probe microscopy.

- Measure the high order harmonic responses of superconductors (Cuprate,MgB_2, Nb)

- Simulate the electromagnetic properties of nano-scale magnetic device by Finite Element Modeling, for example, ANSYS High Frequency Structural Simulator (HFSS), Computer Simulation Technology (CST) Microwave Studio.

Summer Research Intern, Laboratory for Physical Sciences (LPS), MD.   *6/2009~8/2009*

- Measure electro-optic coefficient of poled polymers by the Laser reflection technique.
- Calculate the electro-optic coefficient of poled polymers by the multi-refraction model.

Teaching Assistant, Electrical and Computer Engineering, University of Maryland.   8/2008~5/2009

Research Engineer, National Taiwan University, Taipei, Taiwan.   11/2004~7/2006

- Designed and fabricated wavelength converter device on $LiTaO_3$ and $LiNbO_3$ crystal fiber.
- Measured second harmonic responses of optics devices by pulse Laser and CW Laser.
- Calculated the conversion efficiency of the nonlinear optics device.

Graduate Research Assistant, National Tsing Hua University, Hsin-Chu, Taiwan.   9/2002~7/2004

- Deposited nanoscale structures by sputtering and chemical depositions processes.
- Designed Spintronic device including giant magnetoresistance device (GMR) and tunnel magnetoresistance device (TMR).
- Characterized nanoscale structures with X-Ray diffraction (XRD), and Transmission Electron Microscopy (TEM).   Magnetic property characterization by Vibrating Sample Magnetometer (VSM), and Magnetic Force Microscopy (MFM)

Selected Publications

Tamin Tai, B. G. Ghamsari, Steven M. Anlage, " Modeling the nanoscle linear response of superconducting thin films," (Under preparation to Superconductor Science and Technology)

Tamin Tai, B. G. Ghamsari, Tom Bieler, Steven M. Anlage, " Nanoscale Nonlinear Radio Frequency Properties of Bulk Nb: Origins of Extrinsic Nonlinear Effects'' (Under preparation to Phys. Rev. B)

Tamin Tai, B. G. Ghamsari, Steven M. Anlage, "**Nanoscale Electrodynamic Response of Nb Superconductors**," *IEEE Trans. Appl. Supercond. 23, 7100104, 2013.*

Tamin Tai, B. G. Ghamsari, T. Tan, C. G. Zhuang, X. X. Xi, Steven M. Anlage, "**MgB_2 Nonlinear Properties Investigated Under Localized High RF Magnetic Field Excitation**," *Phys. Rev. ST Accel. Beams 15, 122002, 2012.*

Tamin Tai, X. X. Xi, C. G. Zhuang, Dragos I. Mircea, Steven M. Anlage, "**Nonlinear Near-Field Microwave Microscope For RF Defect Localization in Superconductors**," *IEEE Trans. Appl. Supercond., 21, 2615-2618, 2011.*

S. C. Pei, T. S. Ho, **T. M. Tai**, L. M. Lee, J. C. Chen, A. H. Kung, F. J. Kao, and S. L. Huang**, "Drawing of single crystal and glass-clad lithium tantalate fibers by the laser-heated pedestal growth method,"** *Journal of Applied Crystallography, 43, 48-52, 2010.*

L. M. Lee, S. C. Pei, D. F. Lin, M. C. Tsai, **T. M. Tai**, P. C. Chiu, D. H. Sun, A. H. Kung, and S. L. Huang, "**Generation of tunable blue-green light using ZnO periodically poled lithium niobate crystal fiber by self-cascaded second-order nonlinearity**," *Journal of the Optical Society of America B, 24, 1909-1915, 2007.*

Honors/Awards

Winners of the *"European Superconductivity News Forum (ESNF)"* **contest for best manuscripts in Applied Superconductivity Conference (ASC), Portland Oregon 2012.** (Refer to the announcement http://www.ewh.ieee.org/tc/csc/europe/newsforum/Contents23.html)

Graduate Assistantship, University of Maryland, Center for Nanophysics and Advanced Materials, 2009~present.

Travel Award provided by 15th International Conference on RF Superconductivity 7/25/2011~7/29/2011.

Travel Award provided by USC-DOE Conference on Materials for Energy Applications 3/30/2011~4/1/2011.

Summer (2009) Internship: Laboratory for Physical Sciences (LPS).

Graduate Teaching Assistantship: University of Maryland, Electrical and Computer Engineering, 8/2008 (Teaching Offer) & 1/2009 (Grader Offer).

Thesis Prize in Taiwan Association for Magnetic Technology, 2005.

Professional Activities/Affiliations

Paper Reviewer---Applied Superconductivity Conference (ASC) 2012.
Paper Reviewer--- Conference on Precision Electromagnetic Measurements (CPEM) 2012.